Three Dimensional Microanalysis by Energy Dispersive Spectrometry: Improved Data Processing

THÈSE N^{O} 5501 (2012)

PRÉSENTÉE LE 19 OCTOBRE 2012

LA FACULTÉ DES SCIENCES ET TECHNIQUES DE L'INGÉNIEUR
CENTRE INTERDISCIPLINAIRE DE MICROSCOPIE ÉLECTRONIQUE
PROGRAMME DOCTORAL EN SCIENCE ET GÉNIE DES MATÉRIAUX

ÉCOLE POLYTECHNIQUE FÉDÉRALE DE LAUSANNE

POUR L'OBTENTION DU GRADE DE DOCTEUR ÈS SCIENCES

PAR

Pierre BURDET

acceptée sur proposition du jury:

Prof. K. Scrivener, présidente du jury
Prof. C. Hébert, Dr M. Cantoni, directeurs de thèse
Prof. T. Epicier, rapporteur
Prof. P. Hoffmann, rapporteur
Prof. P. Midgley, rapporteur

ÉCOLE POLYTECHNIQUE
FÉDÉRALE DE LAUSANNE
Suisse
2012

Abstract

This thesis is focused on a combined microscopy technique: energy dispersive spectrometry (EDS) is extended to a three dimensional (3D) microanalysis using a so-called "dual-beam microscope": a scanning electron microscope (SEM) equipped with a focused ion beam (FIB). In the sequential acquisition, the surface freshly milled by the FIB is characterised by SEM imaging and EDS mapping. A 3D elemental picture of the specimen is obtained this way. This technique suffers from the same limitations than the 2D EDS mapping, the major one being linked to the volume of X-ray emission that is large due to the required high accelerating voltage. Other limitations of 3D EDS microanalysis are more specific to FIB/SEM technique, such as the low acquisition time per spectrum due to the large number of spectra required in an acquisition. The goal of this thesis was to develop post-processing solutions to overcome the limitations of 3D EDS microanalysis. Three solutions have been developed. As the acquired data are composed of a high number of noisy spectra, multivariate statistic methods are appropriate. Such a technique is adapted to 3D EDS data and provides smoother spectra improving the quantification afterwards. When analysing a feature that is smaller than the volume of X-ray emission, the quantified composition is inaccurate as part of the X-rays are emitted from the feature's surrounding. To take into account the influence of the neighbouring voxels, an enhanced quantification technique is developed. It is based on a recursive approach adapting an existing complex quantification. Another complementary approach is developed to resolve features too fine for EDS mapping: the segmentation technique is improved by using the higher spatial resolution of SEM images.
A sample formed by laser welding of nickel-titanium (NiTi) and stainless-steel wires is characterised by 3D EDS microanalysis. The acquired data are used to demonstrate the gains and the limitations of the three developed processing techniques. With them, the noise-reduced spectra reveal further details of the fine microstructure. Their quantified composition is closer to the one predicted by the phase diagram. Furthermore, the segmented phases used for the 3D visualisation have a resolution close to the one of the SEM images. This visualisation allows a deeper comprehension of the formation of the phases and their morphologies during the implied solidification. This demonstrates the great potential of this technique to characterise samples with complex microstructure and complex composition.

Keywords: energy dispersive X-ray spectrometry (EDS), focused ion beam (FIB), 3D microanalysis, tomographic spectral imaging, Al-Zn alloys, Fe-Ni-Ti alloys, 3D spectral image analysis, principal component analysis (PCA), quantitative analysis, in-depth analysis, global thresholding.

Résumé

Cette thèse se focalise sur une technique de microscopie : la spectrométrie des rayons-X à sélection d'énergie (EDS) est étendue à la microanalyse en trois dimensions (3D) grâce au microscope à double faisceaux, électronique et ionique (MEB-FIB). Dans le processus séquentiel d'acquisition, la surface fraîchement abrasée est caractérisée par une image spectrale et une image MEB. Une cartographie X en 3D de l'échantillon est ainsi obtenue. Certaines des limitations de cette technique sont identiques à celles rencontrées en 2D, comme celles liées au volume d'émission des rayons-X qui est important de par la nécessité d'une haute tension d'accélération. D'autres limitations sont plus spécifiques à la technique MEB-FIB, comme un temps d'acquisition par spectre limité par le grand nombre de spectres dans une acquisition en 3D.
Le but de cette thèse est de développer des techniques de traitement d'image pour compenser les limitations de la microanalyse EDS en 3D. Trois techniques ont ainsi été développées. Comme les données sont composées de beaucoup de spectres bruités, les techniques de statistique multivariée sont appropriées. Une de celles-ci est adaptée à ce type de données, permettant de réduire le bruit dans les spectres et ainsi d'améliorer grandement la quantification. L'analyse d'objets plus petits que le volume d'émission des rayons-X est faussée, car les rayons-X ne proviennent pas du seul point analysé. Pour tenir compte de l'influence des voxels avoisinants, une technique est développée qui, dans une approche récursive, applique une méthode existante de quantification. Une approche complémentaire est développée afin de résoudre les structures trop fines pour la cartographie X : l'étape de segmentation du volume analysé est améliorée en utilisant les images MEB avec leur meilleure résolution spatiale.
Un échantillon formé d'une soudure laser entre deux fils de nickel/titane (NiTi) et d'acier inoxydable est caractérisé par microanalyse EDS en 3D. Les données acquises sur cet échantillon sont utilisées pour démontrer le gain et les limitations des trois techniques développées dans cette thèse. Grâce à celles-ci, la forte réduction de bruit permet de mieux distinguer les structures fines. De plus, les compositions de ces dernières sont plus proches de celles prédites par le digramme de phase. Et les phases utilisées pour la visualisation 3D ont une résolution spatiale proche de celle des images MEB. Cette visualisation a permis la compréhension de la formation des phases et de leur morphologie durant la solidification, démontrant le fort potentiel de la technique pour la caractérisation d'échantillons à microstructure complexe, chimiquement et géométriquement.

Mots-clés : Spectrométrie des rayons-X à sélection d'énergie (EDS), faisceau d'ion focalisé (FIB), microanalyse en 3D, imagerie spectrale par tomographie, alliage Al-Zn, alliage Fe-Ni-Ti, traitement d'image spectrale en 3D, analyse des composants principaux (PCA), analyse quantitative, analyse en profondeur, segmentation par seuillage.

Acknowledgements

Funding	Carl Zeiss
Supervision	Dr. Marco Cantoni and Prof. Cécile Hébert
Thesis jury	Prof. Patrik Hoffmann, Prof. Thierry Epicier, and Prof. Paul Midgley
Collaborator	Dr. Jonas Vannod, Dr. Jonathan Friedli, Dr. Haïcha Hessler, Dr. Mario Salgado, Prof. Michel Rappaz, and all people from CIME
In particular	Dr. Guillaume Lucas, Philippe Pinard, and Dr. Martin Kienle
Technical support	Gloor Instruments, Carl Zeiss, and Oxford Instruments
Friend/colleague	Anas Mouti, Guillaume Pasche, Jonas Valloton, Christian Monachon, Léa Deillon, Andreas Schuler, and all the others
Personnal	Marie-Catherine Burdet, Philippe Burdet, Julie Burdet, Adèle Burdet, Lucie Burdet, Keziah Burdet, and Annabelle Souriau

Lausanne, 20 September 2012 Pierre Burdet

Contents

Abstract iii

Résumé v

Acknowledgements vii

1 Introduction 1
- 1.1 Microanalysis in 3D . . . 1
- 1.2 Motivations . . . 2
- 1.3 Objectives and structure . . . 4

2 State of the art 5
- 2.1 Characteristic X-rays . . . 6
  - 2.1.1 Electron-solid interaction . . . 6
  - 2.1.2 X-ray spatial distribution . . . 7
- 2.2 Dual beam FIB/SEM microscope . . . 10
  - 2.2.1 Scanning electron microscopy (SEM) . . . 11
  - 2.2.2 Energy dispersive X-ray spectrometry (EDS) . . . 12
  - 2.2.3 Focused ion beam (FIB) . . . 12
- 2.3 3D EDS microanalysis . . . 13
  - 2.3.1 Acquisition method and sample geometry . . . 14
  - 2.3.2 Limitations and artifacts . . . 16
- 2.4 Data processing . . . 19
  - 2.4.1 Spectrum . . . 19
  - 2.4.2 Serial cuts . . . 21
  - 2.4.3 Spectral image . . . 22

3 Materials and method 25
- 3.1 Materials . . . 25
  - 3.1.1 Al-Zn alloy: test-case sample . . . 26
  - 3.1.2 NiTi-stainless steel laser weld: real-case sample . . . 26
  - 3.1.3 Other materials . . . 28
- 3.2 Method . . . 29
  - 3.2.1 Instrumentation . . . 29

3.2.2 Acquisition conditions . . . 30
3.2.3 Computing . . . 33

4 Parasite X-rays **35**
4.1 Measurement method . . . 35
4.2 Results . . . 36
4.3 Discussion . . . 38

5 Noise reduction **41**
5.1 Measurement of the noise level . . . 42
5.1.1 Sets of spectra . . . 42
5.1.2 Variations in the sets . . . 43
5.2 Noise reduction procedure . . . 44
5.2.1 PCA as a noise-filter . . . 44
5.2.2 Median filter . . . 47
5.2.3 The procedure as a whole . . . 49
5.3 Evolution of noise during quantification . . . 50
5.3.1 Qualitative results . . . 50
5.3.2 Quantitative results . . . 52
5.4 Summary . . . 56

6 Quantification enhancement **57**
6.1 Interaction-volume impact . . . 58
6.1.1 Homogeneous microvolume . . . 58
6.1.2 Heterogeneous microvolume . . . 60
6.2 First approach . . . 62
6.2.1 Implementation . . . 62
6.2.2 Test on profile along z . . . 65
6.3 Full method . . . 68
6.3.1 Tilt effect . . . 69
6.3.2 Implementation . . . 70
6.3.3 Test on simulation . . . 72
6.3.4 Test on measured data . . . 74
6.4 Synthesis and improvement perspectives . . . 82

7 Segmentation **83**
7.1 Segmentation of EDS maps . . . 84
7.1.1 Ternary histogram . . . 84
7.1.2 Defining the threshold domains . . . 86
7.1.3 Position of the domain boundaries . . . 88
7.2 Segmentation refinement with SE images . . . 90
7.3 Summary . . . 94

8 Conclusion **95**
8.1 Synthesis 95
8.2 Outlook 98

Bibliography **102**

A Notation **103**

B Processing steps **105**

C Publications **109**

Curriculum Vitae **111**

1 Introduction

Exploring the inside of materials has always been of high interest; how many children have broken a stone to observe its insides. Besides the simple curiosity, the investigation of the materials structure has proven to be crucial for the understanding of the material properties and for their improvement. They depend on the arrangement of the atoms at different scales, from the crystalline unit cell at nanometre scale up to the segregation at macro-scale. To explore a structure, the ideal characterisation technique would grab the position and the kind of any atom, providing a complete picture of the material structure at any scale. But common characterisation techniques provide limited information at a limited scale. Many of them are limited to two dimensions (2D), and this is often not sufficient for an understanding of the complex structure. Other techniques can access three dimensions (3D) but they lack elemental information.

This thesis is focused on a quite recent technique, 3D EDS microanalysis. Energy dispersive spectrometry (EDS) is a well-established technique for elemental analysis and has recently been extended to the third dimension by the micromachining ability of the focused ion beam (FIB). This technique provides a 3D elemental picture of the specimen. Like all techniques, also this one has its limitations; the purpose of this work is to explore, understand, and extend these limits.

1.1 Microanalysis in 3D

Using an electron beam as a probe to image a specimen at high spatial resolution is an old idea that has led to the advent of a whole range of characterisation instruments, namely the electron microscopes (EM). Among the early inventors, R. Castaing has developed in 1951 the first electron probe microanalyser (EPMA), an instrument that detects the X-rays generated by the interaction of the electrons with the bulk specimen [1]. Part of these X-rays are characteristic of the element present in the sample and can be used to determine the local composition of the specimen. Since the first EPMA, the technique has greatly evolved, and new microscopes and spectrometers have been developed. Nowadays, the most widely used one is the scanning electron microscope (SEM) with an EDS detector.

Two advantages make the SEM/EDS instrument suited for elemental mapping. With the EDS detector, a spectrum over a large range of energies is recorded at once, allowing one to detect elements from Boron up to the very heavy ones. The EDS analysis is performed at the position of the electron beam. The EDS map is formed recording a spectrum at each position of a scan across the specimen surface. Depending on the time spend per spectrum, the EDS map provides a qualitative or a quantitative elemental map of the specimen.

The amount of information that the technique can access is limited by the EDS detector. Due to its low efficiency at low energies, light elements are poorly analysed. The low energy resolution of the EDS detector reduces the peak to background ratio, and this limits the detection of trace elements. The smallest spatial volume that the technique can access is limited by the volume from which the X-rays are emitted. As the energy of the electron beam needs to be high enough to excite the desired characteristic X-ray lines, this volume is often large, roughly in the micrometre range.

The FIB was formally developed for the semiconductor industry for failure analysis. When it was combined with a SEM forming the so-called "dual beam FIB/SEM", it became interesting for materials science as a characterisation instrument. The FIB works on the same principle as the SEM, i.e. a highly focused beam scans the sample surface. Instead of electrons, gallium ions are used to form the beam. The interaction of the ion beam with the sample permits to mill away material with a high spatial resolution. The FIB is a micromachining tool that allows the EDS to be extended in 3D. The ion beam removes material from the sample, and an EDS map of the freshly created surface is recorded. These two operations are sequentially repeated to analyse a volume of the specimen. 3D EDS microanalysis is a tomographic spectral imaging technique.

1.2 Motivations

The extension of EDS mapping to three dimensions requires a modification of the acquisition conditions. On one hand, the geometry is more complex as shown in figure 1.1 with a sample ready for acquisition. The angles between the milled surface, the electron beam, and the detector are different than in conventional SEM-EDS, and the milled surface is surrounded by trenches. On the other hand, the acquisition operation is more complex as it consists of a sequence of milling and EDS maps recording steps. The acquisition spreads over a longer duration, up to several days. Numerous spectra are acquired in a limited time; the time spent per spectra is less.

These differences in acquisition conditions cause specific limitations. Spurious X-rays are generated in the surrounding trenches and can be detected, the so-called parasite X-rays . During the acquisition, global conditions of the whole system, such as temperature, may vary and this can cause drift (e.g. drift of the sample position). As the acquisition time per spectrum is short, the spectra suffer from high noise (or a poor signal-to-noise ratio).

A first comprehensive study on this technique was carried out by M. Schaffer during her thesis [2].

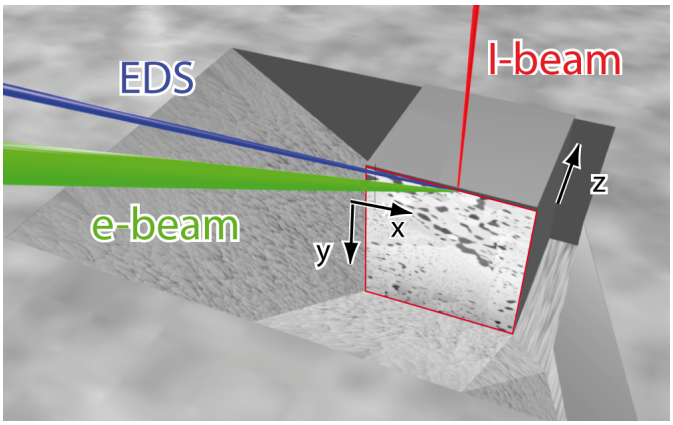

Figure 1.1: Schematic view of a sample ready for acquisition. The position of the different beams is shown. The sample surface is perpendicular to the ion beam that is parallel to y axis. z axis shows the direction of sequential milling. The freshly milled surface is surrounded in red.

Focused mainly on the acquisition, she developed technical solutions to the specific limitations: among others, solutions to reduce the parasite X-rays artefact and the drift problem. Since her thesis, the availability of a faster detector, the silicon drift detector (SDD), has greatly improved the counting statistics. 3D EDS microanalysis has become significantly better on the experimental side.

On the data processing side, the extension of EDS mapping to three dimensions opens new opportunities to develop further solutions to the limitations:

1. The stack is composed of a high number of noisy spectra that are correlated one to the other, as the X-rays are characteristic for a (in general) limited number of elements and phases. With this kind of data, multivariate statistics can be efficiently applied for data mining, and/or for noise reduction.
2. The volume of X-ray emission, which can be seen as a point spread function (PSF) of the EDS map, has a cylindrical geometry and is elongated in the depth direction. Now accessible with the 3D mapping, the depth information can be used for deconvolution techniques.
3. During the acquisition, SEM images can be recorded in parallel to the EDS maps. The SEM images generally have a better spatial resolution and can be used in a complementary processing step to improve the resolution of the results.

Only few specific processing developments have been reported. The only noticeable one is a data mining technique based on the principal component analysis (PCA) reported by Kotula and Keenan [3]. Therefore, this project aims to develop and to adapt processing techniques in order to benefit from the opportunities offered by 3D EDS data.

1.3 Objectives and structure

The goal of this work is to thoroughly study the limitations of 3D EDS microanalysis in order to develop appropriate solutions based on data processing techniques. The development of a full processing procedure, from the raw data to the final 3D visualisation, will be demonstrated. This procedure will be presented by three processing techniques, each one being a solution to one limitation of 3D EDS microanalysis. Each of these techniques benefits from an opportunity listed before:

1. A noise-reduction technique: the high noise due the short acquisition time per spectrum will be reduced taking advantage of the high number of spectra.
2. A quantification technique: when analysing features smaller than the X-ray emission volume, the low compositional accuracy will be improved by taking into account the neighbouring spectra laterally as well as in depth.
3. A segmentation technique: The low spatial resolution of EDS maps will be improved taking advantage of the high spatial resolution of SEM images for the segmentation.

This thesis is composed of 8 chapters. Chapter 2 introduces the bases and the relevant literature for 3D EDS microanalysis. The fundamentals on electron/solid interaction, the instrument, and the experimental technique will be described in order to understand more deeply the limitations of the technique. An emphasis will be also given on the data processing techniques related to 3D EDS microanalysis.

Chapter 3 presents the samples and the acquisition conditions used to acquire two stacks of data. The choice of the samples appropriate for the work's objective will be stressed.

Chapter 4 is dedicated to a further study of the parasite X-rays artefact with a focus on the influence of the operator-controllable parameters.

Chapters 5, 6, and 7 discuss the development of the three processing techniques, respectively the noise reduction, the quantification enhancement, and the segmentation. After the description of their implementation, an emphasis will be also given on their limitations as tested with the stack of data. Each of these chapters will be then summarized.

Finally, chapter 8 will provide a synthesis on the processing techniques, individually and as a whole procedure. The possible improvements of these techniques will be discussed, as well as an outlook for a different global approach.

This thesis was financed by Carl Zeiss in a four-years project.

2 State of the art

This chapter presents the bases and the relevant literature for 3D EDS microanalysis with a focus on data processing. It is divided in four sub-sections. The first one presents an overview of the involved physical phenomena (section 2.1). In the next two sections, the state of the art of the used microscopic techniques and experimental methods are described (section 2.2 and 2.3). Processing techniques for 3D EDS data are reviewed in the last section (section 2.4).

2.1 Characteristic X-rays

This section presents the relevant parts of the theory about characteristic X-rays. An extensive electron-solid interaction description can be found for example in Goldstein's textbook in chapter 3 and in chapter 6 [4].

2.1.1 Electron-solid interaction

Figure 2.1(a) illustrates schematically the interactions of a electron beam with an atom represented by the Bohr model. The involved processes are enumerated in this figure:

1. A primary electron is scattered by the nucleus. Backscattered electrons (BSE) are electrons that leave the specimen after several scattering events.
2. Energy loss because of electron deceleration results in a continuum X-ray emission, the so-called bremsstrahlung.
3. The primary electron ionizes the atom, ejecting a secondary electron (SE).
4. An outer-shell electron relaxes to inner-shell.
5. One way of releasing the excess energy is the emission of an X-ray . The emitted X-ray has an energy which depends on the difference of energy between the different electron-shells and is characteristic for each element in the periodic table.

A typical measured X-ray spectrum is shown in figure 2.1(b) with the energy in x and the amount of detected X-rays in y direction. Characteristic X-rays form peaks, and X-rays from the bremsstrahlung form a continuous background. The elements of the specimen can be identified by the positions (energy) of the peaks. The specimen composition is calculated from peaks intensities with a quantification procedure which will be described later.

The intensity of a characteristic X-ray is directly linked to the primary beam energy through the cross section for inner shell ionization Q. The basic form of Q has been derived by Bethe [5]. In figure 2.2, Q is plotted as a function of the overvoltage ($U = E_0/E_c$) with E_0 the primary electron energy and E_c the critical ionization energy. Q starts quickly to rise when E_0 becomes higher than E_c, and a maximum is reached for an overvoltage of about three. As a rule of thumb for experiment, E_0 should be chosen at least two times higher than the energy of the peak with the highest energy that is expected to be found in the specimen.

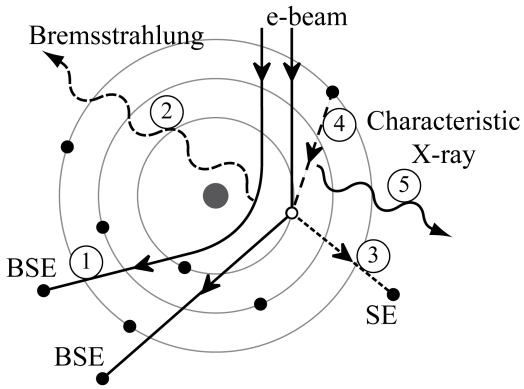

(a) Schematic picture of electron-atom interaction with the Bohr model for the atom. Waves represent the X-rays and straight lines the electron trajectories. The small black dots represent electron and the bigger one the nucleus.

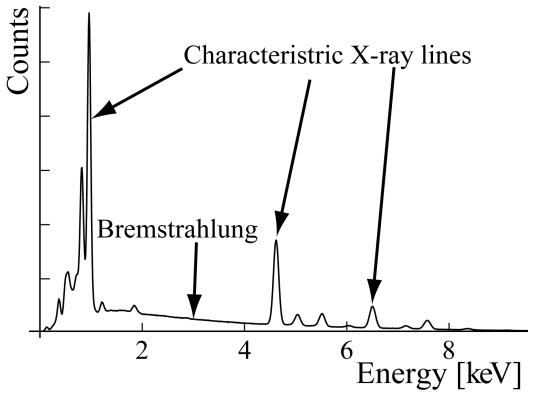

(b) Measured X-ray spectrum. Arbitrary units for the numbers of counts (N).

Figure 2.1: Electron-atom interaction and X-ray spectrum

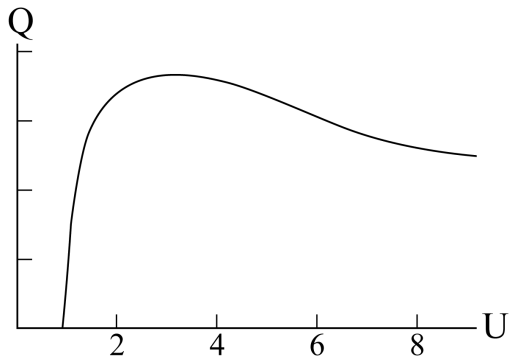

Figure 2.2: Cross sections (Q) for inner shell ionization in function of the overvoltage ($U = E_0/E_c$) (Bethe [5]). Arbitrary units for Q.

2.1.2 X-ray spatial distribution

The primary electrons enter the specimen and can interact several times before being absorbed or backscattered. The total volume containing all electron-solid interactions is called the "interaction volume". Not considering fluorescence, all X-rays are generated within this volume. Precise knowledge of this volume is crucial for the quantification procedure.

In a first step to characterize the interaction volume, the electron range R can be considered[1]. This range depends on the primary electron energy E_0 and on the specimen's density ρ. A general

[1]The electron range R is the maximum depth that electrons can reach in a bulk sample. It is given in nanometres.

form for the electron interaction range can be expressed as follow (Kanaya-Okayama [6]):

$$R = \frac{K}{\rho} E_0^k, \tag{2.1}$$

where K and k are constants (k is between 1.2 and 1.7). This relation can be extended for X-ray generation range (R_x) by Anderson and Hasler in the following equation [7]:

$$R_x = \frac{K}{\rho}(E_0^k - E_c^k). \tag{2.2}$$

In typical experimental condition, X-rays are generated in a depth from several hundred nanometres up to several microns.

Monte Carlo methods can be used to simulate the interaction volume. Random walk is used to calculate enough electron trajectories to have a representative population. The effects of inelastic and elastic scattering on the random walk are derived from appropriate physical models (textbook of Joy, chapter 1 [8]).

In figure 2.3(a), simulated electron trajectories are displayed for aluminium. The trajectories are projected on the xz-plane. Two colours differentiate absorbed (blue) and backscattered electrons (red). A typical round shape is obtained. Simulations demonstrate that low density material show a more pear-shaped volume. E_0 influences the size, but not the volume shape.

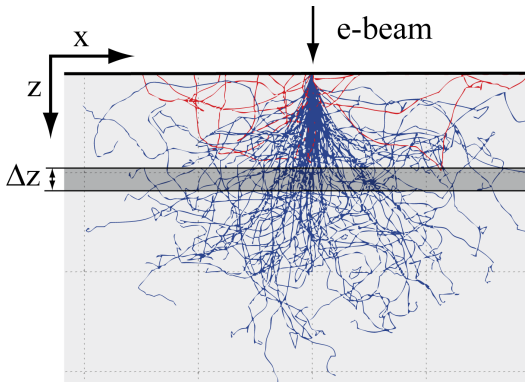

(a) Simulated electron trajectories, with absorbed electrons in blue and BSE in red. (Simulation with CASINO by Drouin *et al.* [9].)

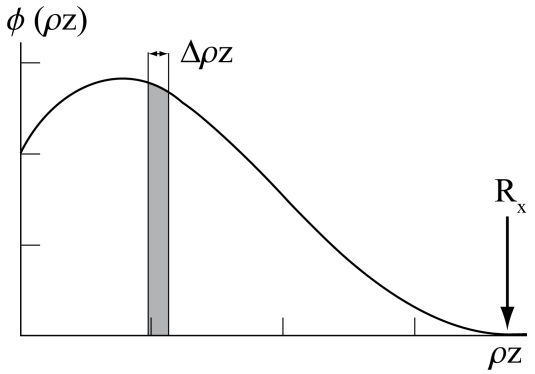

(b) General shape of $\phi(\rho z)$ curve. Generated X-ray distribution plots in function of ρz. (Simulation with DTSA-II by Ritchie [10].)

Figure 2.3: Electron and X-ray distribution. The regions drawn in grey are at the same depth and have the same width.

The simulation of electron trajectories can be extended to calculate the X-ray generation volume with an appropriate probability model. The figure 2.3(b) shows the simulated depth distribution of generated X-rays. The X-ray distribution ϕ is projected on the z axis, and mass depth ρz is used as abscissa. The obtained curve, the so-called $\phi(\rho z)$ curve, first increases to reach a maximum and then slowly decreases. The number of generated X-rays at a mass depth between ρz and $\rho z + \Delta\rho z$ is given by the area drawn in grey in figure 2.3(b), also illustrated with a grey region in figure 2.3(a). R_x is given by the end of the $\phi(\rho z)$ curve.

In quantification procedure, $\phi(\rho z)$ curves need to be accurately known. Simulations are in general not accurate enough, and an experimental approach is used, the so-called tracer technique [1]. Using buried thin films, some $\phi(\rho z)$ curves are measured and used to derive empirical models (*e.g.* extended Pouchou and Pichoir model, XPP [11]). In these models, care is taken that the total intensity of generated X-ray accurately corresponds to the area under the $\phi(\rho z)$ curve.

In the path to the surface, part of the X-rays is lost because of photoelectric absorption. The X-ray beam absorption through a film of thickness t is given by Beer's law:

$$I_{emit} = I_0 e^{-\frac{\mu}{\rho}\rho t}, \tag{2.3}$$

where I_0 is the primary beam intensity, I_{emit} is the intensity at the exit surface and μ/ρ is the mass absorption coefficient for the X-ray line in the specimen. Applying this equation to $\phi(\rho z)$ curve, the X-ray intensity emerging of a bulk specimen (I_{emit}) is given by:

$$I_{emit} = \int_0^\infty \phi(\rho z) e^{-\chi\rho z}\, d\rho z, \tag{2.4}$$

with $\chi = \mu/\rho \csc(\psi)$. The angle ψ is the X-ray emergence angle. Hence the absorption in a bulk specimen is derived and can be taken into account in the quantification procedure.

2.2 Dual beam FIB/SEM microscope

Virtually any analytical instrument is composed of a probe and a detector. As shown in figure 2.4(a), the probe interacts with the specimen. The response carrying specimen information is measured with the detector. In this work, a scanning electron microscope (SEM) is used; the probe is a focused electron beam. The response in form of X-rays is detected by an energy dispersive spectrometer (EDS detector)[2].

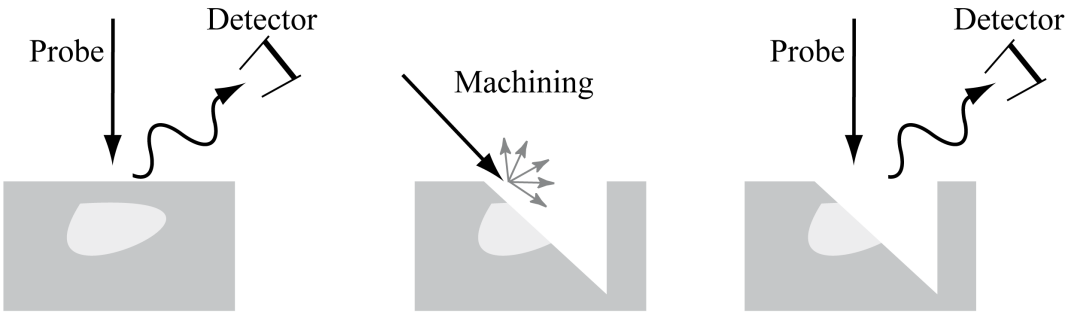

(a) Analyse. (b) Specimen machining. (c) Analyse of a new area.

Figure 2.4: Dual beam microscope: analytical instrument spatially extended.

To spatially extend the analytical instrument, it can be coupled with a machining tool, that physically removes part of the specimen (figure 2.4(b)). As shown in figure 2.4(c), a new area, previously hidden in the bulk, becomes accessible for a new analysis. In this work, the machining tool is a focused ion beam (FIB) part of the so-called dual beam FIB/SEM.

In this section, the three different parts of a dual beam FIB/SEM are introduced. Detailed technical description can be found in the textbook of Goldstein [4] (chapter 2 for SEM, chapter 7 for EDS) and in the textbook of Giannuzzi [12] (chapter 1 for FIB, chapter 2 for basic theory).

[2]The main detector for this work is the EDS. BSE and SE detectors are also commonly used.

2.2.1 Scanning electron microscopy (SEM)

The focused electron beam of SEM is characterized by the electron probe current i_p, the electron probe size d_p, and the electron beam accelerating voltage V_0. Scanning the specimen with the beam, a spatially resolved analysis is obtained. The result is usually displayed as a grey level image, the SEM image. If X-rays are recorded, an EDS map (spectral image) is obtained, in which each pixel contains a spectrum.

A SEM column can be decomposed in three main parts: the source, the condenser, and the objective as shown in figure 2.5(a). In the source, electron emission is obtained with an electron gun. The condenser is a system of condenser lenses and apertures, where the source is demagnified in the column in order to form a small probe. In the final part, the beam is focused on the specimen with the objective lens and position with scan coils. Lenses in a SEM are usually magnetic lenses.

The SEM column used in this work is a GEMINI® column (see figure 2.5(b)). Electron lenses suffer of high chromatic aberration at low-voltage condition; therefore, in a GEMINI® column, a high electron beam energy is maintained through the whole column, thanks to the beam booster which adds 8 kV to the electron beam. The energy is reduced to V_0 at the end of the column with an electrostatic end-lens. For a more detailed description of SEM techniques, see chapter 2 in the textbook of Goldstein [4].

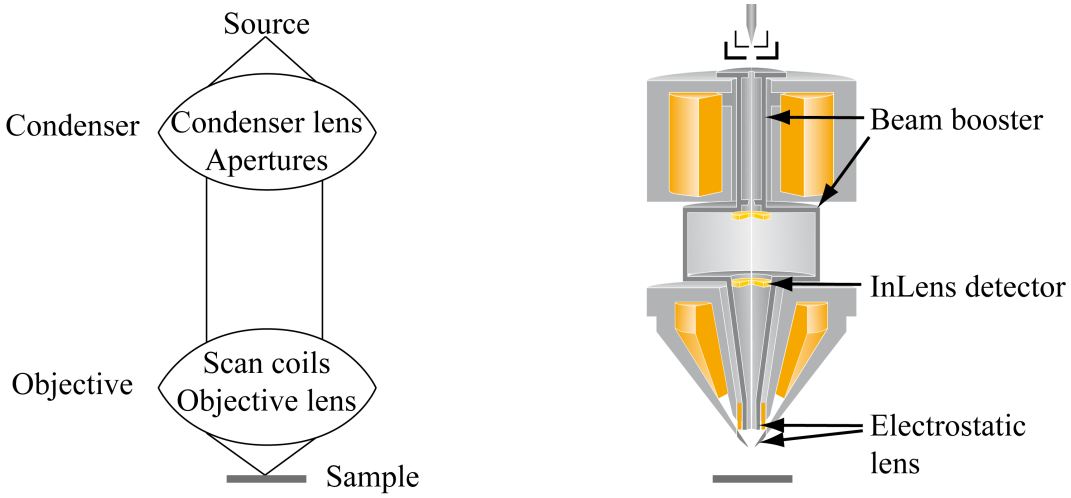

(a) The three main part of a SEM column. Electron path, without crossover, is indicated.

(b) Picture of a GEMINI® column. Pertinent devices are indicated. (Courtesy of Carl Zeiss.)

Figure 2.5: SEM columns.

2.2.2 Energy dispersive X-ray spectrometry (EDS)

In figure 2.6, the X-ray detection process in an energy dispersive detector is schematically drawn. The detector's main element is an intrinsic semiconductor, called detector crystal. The crystal sides are plated with an anode and a cathode. When a photon (X-ray) is captured and absorbed, electrons are promoted into the conduction band, and holes are left in the valence band. Electron and hole swept apart under the electrical field.[3] The X-ray energy is derived from the produced current.

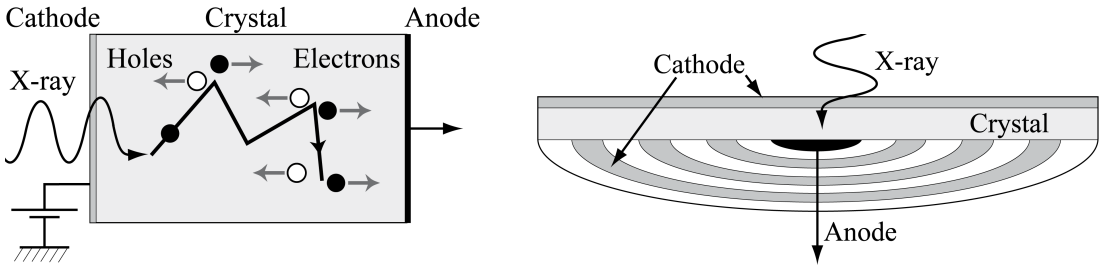

(a) The X-rays detection process in EDS detector. (Adapted from Goldstein [4].)

(b) Schematic geometry of SDD detector. (Courtesy of Oxford Instruments.)

Figure 2.6: EDS detector principle.

The theoretical limit for the energy resolution is about 115 eV for Fe Kα at 6.4 keV (see Goldstein, chapter 7 [4]). Current EDS detectors have an energy resolution close to this limit.

The measured current is weak. Electronic noise is reduced by signal averaging during a time up to some microseconds; the final energy resolution depends on this time, called process time. If a second X-ray is captured during the averaging time, the measure is rejected. The measurement rate, the count rate, is therefore limited for a given process time.

To improve this count rate limitation, a new type of EDS detector was developed and is now commonly used. Silicon drift detector (SDD) has a ring geometry as shown in figure 2.6(b). With this geometry, the anode capacitance is reduced. A smaller process time can therefore be used for the same level of noise, and higher count rates are reached [13]. Recently, SDD detectors with larger active surface have become available [14].

2.2.3 Focused ion beam (FIB)

Figure 2.7 illustrates schematically the main ion-solid interactions. The primary ion penetrates the specimen in a cascade of elastic collisions, generating amorphization. In this collision cascade, particles are sputtered away in the form of ions or neutral particles. Inelastic scattering events result in secondary electron (SE) emission. The primary ion is implanted or backscattered.

[3] The energy to generate an electron-hole pair is ~3.7 eV.

The FIB works in three different modes:

1. Using a high current, material is milled away.
2. At lower currents, the sputter rate (damage to the sample) is reduced, and secondary electrons or secondary ions are detected. The FIB can be used to image the specimen.
3. Material can be deposited by ion beam induced chemical vapour deposition (CVD). In this process, a precursor gas is injected close to the sample. Adsorbed on the surface, the molecules react under the ion beam to form a deposited layer.

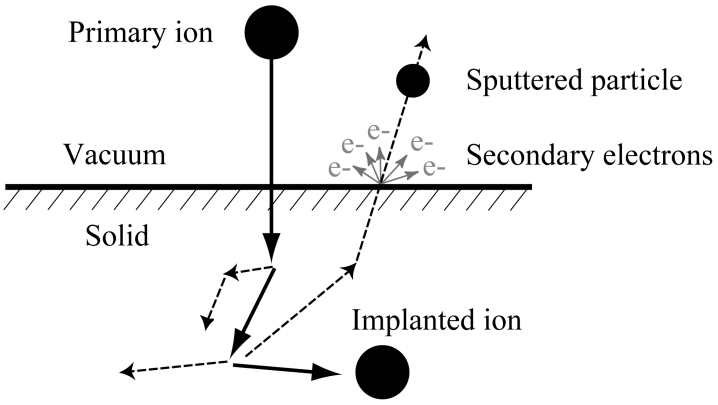

Figure 2.7: Schematic diagram of ion-solid interaction. (Adapted from Gianuzzi [12].)

The FIB is a scanning microscope; the column principle is similar to the one of a SEM column (see figure 2.5(a)). The FIB differs from SEM by the type of lenses (mainly electrostatic) and by the source. In the most common FIB, gallium ions are emitted from a liquid ion metal source (LMIS): the ion emission is obtained by field evaporation applying an electrical field to a filament wetted with liquid metal. Gallium is used, thanks to its physical properties, such as the low melting point.

2.3 3D EDS microanalysis

The first experiment of 3D EDS microanalysis was reported by Kotula *et al.* in 2006 [3], where 10 EDS maps were manually acquired. The experimental part of this technique has been essentially developed during the thesis of M. Schaffer [2]. Three articles were published out of her work: A) The first fully automated acquisition was reported [15]. B) The acquisition method was described in details [16]. This method is presented in this section. C) Sample preparation before acquisition was studied [17].

Only few other 3D EDS applications were published. Lasagni *et al.* characterized cast structures [18, 19, 20]. Scott and Ritchie simulated 3D EDS acquisition of a biological sample [21], and the corresponding measurements were just recently published [22].

2.3.1 Acquisition method and sample geometry

Before acquisition, the area to be analysed on the sample is prepared in the so-called "U-pattern geometry", as illustrated in figure 2.8. First the sample is tilted perpendicularly to the ion beam, and a protective layer is deposited on top of the area of interest. A trench is then milled in front of this area, in a way to create a uniform cross-section. This new surface, surrounded in red in figure 2.8(a), is called the "milled surface". The position of the beams given in this figure is described in details in the next section.

In the U-pattern geometry, three trenches are milled around the block of interest, as enumerated in figure 2.8(b). The width of the trenches is set taking into consideration the following constraints:

1. The front trench needs to be wide enough to access the whole milled surface with the electron beam.
2. As shown in figure 2.8(a), the EDS detector is on the left, the corresponding trench has to be wide enough so that all X-rays emerging from the milled surface can reach the detector.
3. During the run, the sputtered material partially redeposits on the side walls. To avoid masking of the milled surface, trenches on the side allow the accommodation of redeposited material.

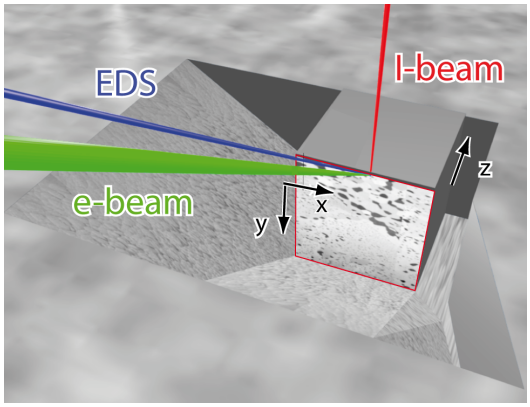

(a) Schematic view of a sample ready for acquisition. The position of the different beams is shown. The x, y and z axes are defined. The milled surface is surrounded in red. A protective layer is deposited on the block of interest. z axis shows the direction of sequential milling.

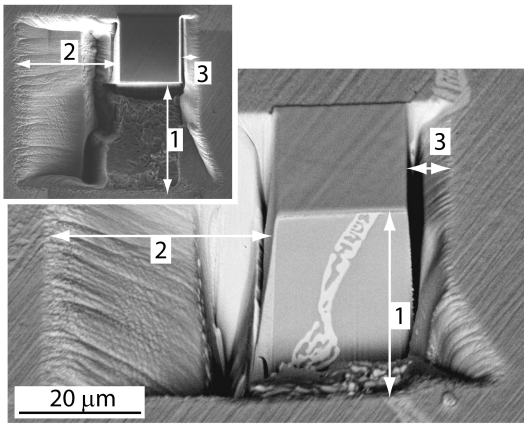

(b) SEM image of the prepared sample. The width of the block is 20 µm. The numbered arrows show the trenches width. Inset: FIB image of the sample.

Figure 2.8: Sample preparation in U-pattern geometry. The sample is tilted to be perpendicular to the ion beam.

During 3D EDS acquisition, a sequence of two steps is repeated sequentially. In the first step, the SEM image and an EDS map are acquired, and, in the second, a thin layer is milled away. These steps can be automated.

System geometry

The coordinate system of the 3D data is defined in figure 2.8(a). The x axis and y axis are parallel to the milled surface. The z axis is in the direction of the sequential milling.

The geometry of the complete system is defined by three angles, schematically drawn in figure 2.9. The first picture 2.9(a) shows α, the angle between SEM and FIB column. The sample surface is tilted by α. The milled surface, drawn by a dashed line, has a tilt angle which is complementary to α. The next two angles define the EDS detector direction; the azimuth angle (β) in picture 2.9(b) and the elevation angle (γ) in picture 2.9(c). The take-off angle (ψ), from the milled surface to the detector, is defined in the following equation [16]:

$$\psi = \arccos(-\cos(\alpha)\cos(\beta)\cos(\gamma) + \sin(\alpha)\sin(\gamma)). \tag{2.5}$$

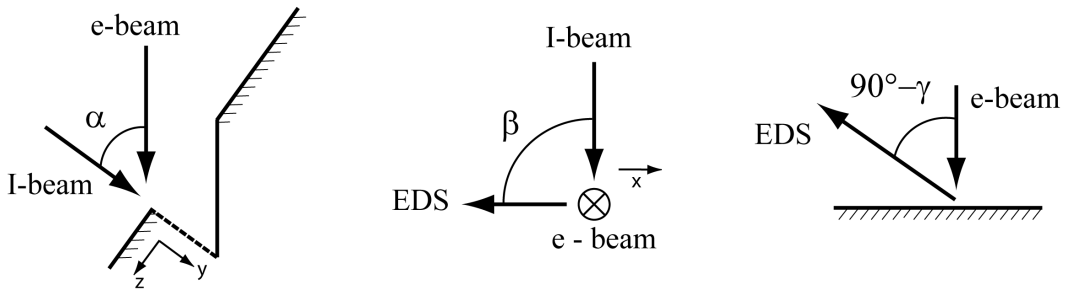

(a) Angle α between SEM and FIB column. The sample is tilted of α. The milled surface, the dashed line, has a tilt angle of (90°-α).

(b) Azimuth angle β, view from the e-beam. β is the angle between the plane formed by the EDS and the e-beam and the plane formed by the I-beam and the e-beam.

(c) Elevation angle γ, view from the normal of the plane formed by the electron beam and the EDS direction.

Figure 2.9: The three angles defining the system geometry.

Figure 2.10 defines the geometry for a single voxel of the milled surface. Formed by the ion beam, the surface forms the xy-plane. The electron beam and the ion beam are in yz-plane. The tilt axis for the electron-beam rotation is perpendicular to yz-plane, parallel to x. The EDS-detector direction is in the plane perpendicular to the untilted surface that contains the electron beam; thus the EDS detector is not in xz-plane but is perpendicular to yz-plane for $\beta = 90°$.

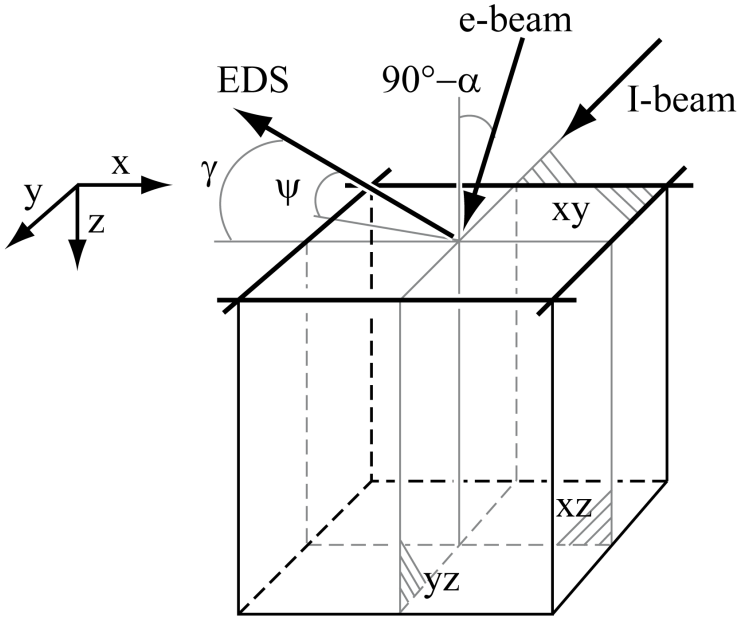

Figure 2.10: Geometry of a voxel with $\beta = 90°$. The two beams are in yz-plane. The ion beam is in the xy-plane. ψ is complementary to the angle between the normal of xy-plane and the EDS-detector direction. γ is the angle between EDS-detector direction and the intersection of xy-plane and xz-plane.

2.3.2 Limitations and artifacts

3D EDS microanalysis thus differs from 2D EDS mapping by the acquisition method and the sample geometry. This induces specific limitations and artifacts, discussed in this section. The subsections on sample geometry, noise, and interaction volume are the focus of chapters 4, 5, and 6 respectively.

Sample geometry

The U-pattern induces an artifact called "parasite X-rays ", schematically illustrated in figure 2.11(a). BSE or X-rays hit the surrounding walls, generating also X-rays. If these parasite X-rays reach the detector, an unwanted signal is added to the spectrum.

This artifacts was first reported by Schaffer *et al.* [17]. She suggested another sample-preparation geometry: the block lift-out. The block of interest is free of from the bulk, glued on a micromanipulator, lifted out, and glued on a TEM support. As shown in figure 2.11(b), the surface has no surrounding surfaces, hence no parasite X-ray. However the block lift-out is a time consuming technique.

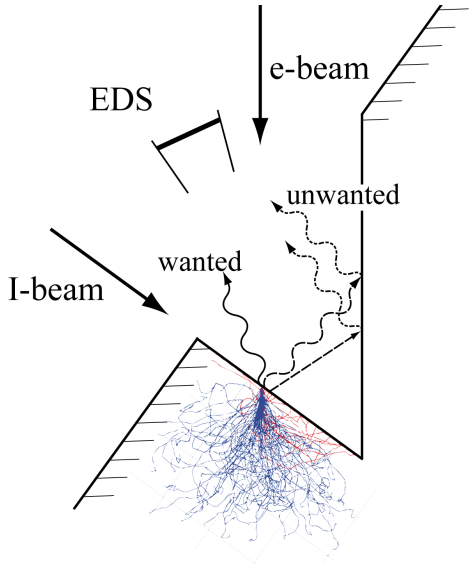

(a) Parasite X-rays are generated by BSE and X-rays hitting the surrounding. The sample has the same geometry as in figure 2.9(b). X-rays are represented as waves and BSE as straight lines.

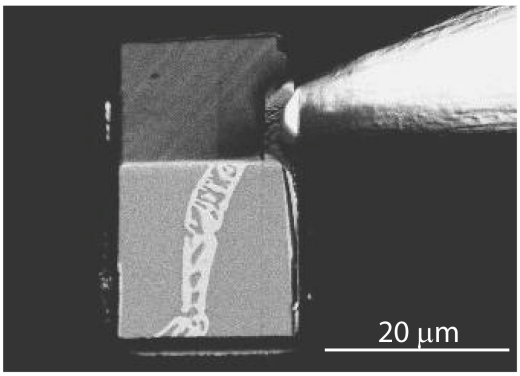

(b) Sample preparation by block lift-out method. The removed block is glued on a micromanipulator, on the upper right.

Figure 2.11: Parasite X-rays generation and block lift-out method.

Noise

X-ray emission is a random process over the time; the measured intensity depends on the X-rays counting statistics. Counting of independent (non-correlated) events follows thus Poisson statistics; the standard deviation σ of a distribution of counts or intensities has the following property:

$$\sigma = \sqrt{\bar{I}}, \tag{2.6}$$

where $\bar{I}$ is the mean value of the distribution. When determining the confidence limits of a calculated composition (the compositional precision), the variation in counting is the most important factor and the only one if the experimental conditions are ideally stable during the measurements.

In comparison with the compositional accuracy, the compositional precision has been treated only by few authors [23, 24]: Lifshin describes a procedure to determine the compositional precision due to counting statistics [25]. With a long enough acquisition time, high enough X-ray intensities

can be measured for each element in order to obtain a confidence interval $2\sigma_C$ below 1% relative for the composition[4]. However, given the high number of spectra to be acquired in a 3D EDS stack, the time per spectrum is limited. The obtained spectra suffer of noise; hence the counting statistics tends to be the most important source of error in composition determination.

Interaction volume

As the overvoltage U needs to be ≥ 2 for a given characteristic X-ray energy, the accelerating voltage V_0 depends on the X-ray lines to be measured. The interaction volume size varies with V_0 and also with the density of the sample (even locally); in most cases, it is bigger than spot size d_p by at least one order of magnitude. The interaction volume is the main factor limiting the spatial resolution, as will be further discussed in chapter 6.

Milling

The milling rate depends strongly on the incident angle of the ion beam. With glancing angle, the rate is several times higher than with perpendicular incidence [26], and the milling has a polishing effect. As shown in figure 2.8(a), the ion incidence angle on the milled surface is glancing (*i.e.* $\sim 89°$ from the normal of the xy-plane).

An artefact observed under these milling conditions is called the "curtaining effect". Because of roughness of the sample surface, the milling rate oscillates sharply across the cross-section. In the extreme case, the surface resembles undulating curtains [27]. To reduce this effect, the sample surface is smoothed by depositing a protective (structure less) carbon layer prior to any milling (see figure 2.8).

Drift

During the acquisition, global conditions of the whole system, such as temperature, may vary, inducing drift. This affects the microscope in two ways: sample movements and fluctuations in electrical components. The drift can be divided in FIB drift and SEM drift, as it can affects the milling or the image acquisition. FIB drift results in variation of the layer thickness, the voxel size in z direction. SEM drift results in image shift in x and y, image distortion and focus loss. Schaffer *et al.* describes a procedure for on-line drift compensation [16].

[4] 95.4% of the measurements fall within $\pm 2\sigma$.

2.4 Data processing

The multivariate statistical analysis (MSA) technique was adapted to EDS data by Kotula and Keenan [28]. It was tested on spectral images obtained by different techniques, among them 3D EDS microanalysis [3]. Technique improvements were later tested on the same data set [29]. This processing technique is the only reported one for 3D EDS data processing.

A 3D EDS data set is composed of a stack of SEM images and a stack of EDS maps, a stack of spectral images. An EDS map contains several thousand spectra, composed of thousand energy channels. For post-processing, such a data set requires different techniques which can be divided in the way data are considered: as individual spectra, as serial cuts or as a set of spectral images. This section is subdivided along these three types of data; each subsection describes the corresponding processing technique.

2.4.1 Spectrum

The quantification procedure for EDS spectrum is described in this section. Since the first steps of Castaing in 1951 [1], it was widely studied. Detailed description can be found in various textbooks (*e.g.* Goldstein in chapter 6 [4]).

Quantification

In the first step of the procedure, X-ray line intensities are extracted from the spectrum. First the background is removed, usually applying a top-hat filter on the spectrum. If two peaks overlap, a correction procedure is applied, usually a least square fitting. After these corrections, X-ray line intensities are given by the area under the peaks. Because of the low energy resolution of EDS, the accuracy in extraction has a strong influence on the final accuracy, especially in difficult cases such as strong overlaps. This problem is discussed in details by Statham [30].

X-ray line intensities are extracted from two spectra: one measured on the sample (I_{corr} for background corrected) and one measured on a standard (I_{std})[5]. If I_{corr} and I_{std} are measured in the same conditions, the ratio between them gives, in a first approximation, the concentration of the considered element in the sample. This ratio, called k-ratio, is corrected by the so-called ZAF factor in order to obtain an accurate composition:

$$\text{k-ratio}_A = \frac{I_{corr,A}}{I_{std,A}} = \text{ZAF}\frac{C_A}{C_{std,A}} \tag{2.7}$$

where C is the concentration of the A element. Z, A, and F are the correction factors for the effects due to the different overall compositions of sample and standard. These matrix effects are expressed in three different ways: Z, A and F. Density variation induces variation in X-ray spatial

[5] A microanalysis standard is a reference sample with a known composition. I_{std} has been corrected for background.

distribution (Z). Absorption (A) and fluorescence (F) depend on the different elements present in the sample.

Among the different methods to determine ZAF correction factors, the most widely used, the XPP $\phi(\rho z)$ method from Pouchou and Pichoir is presented here [11]. In this method, the $\phi(\rho z)$ curve is described through a semi-empirical parametrisation. The $\phi(\rho z)$ curve is linked to the emitted intensity with the following equation:

$$I_{emit,A} \propto C_A \mathrm{F} \int_0^\infty \phi(\rho z) \mathrm{e}^{-\chi \rho z} \, \mathrm{d}\rho z, \tag{2.8}$$

where F is the fluorescence factor for the X-ray line in a material of composition C. The integral gives the total X-ray intensity corrected for absorption (see equation 2.4) and, hence, described the Z and A correction factors. In most cases, F is the less important factor. Z, A, and F factors depend on C; consequently an iterative procedure is used to determine ZAF and C. Testing the quantification method on a database of 1113 analyses of Bastin *et al.* , it was shown that 97% of the results fall within ±5% relative error [31].

Thin-film quantification

The quantification procedure described before requires an ideal sample that is homogeneous over the full range of the interaction volume; the microvolume needs to be homogeneous. An extension of procedure to heterogeneous microvolume is possible if the microstructure is known, as in the case of thin films on a substrate. If realistic $\phi(\rho z)$ curves of the layered material are defined, the intensity of one X-ray line generated in one layer can be derived by partial integration. Among the different types of approaches to quantify thin films, one type supposes that $\phi(\rho z)$ curves are continuous. This assumption allows fast computation of k-ratios for any system. The thin-film quantification adapted from XPP $\phi(\rho z)$ method is based on this assumption [32].

In practice, the layer system is defined with all the a-priori knowledge. Guesses are given for the unknown thickness or/and composition. To be solved, the system needs at least the same number of inputs, the k-ratios, than of unknowns. For instance, with k-ratios measured at one accelerating voltage, the unknowns can be the thickness and the normalized composition of a layer. The system is resolved through an iterative procedure. In the iteration, k-ratios are predicted with the current system; the predictions are used to refine the next system. The iteration is stopped when a convergence criteria is reached. In unfavourable cases with elements common to different layers, the iteration can converge to a local minimum or may not converge in the limit of iteration steps. In such cases, k-ratios measured at several V_0 should be used.

Since the two $\phi(\rho z)$ methods presented are used in this work, the method for homogeneous sample is referred as "bulk quantification", and the one for layered material is referred as "thin-film quantification".

2.4.2 Serial cuts

Serial cuts refer to a physical removal of slices as it is done in FIB nanotomography. This section presents the required steps to process serial cuts for FIB nanotomography. Extensive description can be found in the textbook of Russ [33]: registration in chapter 13, smoothing and nonuniform illumination in chapter 4, segmentation in chapter 7. For the surface rendering, refer to Ohser and Schladitz in section 3.6 [34].

Registration

The drift induces misalignment of subsequent images in x/y.[6] Automated registration procedures are used to precisely align the slices with respect to each other. In the method developed by Thévennaz, the mean square intensity difference between two successive images is minimized [35]. A pyramidal approach is used to avoid local minimum. In the coarsest step, images are severely blurred and aligned. The alignment is iteratively refined using less blurred images until a subpixel accuracy is reached.

Smoothing

SEM images suffer of Gaussian noise because of low counting statistics. Noise-reduction filters can be applied for better visualisation and better demarcation of features for later measurements. Neighbourhood averaging filters are often used as smoothing filter, but these techniques tend to blur edges. A classical edge-preserving smoothing filter is the median filter, a neighborhood ranking filter. The value of the central pixel is set to the median value of a neighbourhood defined by a kernel. Edge-preserving filters are improved with kernel size adapted in function of local properties of the image.

Nonuniform shadowing

The vicinity of a surrounding at the emerging position of electron can influence the final detection rate. In U-pattern geometry, the surrounding proximity varies with the position on the milled surface. Because of this, SE images show a nonuniform shadowing effect. BSE are less influenced because of their higher energy. To correct this effect, a background containing the nonuniform shadowing is subtracted from the original image. The background can be calculated by low-pass filtering of the original image.

Segmentation

One aim of 3D image processing is to automatically divide (segment) the analysed volume into phases of uniform properties. Supposing that the properties are characterized by the image

[6] Rotation and scaling do not have to be considered in this case.

brightness, a phase can be isolated defining a range of grey level. This method is called global thresholding.

Surface rendering

A system of several phases is obtained from segmentation. To obtain the surface of the different phases, the borders are transformed in a set of triangles with an algorithm such as the marching cube (Ohser's textbook, section 3.6 [34]). 3D visualisation with illumination effects can then be computed from this surface.

2.4.3 Spectral image

Spectral images often contain too large amount of data to be efficiently analysed. Techniques of data mining have been developed to help an user interpreting spectral image. For instance in a very common one, all spectra are scanned to find peaks above background. Overview of data mining techniques for EDS maps are described in the review of Friel and Lyman on X-ray mapping [36] .

Multivariate statistical approach (MSA) and principal component analysis (PCA)

A complete description of MSA methods can be found in the textbook of Malinowksi [37]. MSA methods such as the weighted principal component analysis (PCA) are used to identify correlations in data set, for instance elemental phases in the case of EDS maps. PCA aims to find directions that explain the highest data variation. These directions, the so-called principle components, reveal correlations in data. This is illustrated for a simple case in figure 2.12 with a data set of two variables. Applying the PCA, two directions are obtained. Direction 1 represents data the best: most of data variance is defined in this component. Direction 2 is set perpendicular to direction 1.

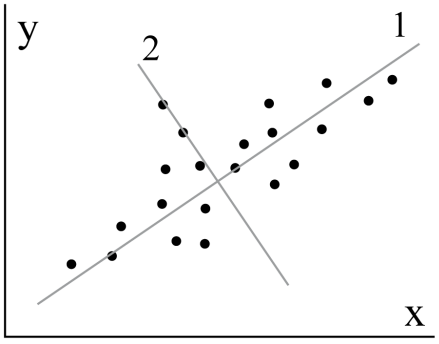

Figure 2.12: A data set of two variables, x and y. Direction 1 is responsible for most of variance. Direction 2 is perpendicular to direction 1.

For a stack of spectral images, the data are arranged in a data matrix **D** composed of m voxels and n energy channels and scaled (weighted) to take into account the statistical nature of the noise, in our case Poisson statistic [38]. This matrix is decomposed by weighted PCA in:

$$\mathbf{D}=\mathbf{T}\mathbf{P}^T, \tag{2.9}$$

where **T** is the score matrix, the images, and $\mathbf{P}^T$ is the transpose of the loading matrix, the spectra. **D** is written as a linear combination of **T** and **P**. Components (**T**+**P**) are sorted according to their eigenvalues, which represent the amount of variance expressed by a component. Dimensionality of the original dataset can be reduced by carefully selecting components representing most of the data. The data can then be reconstructed using only the more meaningful components, leaving apart the noise.

PCA is used with EDS data with two different aims: 1) as a data mining technique interpreting the principal components in a qualitative analysis [28], and 2) as a noise-filter to improve quantitative analysis [39]. For the first application, a main drawback of PCA is that loadings and scores can have negative parts; they have no physical meaning. Many methods have been applied to overcome this drawback. All aim to recover a physical meaning in the components, such as factor rotation [40].

3 Materials and method

3.1 Materials

The samples were selected so that they are suited for this work's objectives. Generated data have to be appropriate for developing processing techniques and free of sample specific artifacts; the required "ideal" sample is:

- conductive, free of charging effects,
- dense,[1]
- well studied and well known to assess the developed techniques,
- with a microstructure size in the range of the desired spatial resolution,
- and with a set of non-overlapping X-ray lines.

Metals can fulfil these requirements. Metallic samples are conductive and often dense. They have generally a high milling yield that helps preventing curtaining effect and reduces the overall milling time. Metallic alloys form intermetallic phases of known composition. The microstructure size can be controlled to some extent by heat treatment.

Two samples were selected. Each sample has a specific function:

- A test-case sample for the development of the processing technique. The sample is easy to model with a known microstructure and a known phase composition.
- A real-case sample for testing the processing technique. The sample has a complex microstructure and complex phase composition, for which 3D EDS microanalysis is an ideal characterization technique.

The test-case sample is an Al-Zn alloy, and the real-case sample is the weld between nickel-titanium (NiTi) and stainless steel. These samples were extensively studied in two recent theses:

[1] In porous materials, X-rays are emitted from different planes.

by J. Friedli for the AlZn sample [41] and by J. Vannod for the weld sample [42]. These samples are described in the two first subsections. In a third subsection, other used materials are presented.

3.1.1 Al-Zn alloy: test-case sample

Friedli investigated certain types of growth morphologies in Al-Zn alloys [41]. Figure 3.1(a) shows the Al-Zn phase diagram [43]. Below 277°C, aluminium is not miscible with zinc. At equilibrium the alloy is composed of two almost pure phases.

An Al-Zn alloy with 78 wt.% Zn was prepared from 99.995 wt.% purity base metals. The alloy was first molten and then quenched. Following a specific heat treatment, the alloy underwent a solid state decomposition. The SE image of figure 3.1(b) shows the obtained microstructure. The Aluminium phase forms black round-shaped particles smaller than a micron, and the white matrix corresponds to the zinc phase. This simple microstructure is suitable for a test-case sample.

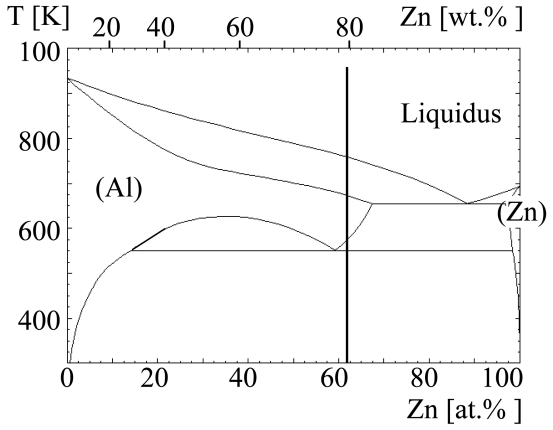

(a) Aluminium-zinc phase diagram [43]. The vertical line shows the primary alloy composition.

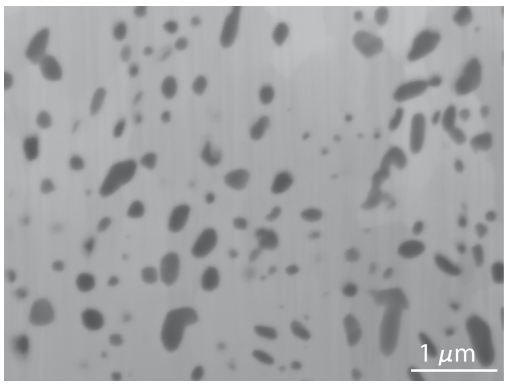

(b) SE image at 5kV. Aluminium particles appear in dark grey.

Figure 3.1: Al-Zn alloy.

3.1.2 NiTi-stainless steel laser weld: real-case sample

NiTi plays an important role in biomedical engineering thanks to its properties, such as shape memory and biocompatibility. In order to extend the range of applications, NiTi is joined with other biocompatible alloys such as stainless steel. Vannod applied a laser welding technique to join NiTi wires and stainless steel (SS) wires [42]. The fracture behaviour was investigated by mechanical testing, modeling, and microstructural characterization.

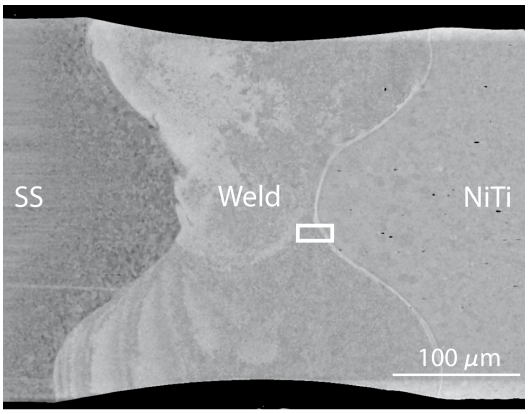

(a) BSE image of a longitudinal cut through the weld. SS wire is at left, and NiTi wire is at right the NiTi. The white rectangle defines the region of the 3D EDS acquisition.

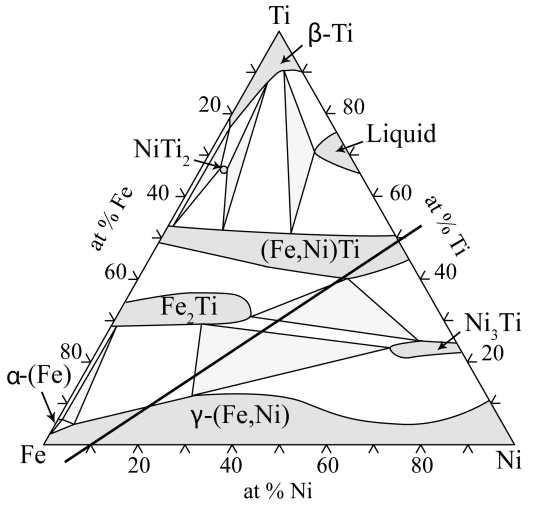

(b) Fe-Ni-Ti ternary phase diagram, isothermal cut at 1000°C [45]. The black line connects the composition of the base wires.

Figure 3.2: NiTi-SS laser weld.

The sample was produced by welding wires of NiTi (56.4 wt.%Ni) and stainless steel (grade 304L), 300 μm in diameter. The welding was performed using a pulse laser coupled to an orbital welder. Laser parameters were adjusted to reach a complete transverse weld. Prior to observation, a mirror-polished longitudinal section was prepared from the welded wires. This section is shown in the BSE image of figure 3.2(a). In this work, this sample is refereed as NiTi-SS.

The meniscus shape of figure 3.2(a) corresponds to the welded region. The interface between the welded region and the unmelted NiTi wire is of particular interest: cracks form systematically in this region [44]. This particular crack location was shown to result from stress concentration. In order to assess that this failure is not favoured by brittle intermetallics, an extended knowledge of the microstructure is needed. The microstructure at the crack location was thus investigated, in the region defined by a white rectangle in figure 3.2(a).

To comprehend the complex microstructure of the welded joint, phase diagrams are considered. The three main elements are titanium, iron and nickel. An isothermal cut at 1000°C of a ternary Fe-Ni-Ti phase diagram is shown in figure 3.2(b) [45]. The black line connects the two initial phases, the stainless steel on the left corner and the NiTi on the middle right. Following the diffusion path theory described by Kirkaldy *et al.* [46], the phases possibly present are those present in the phase domains crossed by this black line. Four different phases can form in the present case. During sample production, the weld is molten and a mixing process driven by Marangoni-convection takes place. The resulting microstructure is complex in a geometrical and a compositional sense. 3D EDS microanalysis is an appropriate technique for this complex case, and the sample is typical for a real-case sample.

3.1.3 Other materials

Nb_3Sn strands

To measure parasite X-rays, a sample of Nb_3Sn strands was chosen. Figure 3.3(a) shows a sample cross-section prepared by mechanical polishing. Smaller than 10 µm in diameter, the strands form groups of 100 µm.

The Nb_3Sn strands are produced by "bronze route" as illustrated in figure 3.3(a). The strands are composed of Nb-7.5 wt.%Ta and are embedded in a bronze matrix composed of Cu-15.5 wt.%Sn. During a heat treatment of 100 hours at 650°C, the tin diffuses into the strands forming Nb_3Sn phase. After heat treatment, an unreacted Niobium heart can remain. The samples were provided by the group of Flückiger *et al.* [47].

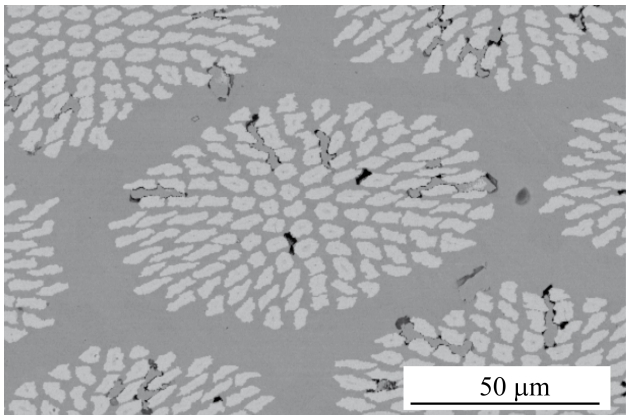

(a) BSE image at 10 kV of a cross-section. In light gray, the strands are grouped in array. The black area in between strands are pores.

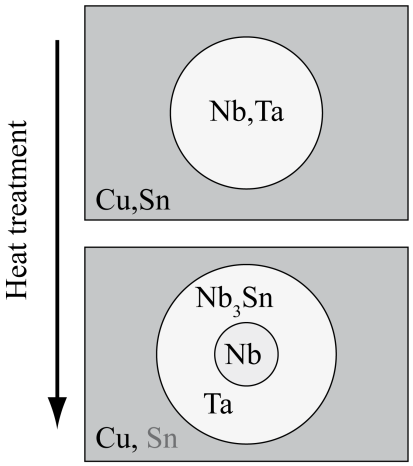

(b) Schematic picture of bronze route. During heat treatment, Sn diffuses in the Nb strand to form Nb_3Sn.

Figure 3.3: Nb_3Sn strands produced by bronze route.

Microanalysis standards

The martensitic transition temperature of NiTi is strongly linked to nickel / titanium ratio [48]. This ratio is certified and impurities are guaranteed below 0.1 wt%. NiTi base wire was used as a microanalysis standard for Ni and Ti. For the other analysed elements, pure materials, mounted on a support (44 Metals Standard Mount, Structure Probe Incorporation supplies), were used.

3.2 Method

Dual beam, acquisition method, and data processing are described in section 2.2, 2.3, and 2.4. Instrument characteristics, experimental conditions and computing methods are presented in details in this section.

3.2.1 Instrumentation

The dual beam FIB/SEM is a Carl Zeiss Nvision40. The electron column is a GEMINI® column with a Schottky field emitter. Company specifications give a probe size i_p of 1.1 nm at 20 kV and of 2.5 nm at 1 kV.

The ion column is a 100 nm zeta FIB column from SIINT. Company specifications give a probe size of 4 nm at 30 kV. The ion probe current ranges from 0.1 pA to 45 nA. 5 different gases can be injected through a nozzle. Two of these gases are precursors for conductive deposition: carbon and platinum.

The EDS detector is an Oxford Instrument X-Max with 80 mm^2 detection area. A 123.2 eV energy resolution (FWHM of Mn Kα peak at 5.9 keV) was measured applying the method of Alvisi *et al.* [49].

The Nvision40 geometry (see section 2.3.1) is defined by an angle between SEM and FIB column α of 54°, elevation angle β of 35°, and an azimuth γ of 90°. Applying equation 2.5, a take-off angle (ψ) of 27.5° is obtained.

In the Nvision40, the coincidence point between the SEM column, the FIB column, and the EDS detector is at a working distance (WD) of 5 mm. With a distance between the sample to the crystal estimated at 30 mm, the detector solid angle is 0.0125 sr.

A stable microscope is crucial to minimize drift. Vibrations are attenuated by an isolating support structure (Table Stable, Ammerbuch, Germany). A cancelation system reduces magnetic field interference (SC22, Field Cancelation System, Spicer Consulting, Santa Cruz, USA). Temperature variations of the microscope room are controlled by air conditioning. The whole system is monitored regularly over the year.

Electron detectors in GEMINI® column

Apart from classical electron detectors, GEMINI® system has another SE detector, called InLens detector. It is installed inside the column, and its principle is illustrated in figure 3.4. In the column, the beam booster is at a high positive voltage, attracting part of the emerging electrons. After the objective lens, BSE and SE focal points are different because of chromatic aberration and the difference of energy. An annular detector is positioned at the BSE focal point in order to collect SE[2]. InLens detector is efficient for low energy SE, hence surface sensitive.

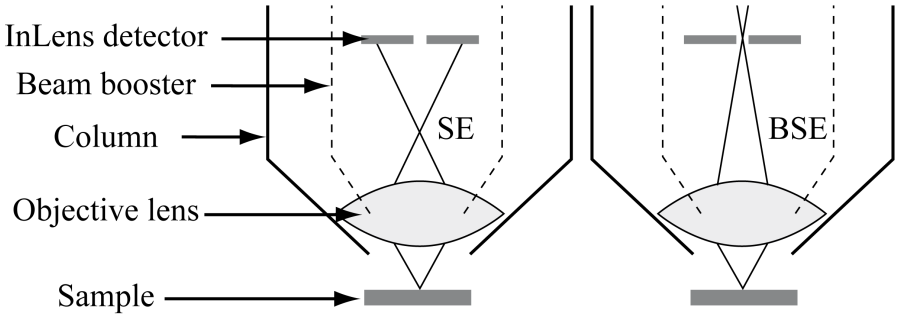

Figure 3.4: Schematic path of SE and BSE beam back inside the GEMINI® column. Electron paths are drawn with thin lines. (Courtesy of Carl Zeiss.)

3.2.2 Acquisition conditions

In this section, the experimental parameters of 3D EDS acquisition are presented for AlZn and NiTi-SS samples. The ones for Nb_3Sn strands are given in a following subsection. Table 3.1 gives the X-ray lines chosen for quantification. These lines form the lowest-energies set that does not suffer from overlapping peak due to the limited resolution of the EDS detector.

Table 3.1: X-rays lines and energies for the analysed elements.

	AlZn		NiTi-SS					Nb_3Sn strands			
	Al	Zn	C	Ti	Cr	Fe	Ni	Cu	Nb	Sn	Ta
Lines	Kα	Lα	Kα	Kα	Kα	Kα	Lα	Lα	Lα	Lα	Mα
E [keV]	1.49	1.01	0.28	4.51	5.41	6.40	0.85	0.93	2.17	3.41	1.71

[2]The BSE focal point depends neither on the working distance (WD) nor on the accelerating voltage (V_0), as the focal length of the objective lens is the sample-to-lens distance when the image is on focus.

3D EDS acquisition

The parameters for EDS spectra are given table 3.2. Spectra recorded under these conditions are shown in figure 3.5. The accelerating voltage was set to excite efficiently all X-ray lines. The process time was set as low as possible so that X-ray lines do not overlap. The probe current i_p was adjusted to a 50% dead time, the relative time of rejected X-ray measurements. The Al Kα peak is far from Zn Lα peak (see figure 3.5(a)); the second-shortest process time was used (p2), and a high count rate was reached. The Ni Lα peak is close of Fe Lα peak (see figure 3.5(b)); the third-shortest process time was used (p3). Given in table 3.2, the dwell time is the acquisition time per spectrum. The acquisition time per map was adjusted to record several maps per hour. With the low time per map of the NiTi-SS sample, many maps (44 maps as given in table 3.3) are recorded in a relatively short total acquisition time. But the corresponding dwell time is low, and the spectrum is noisy 3.5(b).

Table 3.2: Parameters for EDS spectrum acquisition. "t." stands for time. "Dwell t." is the acquisition time per spectrum. "Rate" is the count rate (rate of detected X-rays). "Total t." is the total acquisition time for the 3D acquisition.

	V_0 [kV]	i_p [nA]	Rate [kct/s]	t. per map [s]	Dwell t. [ms]	Total t. [h]
AlZn	5	9.2	95	810	66	35
NiTi-SS	10	2.8	40	355	29	6

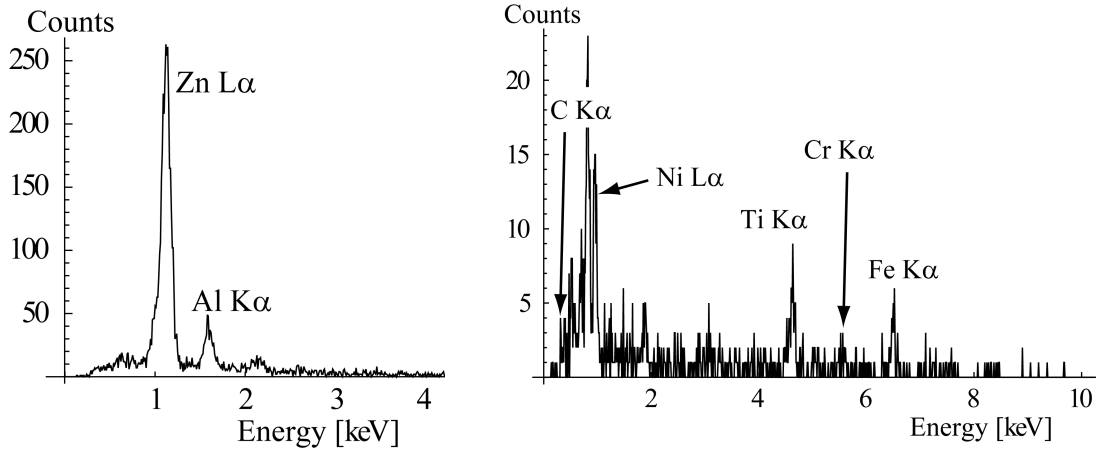

(a) AlZn spectrum.

(b) NiTi-SS spectrum.

Figure 3.5: Spectra of one voxel recorded in conditions of table 3.2. The set of X-ray lines of table 3.1 are indicated.

Spatial parameters are given in table 3.3. All voxels are isotropic. Voxels of SEM images are 8 times smaller than EDS maps ones. SEM images were recorded with InLens detector for both samples. The FIB probe current used for sequential layer milling is 700 pA, at 30 kV. The U-pattern milling geometry was used.

Table 3.3: Spatial parameters of the acquisitions.

	AlZn		NiTi-SS	
	EDS maps	SEM (InLens)	EDS maps	SEM (InLens)
Voxel size [nm^3]	40 x 40 x 40	5 x 5 x 5	100 x 100 x 100	12.5 x 12.5 x 12.5
No. Voxels	128 x 96 x 131	1024 x 768 x 616	128 x 96 x 44	1024 x 768 x 352
Stack size [μm^3]	5.12 x 3.84 x 5.2		12.9 x 9.6 x 4.4	

Drift

Before starting the acquisition, the microscope was let to stabilize in the acquisition condition for several hours. During acquisition, focus and astigmatism was checked about every six hours. This approach was also used for FIB nanotomography performed on the same microscope. With several thousand images of 10 x 10 x 10 nm^3 voxel size recorded during several days, subsequent images showed a minimal drift [50].

The acquisition time for a single EDS map is, at least, one order of magnitude higher than for one SE image. The risk of drift during EDS map acquisition is proportionally higher. To minimize this effect, several fast scans are summed up for one EDS map, and the image shift is compensated by image correlation (SEM image) between the scans.

2D map and spectrum acquisition

The EDS maps acquired on the NiTi-SS sample during the 3D acquisition are especially short. Prior to the 3D acquisition, a 2D EDS map was recorded with a dwell time 10 times longer (300 ms dwell time, one hour for the whole map). The other acquisition parameters are identical (see table 3.2 and 3.3).

For microanalysis standard, spectra are measured with the parameters of table 3.2, except the dwell time of 30 s. Standards were tilted by 36° to have the same geometry.

Nb_3Sn-strands sample was prepared in U-pattern geometry. But only 2D EDS maps and 1D spectra were acquired, as this sample was only used to investigate the parasite X-ray artefact. The set of X-ray lines is given in table 3.1. The lines are close; the second-longest process time was used (p5), and a count rate around 10 kct/s was reached. Spectra were recorded at 7 kV, 12 kV, 16 kV, and 20 kV with a dwell time of 30 s. The map was acquired at 7 kV during 14 hours with a dwell time of 1.5 s. The map is composed of 190 x 180 pixels with a size of 10 x 10 nm^2.

3.2.3 Computing

Data processing

For SEM stacks, the procedure described in chapter 2.4.2 on serial cut is applied. The spatial resolution in SEM images is usually better than the one in EDS maps. The SEM stack is used as reference to register all stacks of the data set. A first order 3D median filter is used for smoothing. The background to correct shading effects is obtained from a mean filter with a kernel size of 150 pixels.

The procedure of standard quantification defined in chapter 2.4.1 is applied on X-ray spectra. K-ratios are extracted with a home-made script. Background is removed by a top-hat filter with a kernel size adapted in function of the X-ray energy, as described by Statham [51]. Since the sets of X-ray lines are free of overlap, no peak deconvolution has to be applied. The intensity is given by the area under the peak between two limits. The limits are finely tuned comparing spectra from stack, scaled with k-ratio, with spectra measured on the standard. Principal component analysis (PCA) is applied on the raw EDS maps with a script developed in the laboratory[3] [52].

Simulations

NISTMonte is a publicly available tool for Monte Carlo simulations [10]. It was chosen because complex geometries can be simulated in a reasonable time and scripting is possible. Tested on the thin-films database of Bastin *et al.* [53], a simulation accuracy of 20% was demonstrated for most of the systems [54]. To test our simulation system, we used the same database with systems close to AlZn sample.[4] A satisfying accuracy was found with a relative mean error lower than 5%.

The two case-study samples were studied with simulations. The simulation parameters, V_0 and voxel size, as well as the simulation geometry are set in accordance with the measurements. The analysed surface is flat and no surrounding is set around it. For accurate spectrum simulation, the modelled detector is defined based on detector characteristics from company specifications and on measured spectra.

For electron or X-ray distributions, a one phase sample is simulated. For a good precision, a high number of electron trajectories is required, typically hundred thousands. Electron distributions are obtained by counting electrons going through a cubic bin. X-ray distributions are obtained gathering the probability of generating X-ray in the cubic bin. X-ray distributions are corrected for absorption effects.

For model acquisitions, a two phase sample is simulated. Profiles and 3D acquisitions are

[3] G. Lucas has implemented PCA in plugins for Mathematica® 8.0 and DigitalMicrograph™. They are freely available on request.

[4] The measurements used for the test are aluminium films of thicknesses from 10 to 320 nm on a copper substrate. The k-ratios were measured at 6 kV.

simulated on planar interfaces and spherical particles respectively. The interface between phases is sharp, there is no diffusion. Less electrons are used, typically ten thousands. Simulated standards were used to obtain k-ratios.

Software

The dual beam is controlled by SmartSEM® software from Carl Zeiss. The 3D EDS acquisition is driven by INCA® from Oxford Instrument.

The whole post-processing procedure is controlled with a home-made scripts in Mathematica® 8.0. Parts of the procedure are processed with other softwares:

- Stratagem® software from SAMx for EDS spectrum quantification ($\phi(\rho z)$ method),
- ImageJ software with the stackreg plugin for image registration [35],
- CASINO v2.42 by Drouin *et al.* for Monte Carlo simulation used for electron-trajectory pictures [9],
- DTSA-II, based on NISTMonte, by Ritchie for all other simulations [10],
- and Avizo® fire 7.0 (VSG) for 3D visualizations.

Acquisition automation

At the beginning of this work, no commercial solution for 3D EDS acquisition was available. A solution was developed using AutoIt -a freeware that uses a combination of simulated keystrokes, mouse movement and window control. With this software, sequential commands of milling and imaging are sent to dual beam and EDS softwares. Oxford Instrument developed later a commercial solution. The solution was beta tested during this thesis, and all data of this work were acquired with this solution.

4 Parasite X-rays

An important part of the preparation for a 3D EDS acquisition is the selection of the volume of interest and the milling of the trenches to get access to the region of interest. The U-pattern geometry as described in section 2.3 has some advantages over other techniques. It can be applied on any polished surface of a sample, it is faster than the block lift-out method, and it required less user's ability; this is why the technique is often preferred. The technique has a specific artifact, the parasite X-rays, and an extended knowledge of it is needed.

4.1 Measurement method

Parasite X-rays are generated in the surroundings trench walls; an element not present on the milled surface, but present in the surroundings, can serve as a parasite-X-rays indicator. The corresponding peak in the EDS spectrum is the direct measurement of parasite X-rays .

Schaffer *et al.* demonstrated qualitatively the parasite-X-rays artifact in an "*ex-situ*" experiment [17]. Glued on a micromanipulator, a block of material was placed in a cavity of different composition. Parasite X-rays were revealed comparing EDS measurements in vacuum and in the cavity.

Based on the specific microstructure of a sample, an "*in-situ*" approach is developed in this work. The sample is composed of parallel Nb_3Sn strands that form groups and that are embedded in a copper matrix. U-pattern preparation is executed in way to obtain strands on the milled surface, but not in the surrounding. Nb_3Sn strands being free of copper, this element serves as the parasite X-rays indicator.

The milling pattern for U-pattern preparation is shown in figure 4.1(a). The area of interest is over a Nb_3Sn-strands group. The trenches that are outside the area of interest cover only the matrix. Indicated with a dashed line in figure 4.1(a), the milled surface contains strands and faces trench walls only containing copper.

4.2 Results

In a first step, a geometry free of parasite X-rays is compared with U-pattern geometry. Figure 4.1(b) shows the corresponding spectra measured on Nb_3Sn strand. Spectrum 1 is recorded at position 1 of figure 4.1(a) with no tilt[1], and is thus free of parasite X-rays . Spectrum 2 is recorded at position 2 of figure 4.2 in the U-pattern geometry. Both are representative spectra from a series of measurements.

Spectrum 1 shows a small peak of Cu Lα. Nb_3Sn strands contains a little amount of copper in the grain boundaries because of diffusion, as observed by Cantoni *et al.* [55]. We measure a copper content lower than 1 wt.% with several EDS analyses at 7 kV and 20 kV. Spectrum 2 has a Cu Lα peak five times more intense, indicating clearly the presence of parasite X-rays .

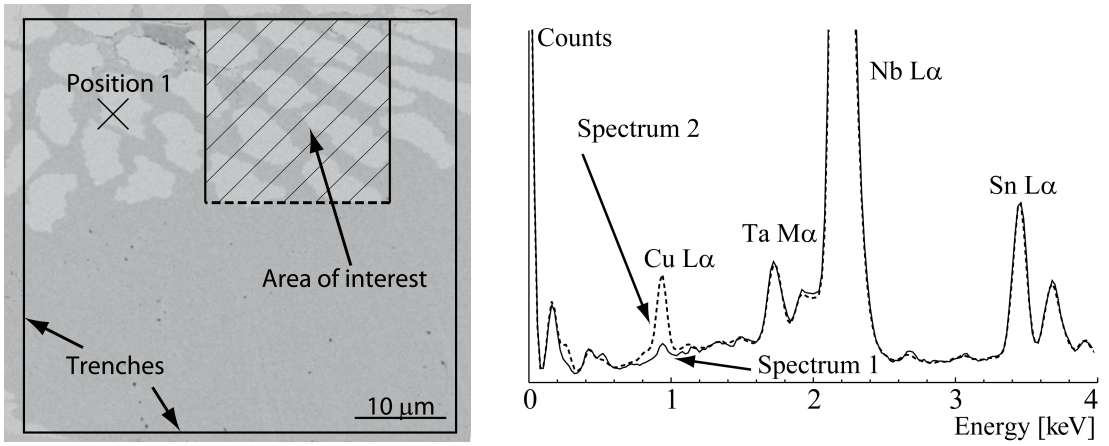

(a) Milling pattern drawn on a top-view BSE image of the sample. Nb_3Sn wires are in light gray. The dashed line indicates the position of the milled surface. The spectrum 1 of figure 4.1(b) is recorded at position 1.

(b) Measurements of parasite X-rays on Nb_3Sn strand. Spectrum 1 is free of this artifact, being recorded at position 1 with no tilt. Spectrum 2 is recorded on the milled surface, at position 2 of figure 4.2. The spectra are recorded at 20 kV. The no. of counts is adjusted to have the same height of Nb Lα peaks.

Figure 4.1: Parasite-X-rays measurement: milling geometry and measured spectra.

The sample prepared in U-pattern geometry is shown in the SEM image of figure 4.2. An EDS map of the milled surface is recorded at 7 kV. Copper content is calculated from it, scaled with a colour code, and superimposed to the SEM image. The map is displayed only at the position of the Nb_3Sn strands, the surrounding matrix being composed of 100% of Cu. The part on bottom left suffers from a detector shadowing effect. The copper content depends on the position on the milled surface: from left to right, it increases and, from top to bottom, it goes through a maximum at about the half height of the face. This experiment shows the qualitative distribution of parasite X-ray generation.

To test the influence of the trench geometry, the right trench was milled wider, obtaining a modified U-pattern geometry shown in figure 4.3(a). The two geometries were tested measuring

[1] Spectrum 1 is recorded with the geometry of a classical EDS analysis on a horizontal surface.

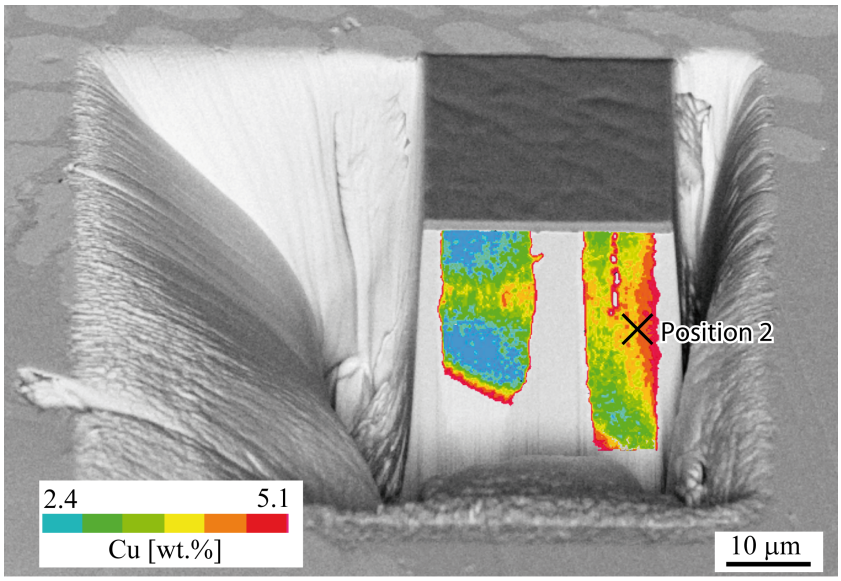

Figure 4.2: Cu-content map characterizing parasite-X-rays distribution. The map is superimposed to the BSE image of the sample, prepared as described in figure 4.1(a). EDS map and BSE image are recorded at 7 kV. The map is displayed at the position of Nb_3Sn strands. Spectrum 2 is recorded at position 2 (see figure 4.1(b)).

EDS spectra at 10 different positions on the Nb_3Sn strands. In figure 4.3(b), the resulting copper contents are plotted in function of the accelerating voltage. The central point indicates the mean value and the bars extend to the minimum and maximum. As the accelerating voltage increases, mean parasite X-rays increase regularly, and the extrema spread. The modified geometry shows a lower level of parasite X-rays .

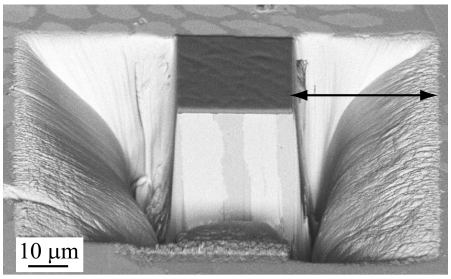

(a) SE image of modified U-pattern geometry. The trench on the right is wider.

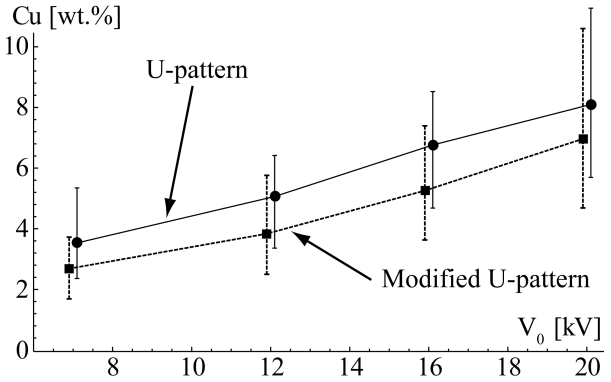

(b) Copper content plotted in function of accelerating voltage. The central point is the mean of 10 measurements at different positions on the Nb_3Sn strands. The measurements extrema gives the error bar.

Figure 4.3: Influence of accelerating voltage and of surrounding geometry.

4.3 Discussion

The parasite-X-rays yield depends on three factors: 1) the intensity of primary BSE and X-rays that hit the surrounding walls, 2) the probability of generating secondary X-rays (cross section), and 3) the absorption of these X-rays in the bulk. The second factor depends on the energy of the BSE and therefore on the accelerating voltage V_0. This explains the increase of their contribution with V_0, as observed in the plot of figure 4.3(b).

The first factor varies with the solid angle under which the surrounding walls are "seen". The intensity is inversely proportional to the square of the source-to-wall distance, the source being the beam position. As observed in figure 4.2, the wall on the right is closer than the others. This explains the higher values in the copper map from left to right, as well as the lower copper content for the modified U-pattern geometry (see figure 4.3(b)).

The dominant influence of the right wall is also increased by another circumstance. Figure 4.4(a) shows the sample from the point of view of the EDS detector. The right wall is almost facing the detector, but the other walls not; the take-off angle is higher, and the absorption of X-rays on the way to the detector is lower.

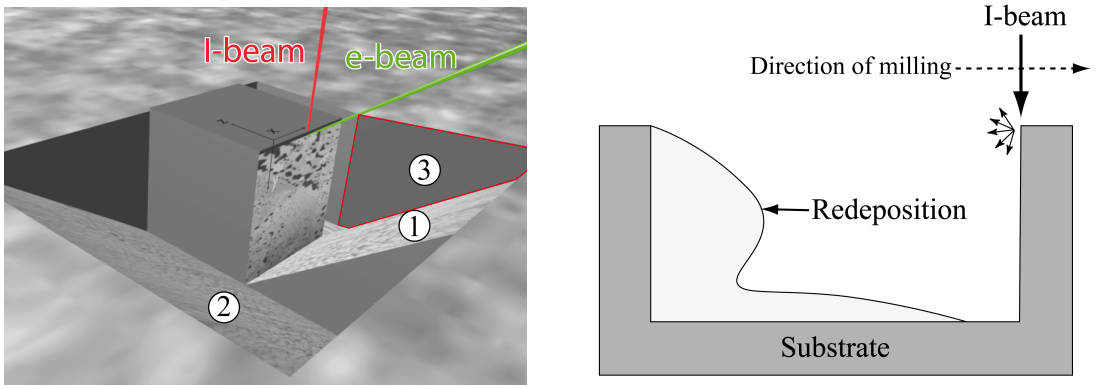

(a) Walls geometry from the EDS detector point of view.

(b) Wall shape resulting from redeposition during one-scan milling. (Adapted from Müller [56].)

Figure 4.4: Geometry and shape of the surrounding walls.

The influence of redeposition on wall shape was studied experimentally by Müller [56]. The trench was milled in one scan as all trenches of this work. The observed shape is drawn in figure 4.4(b). Without redeposition, the wall is almost vertical. As the ion beam removed material, the redeposition changes the wall shape. With a right wall of this shape, the source-to-wall distance changes from top to bottom, explaining the parasite X-rays distribution of figure 4.2 along y axis.

As a first approximation, surrounding wall has roughly the mean composition of the milled surface. In the case of totaly homogenous samples, the contribution of these parasite X-rays would not change the analysis, as they would add X-rays with similar intensities. This changes if we want

to analyse small features with a different composition than the matrix. The parasite X-rays linked to the matrix-phase composition will be added to the small-feature's measurements.

Redeposited material contains a certain amount of gallium coming from the ion of the beam; surrounding walls contains few wt.% of gallium. Parasite X-rays from gallium are observed. Measured in the same conditions than for copper content, the gallium content is always lower than 1 wt.%, close to detection limit of EDS.

In this study, a static case is considered. However, during 3D acquisition, the composition and the geometry of the surrounding walls change, and therefore the parasite X-rays. If the volume of interest has a constant mean composition, the variations are small. Müller has observed that a steady wall shape is reached as the milling goes on [56]. The surrounding wall keeps globally the same shape, but the distance between them and the milled surface grows larger.

5 Noise reduction

In FIB nanotomography, data acquisition can last up to several days. The main part of this time is spent acquiring SEM images or EDS maps, the milling time to remove material is considerably shorter (typically several hours). Compared to SEM imaging, EDS mapping takes longer even with large area SDD detectors. For a precise analysis[1], several millions of counts per spectrum would be needed: this corresponds to several tens seconds of acquisition time per pixel depending on the acquisition rate. As a matter of comparison, with a 3D acquisition that lasts 48 hours, the acquisition time per voxel (dwell time) is about 100 ms. This corresponds to several thousands of counts with a high acquisition rate; three orders of magnitude less counts than typically required for a precise analysis.

The low number of total counts per spectrum produces noisy data, and the compositional precision is low. To improve it, the quantification procedure is modified adding two noise-reduction steps: principal components analysis (PCA) as a noise-filter before the quantification and a median filter after quantification. The limitations of this procedure and its capability to reduce noise are investigated with well characterized sets of spectra. In the first section, these sets of spectra are defined and characterized. In the second section, the smoothing steps and the quantification procedure are described. In the last section, the evolution of noise at each step of the procedure is measured and discussed. The data acquired on the NiTi-SS sample are used in this chapter as the spectra of the 3D stack are especially noisy.

[1] $2\sigma < 1\%$ relative can be reached, see section 2.3.2

5.1 Measurement of the noise level

As discussed in section 2.3.2, the noise in microanalysis is due to variations in intensity induced by counting statistics, following thus Poisson statistics. The noise propagates through the quantification procedure to the final composition. Noise is a type of uncertainty, and its propagation can be calculated using mathematics of uncertainty propagation. To ensure the correctness of such a calculation, sets of measured spectra are used: noise in the set is characterized before the quantification and measured at the different steps of the procedure. For proper noise measurement, the variations in the sets need to be only due to counting statistics and not to sample heterogeneity or measurement variations.

5.1.1 Sets of spectra

The 3D stack and a 2D map of the NiTi-SS sample are acquired at the border between the weld and the unmelted NiTi wire. This wire is easy to identify on the EDS maps and is composed of a homogeneous NiTi phase, as it has not melted during the welding. Spectra from both acquisitions (2D and 3D) are selected in the unmelted NiTi wire, forming the two sets used to measure the noise level.

Table 5.1 gives the relevant properties of the two sets of spectra, as well as the ones of a reference spectrum acquired on the NiTi base wire.[2] Spectra have been acquired with dwell times of 0.03 s, 0.3 s, and 30 s for the 3D stack, the 2D map, and the reference spectrum respectively. All other acquisition conditions are identical (see section 3.2.2); the total number of counts per spectrum is proportional to the dwell time. Several thousands of spectra are selected for each set; all spectra from the 3D stacks are from the same map (the 41^{st} map of the stack).

Table 5.1: Properties of spectra acquired on NiTi-SS sample (3D stack and 2D map) and on NiTi base wire (reference spectrum). The numbers of spectra in the acquisition and in the set used to measure the noise level are given.

	Dwell time [s]	Counts/spectrum [kcts]	No. spectra	No. spectra in set
3D stack	0.03	1.1	540'000	3'300
2D map	0.3	11	12'300	1'800
Reference	30	1'100	1	1

The reference spectrum and a selected spectrum per set are shown in figure 5.1(a). To compare these spectra, the count rate per energy channel (the counts per channel divided by the dwell time) is given for the y axis. The level of noise can be estimated looking at the background: for the spectrum of the shortest dwell time, there are only few, or often even zero, counts per channel. Ni Lα and Ti Kα peaks are clearly defined in all spectra. For the noisiest spectrum, smaller peaks such as Ni Kα can hardly be distinguished from the noise of the background.

[2] This spectrum is used as a microanalysis standard for Ni and Ti. It was recorded with a tilt angle of 36°, but not in the U-pattern geometry.

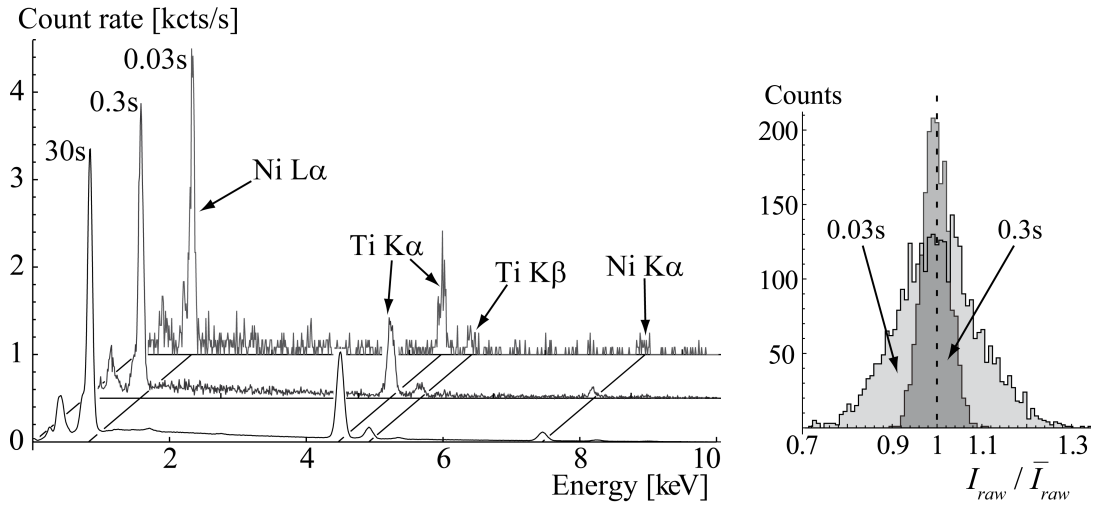

(a) Spectra acquired with different dwell times. The reference spectrum (30s) is the microanalysis standard for Ni and Ti and is recorded at 36° of tilt. The two spectra from 2D map and 3D stack (0.3 s and 0.03 s) are acquired in the U-pattern geometry.

(b) Histogram of raw intensity for the two sets of spectra. These sets are used to measure the noise level. The bin size of 0.85% is equivalent to 1 count (X-ray) for the 0.03 s distribution.

Figure 5.1: Spectra acquired on the unmelted NiTi wire at 10 kV.

5.1.2 Variations in the sets

If the variations in a data set are only due to counting statistics, data follow Poisson statistics. To test Poisson nature of the sets of spectra, the chosen variable is the raw intensity I_{raw} of the Ti Kα peak -the peak used to quantify Ti. I_{raw} is given by the number of counts between 4.45 keV and 4.47 keV; the channel width between these limits L_{int} is close to the full width at half maximum (FWHM) of the Ti peak (L_{int}=130 eV). The distributions of I_{raw} in the two sets are plotted as histograms in figure 5.1(b) and their characteristics are given in table 5.2.

To compare the two distributions in figure 5.1(b), I_{raw} relative to the mean value of I_{raw} in the set ($I_{raw}/\bar{I}_{raw}$) is given for the x axis. The bin size is set to be equivalent to 1 count (X-ray) for the 0.03 s distribution. The global shape resembles a normal distribution, confirming the Poisson nature of the noise.[3]

A Chi-squared test is applied on the two distributions with the hypothesis of a Poisson distribution.[4] The output of this test is the probability values (p-value): the closer is this value to 1, the more likely is the hypothesis. When p-value is higher than a cutoff usually set at 0.05, the hypothesis is considered true. Given in table 5.2, p-values of the distributions are higher than 0.05 and the one of the longest dwell time is close to one: both distributions follow a Poisson distribution. The two sets of spectra are thus measured under stable conditions and on a

[3]Poisson distribution with high number of measurements can be approximated by a normal distribution.

[4]The well-known Pearson's chi-squared test is used.

homogenous phase; variations are only due to counting statistics.

Table 5.2: Characteristics of the two distributions of figure 5.1(b) from the sets of spectra measured in NiTi phase. The used variable is the raw intensity I_{raw} of Ti Kα peak. n is the number of spectra. The sample standard deviation S is defined in equation 5.1.

Dwell time [s]	n	$\overline{I}_{raw}$	p-value	σ^2_{raw}	$2\sigma_{raw}/\overline{I}_{raw}$
0.03	3300	117.2	0.18	117.3	0.185
0.3	1800	1152	0.99	1156	0.059

Variations in the whole data (population) can be characterized by the standard deviation of a set (sample) selected from the data, as expressed in the textbook of Goldstein [4]:

$$S^2 = \sum_{i=1}^{n} \frac{(N_i - \overline{N})^2}{n-1}. \tag{5.1}$$

with i the index of a spectrum in the n spectra of the set and N any spectrum variable such as I_{raw}, k-ratio, or C. Given the high value of n, S is an appropriate measurement for σ, the standard deviation of the whole population, and σ is used to designate both S and σ. Calculated for the two distributions, σ^2_{raw} is given in table 5.2. As expected for a Poisson distribution[5], σ^2_{raw} is close to $\overline{I}_{raw}$. Equation 5.1 can be used to calculate $2\sigma/\overline{N}$, the relative standard deviation in the set of spectra, as a measurement of the noise level in any spectrum variable N.

5.2 Noise reduction procedure

Two noise reduction steps are added to the quantification procedure: the PCA as a spectral filter and the median filter as a spatial filter. In a first step, these filters are described applying them independently on the 3D stack of the NiTi-SS sample. Then, the quantification procedure with both steps is discussed as a whole.

5.2.1 PCA as a noise-filter

PCA has been reported as a noise-filter to improve quantification by Parish in the case of STEM-EDS[6] [39]. He has considered the quantification of phases with similar composition; these phases are formed by a complex system of elements that have sever peaks overlaps. He concluded that PCA as a noise-filter should be used with care. This method suffers of artefacts under certain conditions. In this subsection, this method is discussed in details, applied on the 3D stack acquired on the NiTi-SS sample.

[5] $\sigma^2 = \overline{I}$, see equation 2.6

[6] STEM stands for scanning transmission electron microscope. The difference between STEM-EDS and SEM-EDS is that the first deals with thin sample and the second deals with bulk sample: the k-ratio extraction is the same, but the quantification method is different (usually the Cliff-Lorimer's one for STEM-EDS [57]).

Applying the PCA on the whole data, the data matrix **D** is decomposed in scores (images) and in loadings (spectra), as described in section 2.4.3. Each set of score and loading (each component) is associated to an eigenvalue that characterises the amount of variance in the component. The components that describe the best the original data need to be selected in order to reconstruct a faithful approximation of the data leaving aside the noise.

One efficient way of selecting the components is achieved by visual inspection of scores, loadings, and eigenvalues, as illustrated in figures 5.2. In figure 5.2(a), the eigenvalues are plotted in function of the component index, forming the so-called screeplot. By construction, the components are sorted by decreasing eigenvalues (decreasing amount of variance). After the seventh component indicated by a vertical line, the curve reaches a plateau suggesting a limit above which the components describe only noise. To illustrate the selection method by visual inspection, two components are considered on each side of this limit: the fourth and the ninth. Their score (image) and their loading (spectrum) are shown in figure 5.2(b). Below the limit, the fourth component describes part of the data[7], whereas, above the limit, the ninth component mainly describes noise. By visually inspecting the score and the loading of the other components, the first seven are selected for the reconstruction.

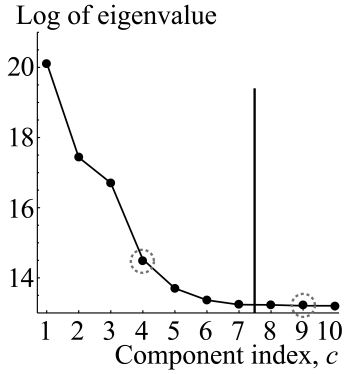

(a) Eigenvalue plotted in function of component index. Components have been selected up to the seventh one (vertical line).

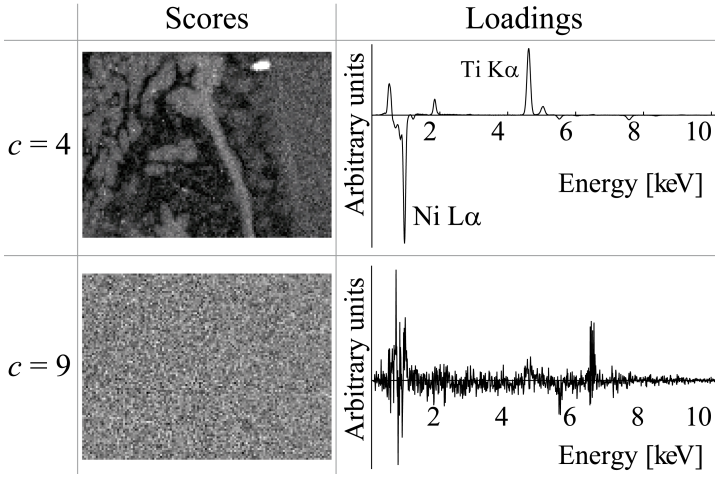

(b) Two selected components represented by a score (image) and a loading (spectrum). The 11^{th} image of the stack is displayed.

Figure 5.2: PCA as a noise-filter applied on the whole 3D stack acquired on the NiTi-SS sample: choice of the components that describe the best the data.

[7] *n.b.* the loadings (spectra) can have negative values as mentioned in section 2.4.3.

Figure 5.3(a) shows the two selected spectra (see figure 5.1(a)) and the corresponding spectra from the reconstructed stack. These last spectra are significantly less noisy than the initial spectra. Figure 5.3(b) shows the level of noise $2\sigma/\overline{N}$ measured with the raw intensity I_{raw} of the Ti Kα peak. The noise level is lower with PCA for the two sets by a factor of ~1.5. In figure 5.3(a), the continuous background is smoother for the reconstructed spectrum with the short dwell time than for the raw spectrum with the long dwell time. The opposite is observed for the noise level of the Ti Kα peak given in figure 5.3(b). This suggests that the noise of the background is more reduced by PCA than the noise of the peak.

Used as a noise-filter, PCA can be seen as a method that finds correlations in the data to build an improved spectral reconstruction. The different energy channels of an EDS spectrum are correlated when they are in the same peak, in peaks of the same element, or in peaks of correlated elements (*e.g.* same phase). These correlations can help for a more accurate spectral reconstruction. For example, the ratio between Ni Kα and Ni Lα is constant; this ratio is more accurate in the reconstructed spectrum, even if the Ni Kα peak in the initial data is hardly above the noise level of the background. However, correlations may induce errors in the reconstruction. The unmelted NiTi phase does not contain iron, and the noisiest spectrum does not seem to have a Fe Kα peak, but its reconstruction does. As iron is present in large amount in other part of the sample, correlations are established between the Fe Kα peak and to some other energy channels, probably the ones of the Fe Lα peak at low energy close to Ni Lα. As the noise level is high and the two peaks are close, these correlated channels may contain enough counts to generate in the reconstruction the Fe Kα peak. This spurious peak is not present in the spectrum with longer

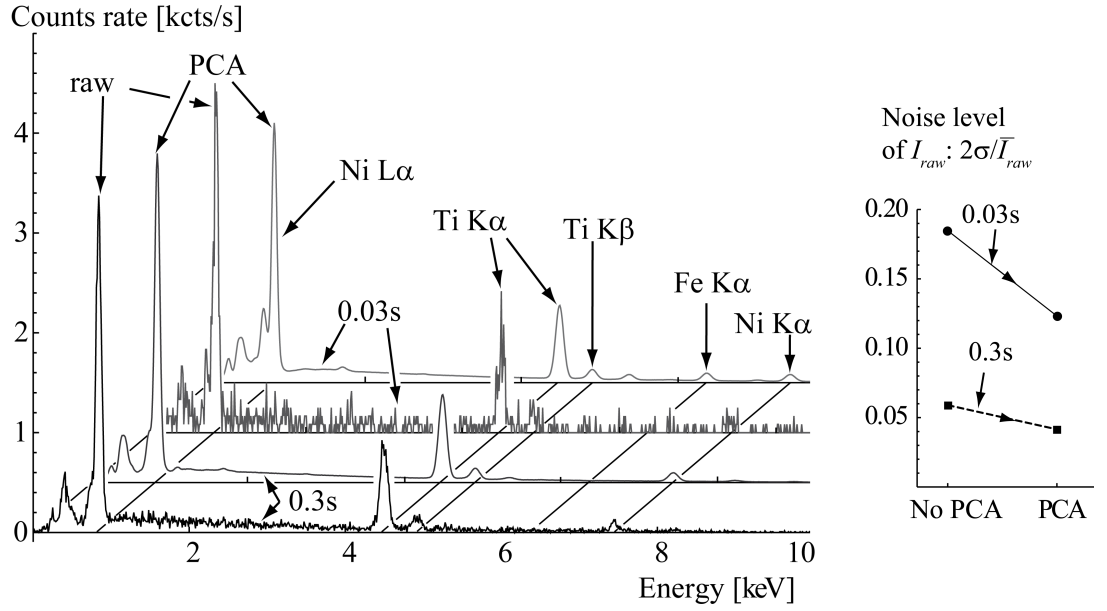

(a) Spectra from figure 5.1(a) and corresponding reconstructed spectra.

(b) Noise level measured for I_{raw} of the Ti Kα peak.

Figure 5.3: PCA effect on spectra measured on NiTi phases.

dwell times. A certain signal-to-noise level is needed to suppress it.

The artefacts described by Parish are similar [39]. His main conclusions regarding PCA as a noise-filter are corroborated by our example: the raw spectrum and the reconstructed one must be carefully examined, and the peaks chosen for the analyses should be clearly above the noise. PCA does not remove the requirement of a high enough signal-to-noise ratio for a reliable quantitative analysis.

5.2.2 Median filter

Median filter is a classical filter among the different spatial smoothing filters that preserve edges. More specific smoothing filters have shown better results on certain type of data[8] [33]. Median filter has been chosen because: A) it is local, B) its kernel size is constant and thus it has a well-defined effect, C) and it is easy to adapt for 3D EDS data.

A median filter smoothes noise preserving edges, but tends to remove small spherical features as described in section 2.4.2. In the NiTi-SS sample, small particles of titanium carbide (TiC) are observed in the SE images with a black contrast, as shown in figure 5.4(b). Each particle has the size of only a few EDS voxels. The median filter needs to be adapted in order to preserve these TiC particles.

One TiC particle is indicated by a red arrow on the SE image of figure 5.4(b) and on the Ti quantified maps of figure 5.4(a). In this last figure, 3D median filters with two different kernels are applied on the Ti quantified stack. The first kernel is formed by the 26 voxels sharing a face, an edge, or a corner with the central voxel: the cubic kernel. The second kernel is formed by the 6 voxels sharing a face with the central voxel: the cross kernel. As defined in the previous section, the noise level $2\sigma/\overline{C}$ is measured for the different filters with the Ti content and shown in figure 5.4(c). The noise is reduced by a factor of 3.7 with the first kernel, but the TiC particle disappears. The noise is reduced by a factor of 2 with the second kernel, and the TiC particle is hardly visible. In the last smoothed map at right in figure 5.4(a), the volume is resampled with the number of voxels doubled in each direction (2 x 2 x 2 times more voxels) the number of voxel is doubled in all direction: the value of the new voxels is obtained by a linear interpolation. Applying then a median filter with a cross kernel (first order), the noise is reduced by a factor of 1.6, and the TiC particle is almost unaffected. Used as a spatial filter, this approach is referred as the 3D median filter.

[8] Nonlinear total variation filter [58] and anisotropic diffusion filter [34] are two promising smoothing filters that preserve edges. They need to be further tested on 3D EDS data.

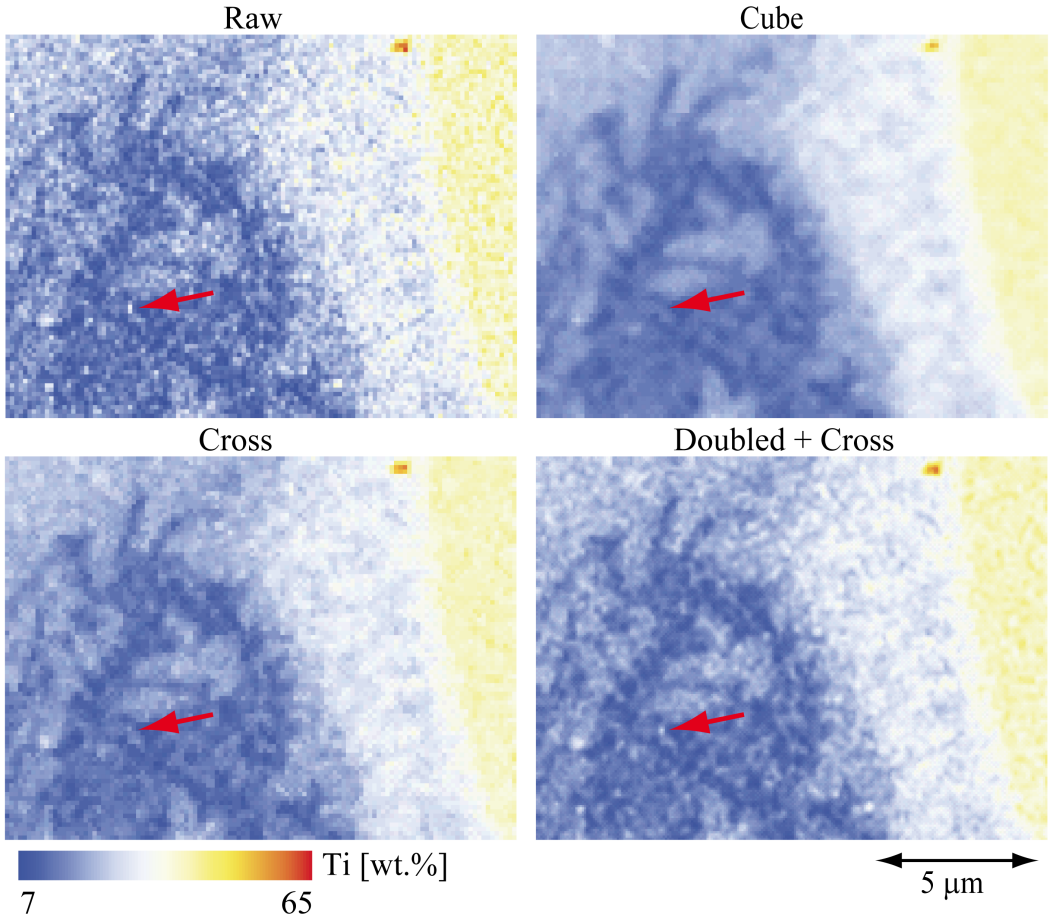

(a) Ti quantified map scaled by a colour code. The 11^{th} image of the stack is displayed. The red arrow indicates a TiC particle.

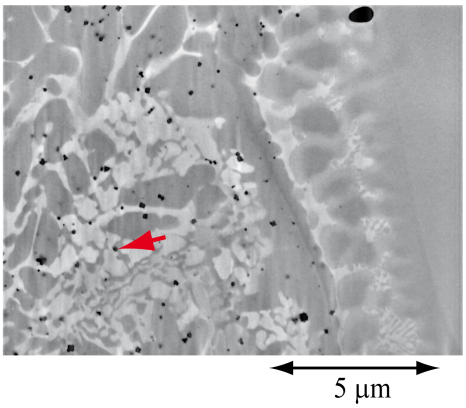

(b) SE image. The 11^{th} image of the stack is displayed. The red arrow indicates a TiC particle.

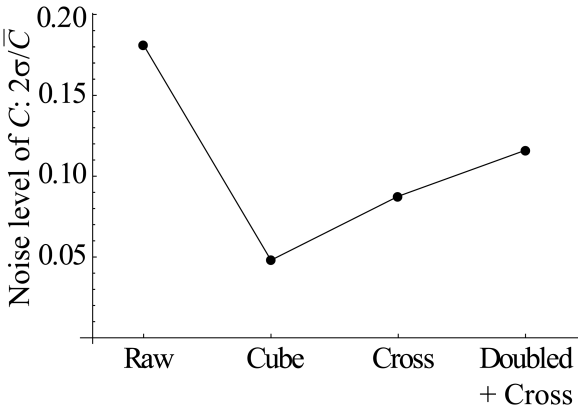

(c) Noise level measured with Ti content and plotted in function of the kernel used for the 3D median filter.

Figure 5.4: Choice of the kernel used for the 3D median filter considering a small spherical feature and the noise level. Median filters are applied on the quantified stack of NiTi-SS sample. "Cube" and "cross" indicate the shape of the kernel, and "doubled" indicates that the number of voxel is doubled in each direction.

5.2.3 The procedure as a whole

Figure 5.5 shows a flowchart of the procedure. First, the PCA is applied on the raw stack; the data matrix is then decomposed and the components are selected. The PCA reconstruction is a matrix multiplication, and each step in k-ratio extraction is linear: the order of these two operations can be inverted. In order to save computing time, k-ratios are extracted from the loadings and then multiplied with the scores to reconstruct a stack of k-ratios maps. The two steps of k-ratio extraction from the loadings are shown in figure 5.5: 1) background subtraction with the top hat filter to obtain I_{corr}, the corrected intensity, and 2) the division of I_{corr} by I_{std}, the intensity measured on a standard. Thanks to the limited number of selected components (seven in our case), a visual inspection of loadings and standard spectra is possible for an accurate k-ratio extraction. The k-ratio stack are then quantified with the $\phi(\rho z)$ method (see section 2.4.1), and each composition is normalised to 1. After registration of the stack, the 3D median filter is applied.

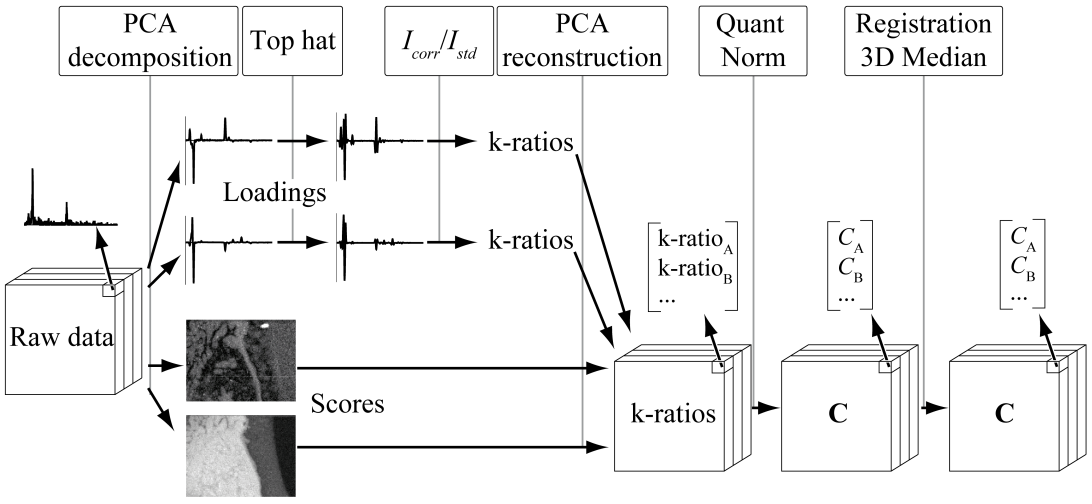

Figure 5.5: Flowchart of the smoothing quantification procedure from raw data to smoothed quantified stacks. I_{corr} is the intensity corrected from background, and I_{std} is the intensity measured on a standard (also corrected from background). "Quant" is the $\phi(\rho z)$ quantification and "Norm" is the normalisation of each composition to one. For each stack, the content of one voxel (top right corner) is illustrated.

5.3 Evolution of noise during quantification

The smoothing quantification procedure described before is applied on the 3D stack and the 2D map acquired on the NiTi-SS sample, and the resulting changes in noise level are discussed. In the first subsection, the output of procedures with or without the smoothing steps is qualitatively described. In a second subsection, the noise level quantitatively measured at each step of the procedure is discussed.

5.3.1 Qualitative results

Three different procedures are discussed: the procedure without any smoothing steps (Quant), the smoothing procedure without the last step of spatial smoothing (PCA + Quant), and the smoothing procedure as defined in figure 5.5 (PCA + Quant + 3D Median). Figure 5.6(a) shows orthogonal views of Ti content through the stack quantified with these three procedures. The ones with the two other elements are given in appendix B. The PCA filter smoothes clearly the noise and reveals features that were hidden in the noise. The 3D median filter further smoothes the noise, reduces slightly the intensity of the spherical TiC particles (in white), and enhances further the larger features.

In figure 5.6(b), the Fe-, Ni-, Ti-concentrations measured at each voxel of the quantified 3D stacks are reported in a ternary Gibbs simplex, with a logarithmic scale (from blue to red) [59]. These ternary histograms are overlaid on a 1000°C-isothermal section of the Fe-Ni-Ti phase diagram (see section 3.1.2). Without any smoothing, the peaks are broad due to the high level of noise, and the composition "path" goes almost directly from the NiTi phase (no iron) towards a pure iron phase. As smoothing steps are added, the peaks become narrower, and the compositions form a more winding path. It tends to go from one of the indicated phases to another as predicted by the theory.

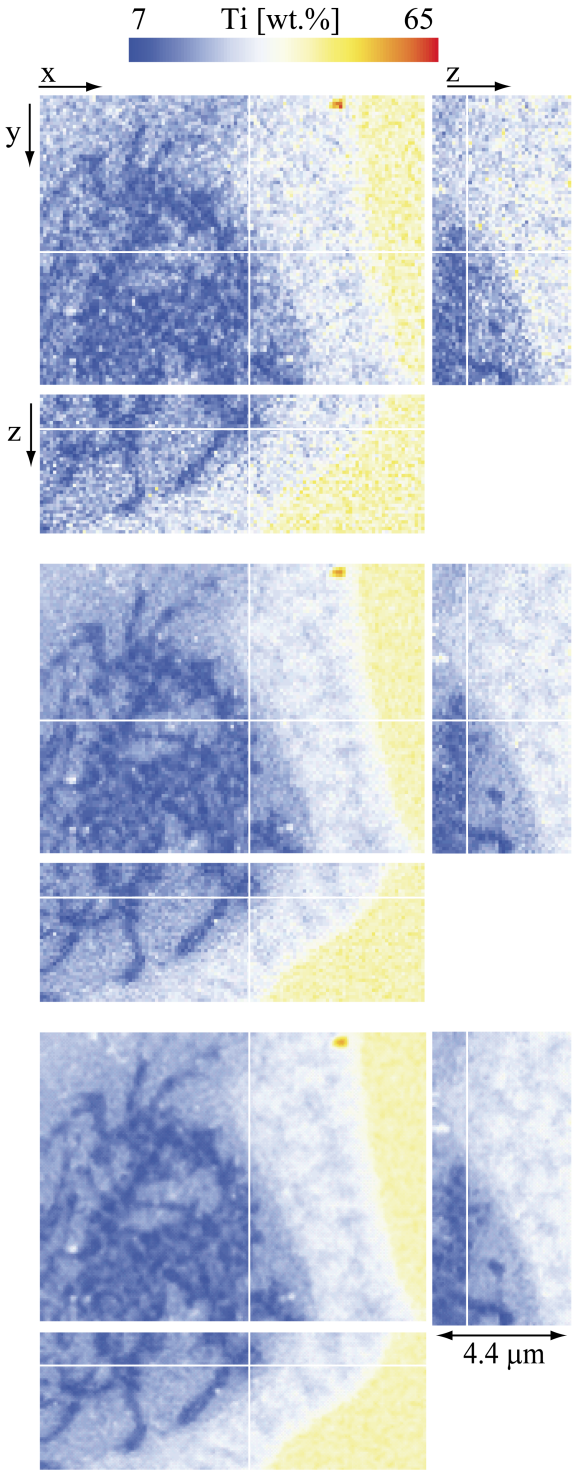

(a) Orthogonal views through Ti quantified stacks, scaled by a colours code. The white lines show the position of the other orthogonal views.

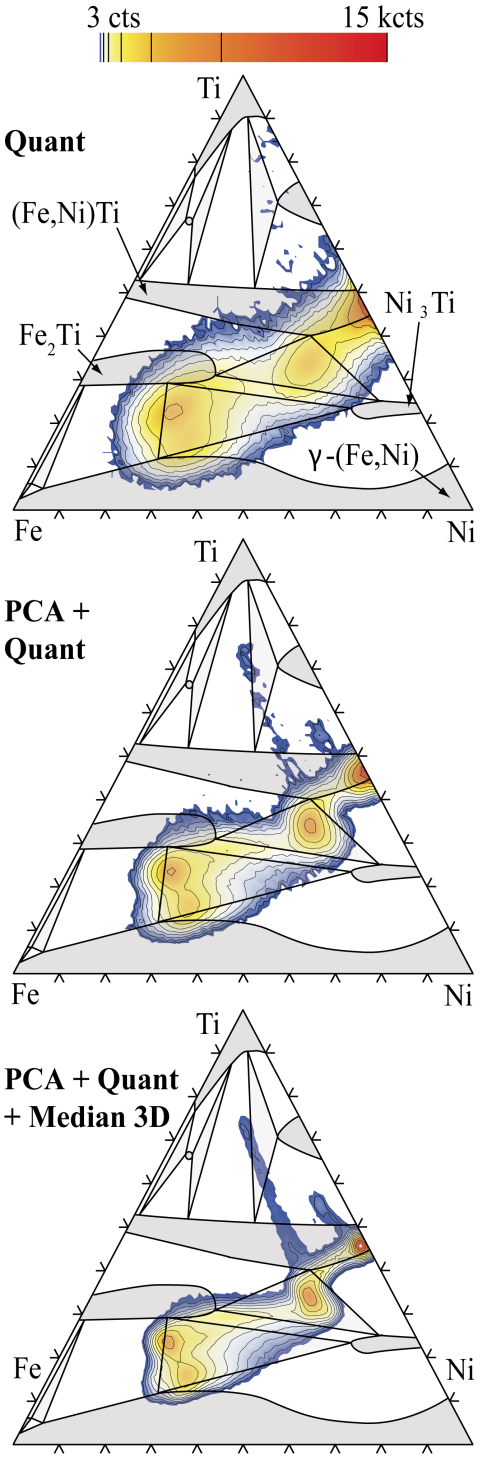

(b) Fe-Ni-Ti ternary histograms scaled by logarithmic colours code and iso-contours. A ternary phase diagram cut at 1000°C is superimposed [45].

Figure 5.6: Orthogonal views and ternary histograms of the NiTi-SS stacks quantified with three different procedures: procedure without smoothing (Quant), with spectral smoothing (Quant + PCA), with spectral and spatial smoothing (Quant + PCA + 3D Median).

5.3.2 Quantitative results

As defined in a previous section, the relative standard deviation $2\sigma/\overline{N}$ is used as a direct measure of the noise level. $2\sigma/\overline{N}$ is measured on two sets of spectra selected in the NiTi phase with Ti intensity, k-ratio, or Ti content as variables. Spectra from one set are acquired with a dwell time of 0.3 s (the 2D map) and spectra from the other set are acquired with a dwell time of 0.03 s (the 3D stack). Figure 5.7 shows $2\sigma/\overline{N}$ at each step of the procedure: absolute in (a) and relative to the first value ($2\sigma_{raw}/\overline{I}_{raw}$) in (b). In the following subsection, each main step is discussed comparing the two sets (different dwell times) and the procedure with or without the PCA filter.

The standard deviation σ quantifies the uncertainty of a variable. The mathematics of uncertainty propagation gives the following relations for addition and division:

$$N_3 = N_1 \pm N_2 \quad \rightarrow \quad \sigma^2_{N_3} = \sigma^2_{N_1} + \sigma^2_{N_2} \pm 2\,\mathrm{Cov}_{N_1,N_2} \qquad \text{and} \tag{5.2}$$

$$N_3 = \frac{N_1}{N_2} \quad \rightarrow \quad \frac{\sigma^2_{N_3}}{N_3^2} \cong \frac{\sigma^2_{N_1}}{N_1^2} + \frac{\sigma^2_{N_2}}{N_2^2} - 2\frac{\sigma_{N_1}\sigma_{N_2}}{N_1 N_2}\,\mathrm{Corr}_{N_1,N_2}, \tag{5.3}$$

where N_1, N_2 are real variables, N_3 is the calculated variable, and Cov_{N_1,N_2},Corr_{N_1,N_2} are the covariance and the correlation between N_1 and N_2. In the present case, variables N_1, N_2, and N_3 are the mean Ti intensities, k-ratios, or Ti contents from a set of spectra (*e.g.* $\overline{I}_{raw}$). Covariance and correlation are calculated between vectors of variables; one vector is composed of all values of a variable. Covariance and correlation are equal to zero for independent variables.

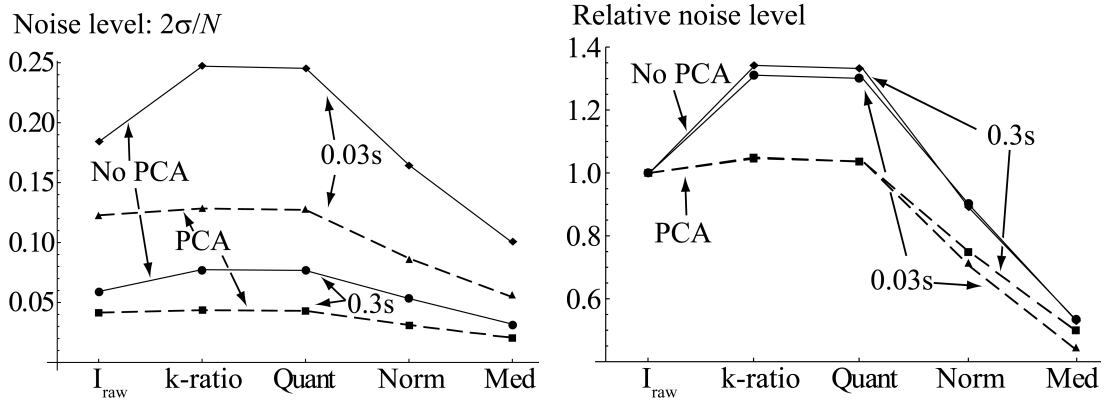

(a) Noise level $2\sigma/\overline{N}$.

(b) Noise level relative to the first value ($2\sigma_{raw}/\overline{I}_{raw}$).

Figure 5.7: Noise level measured on sets of spectra selected in the NiTi phase: measurements at the different steps of the procedure (see figure 5.5). $2\sigma/\overline{N}$ is calculated with Ti raw intensity I_{raw}, Ti k-ratio and Ti contents (raw, normalised, and smoothed with 3D median filter). The two sets of different dwell time (0.03 s and 0.3 s) treated with or without PCA are considered.

k-ratio extraction

The k-ratio extraction can be decomposed into three steps: the background subtraction, the intensity measurement, and the division by the intensity measured on a standard (I_{std}). The increase of noise $2\sigma/\overline{N}$ due to this last division can be calculated with equation 5.3 estimating that $I_{std} \cong \sigma^2_{std}$. As the two intensities are independent (Cov = 0), the relative variance σ^2 are added. In the present case, the increase of noise level varies from 1.0005 (0.03 s and without PCA) to 1.01 (0.3 s and with PCA). These values do not explain the significant change from I_{raw} to k-ratio observed in figure 5.7 without PCA. The two first steps of the k-ratio extraction need to be investigated. The background is removed by top hat filtering, and the corrected intensity I_{corr} is obtained with the total of counts between two limits, as already defined for I_{raw}[9].

Before considering the top hat filter, a simpler method to subtract background is considered: $I_{corr} = I_{raw} - I_B$, with I_B the intensity of the background. I_B and σ_B are measured on the left side of the Ti peak with the channel width L_{int}, as used to measure I_{raw}. σ_{corr} can be calculated with equation 5.2: σ_B is added to σ_{raw}. With this method, the increase of noise level is ∼1.1, compared to ∼1.35 for the top hat filter (without PCA, both dwell times). The loss of precision is smaller, but this method is usually not used in EDS quantification; the measure of I_B is often complicated by close peaks or irregular background. Top hat filter has proved to be more robust in difficult cases [30].

Figure 5.8(a) shows a closer look on the Ti Kα peak of the selected spectrum acquired with a dwell time of 0.03 s (see figure 5.1(a) and 5.3(a)). A top hat filter is applied to this spectrum and to the corresponding spectrum filtered with PCA. The kernel of the top hat filter is defined in the right inset of figure 5.8(a). This kernel has the optimal size suggested by Statham [51]: the positive central lobe has a size L_{up} close to FWHM of the Ti peak with L_{up}=130 eV.[10] The sum of the two negative side lobs ($2L_{low}$) is just smaller with $2L_{low}$ =120 eV. The peaks filtered with the top hat have roughly the same shape with negative parts on the sides. Compared to the unfiltered peak, the positive area is systematically smaller by a factor of about 2.3. In the case of PCA filtering, the background is efficiently removed. For the raw spectra, the peak is smoothed, but the background shows a type of oscillation.

[9] For further reading about precision of the top hat filter, refer to Statham [51]; among other problems, he has considered peak overlap using k-ratios extraction by least-squares fitting.

[10] The channel width L_{int} used to measure intensity has the same definition: close to FWHM of the peak. Thus $L_{int} = L_{up}$ = 130 eV for Ti Kα peak.

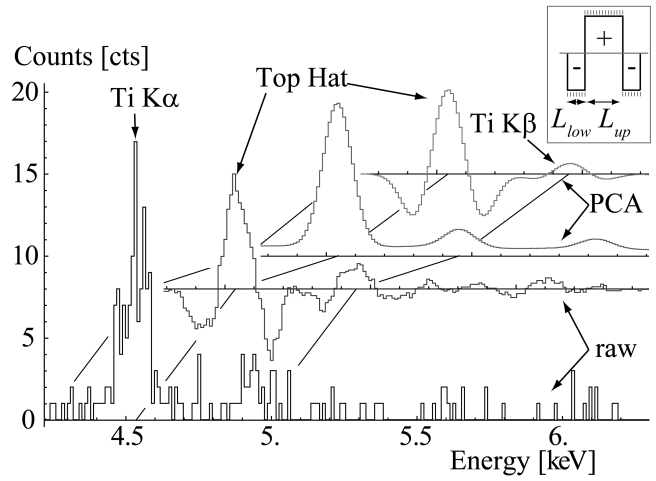

(a) Close look on the Ti Kα peak. The top right inset shows the kernel of the top hat filter.

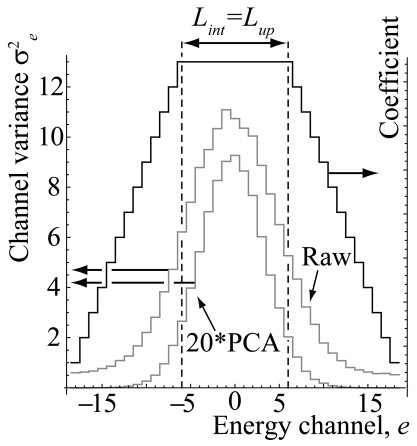

(b) Calculation of σ^2_{corr}: the coefficient (arbitrary units) are applied the variance per channel σ^2_e. All σ^2_e of PCA are multiplied by 20.

Figure 5.8: Top hat filter and PCA filtering applied on a selected spectrum acquired with a dwell time of 0.03 s). The raw spectrum and the one reconstructed after PCA are the ones shown in figure 5.3(a).

Top hat filter and intensity measurement are two linear operations (addition and subtraction) applied on the intensities I_e per energy channel (no. of X-rays per channel). Applying two times equation 5.2, σ^2_{corr} is obtained by a summation of channel variances σ^2_e and covariances between channels Cov_{I_e,I_e}. The coefficient to apply on the different σ^2_e are plotted in function of the channel e in figure 5.8(b). In this figure, the channel variances σ^2_e are also plotted for the spectra set corresponding to figure 5.8(a).[11] The two vertical dashed lines give the limits of intensity measurement L_{int} and the size of the central lob L_{up}. Between these two lines, the coefficients form a plateau and decrease outside them. The top hat filter adds thus to I_{corr} noise coming from channels on the sides of the peak.

As can be seen in figure 5.7(b), the increase of noise level due to the top hat filter is independent of the dwell time. Recording the spectra n times longer, all $\overline{I}_e$ are increased by n. Since all implied operations are additions or subtraction and PCA filter is a linear operator (matrix multiplication), n is reported to all σ^2_e, I_{raw}, I_{corr}, etc. and cancelled dividing $\sigma_{corr}/\overline{I}_{corr}$ by $\sigma_{raw}/\overline{I}_{raw}$.

As observed in figure 5.7(b), PCA filtering has a positive effect on the increase of noise level: without PCA the increase is about 1.35 and with PCA the increase is only about 1.05. This difference can be explained by the σ^2_e curves of figure 5.8(b). The curve with PCA goes quickly to zero outside L_{int}; σ^2_{corr} of PCA is almost only due to noise inside L_{int} unlike σ^2_{corr} without PCA. In other words, the noise from side channels added by the top hat filter is smaller with PCA

[11] The curve of σ^2_e for the set of raw spectra gives the average spectrum of the set, as $\sigma^2_e = \overline{I}_e$. This is not true for spectra filtered by PCA as they do not follow Poisson statistic anymore.

filter, as PCA strongly smoothes the background.

Quantification

The uncertainty propagation from k-ratio to composition due to quantification can be obtained with the following equation, adapted from Lifshin [25]:

$$\frac{\sigma_C^2}{C^2} = \frac{\sigma_{k-ratio}^2}{k-ratio^2}(1-\frac{(a-1)C^2}{a}) \qquad \text{with} \qquad \frac{1\text{ - }k-ratio}{k-ratio} = a\frac{1-C}{C} \tag{5.4}$$

where a is a constant unique for the set of elements and the accelerating voltage V_0. In the NiTi phase, the actual composition is the one of the standard sample (NiTi base wire): $k-ratio = C$ and a should be equalled to one. This is observed experimentally in figure 5.7.

After quantification, the contents of Ni and Ti are normalised to one. This operation reduces the noise level as observed in figure 5.7. The noise level propagation can be calculated using equations 5.2 and 5.3. Supposing that the content of the different elements are not correlated, the following relation is obtained:

$$\widehat{C_A} = \frac{C_A}{\sum_i C_i} \quad \rightarrow \quad \frac{\widehat{\sigma_A^2}}{\widehat{C_A^2}} \cong \frac{\sum_i \sigma_i^2}{(\sum_i C_i)^2} + \frac{\sigma_A^2}{C_A^2}\frac{\sum_i C_i - 2*C_A}{\sum_i C_i} \tag{5.5}$$

with $\widehat{C_A}$ the normalised content of element A. The supposition of no-correlation introduces ~10% of error compared to σ measured in the set of spectra. In the NiTi phase, $C_{\mathrm{Ti}} \cong C_{\mathrm{Ni}}$ and the second term is small; the decrease of noise level is about $\sim \sqrt{2}$ for all cases.

Spatial smoothing

The set of spectra acquired with the longest dwell time is extracted from a 2D map. To compare the noise level in the two sets spatially smoothed, the 3D median filter is adapted in an equivalent 2D median filter: the number of pixels is doubled in each direction and the kernel of the 2D median filter is set with the same number of pixels. As already observed in the previous section, the impact of the median filter on the noise level is mainly linked to the number of pixels in the kernel. In figure 5.7(b), a decrease of noise level of about 1.6 is observed for the four measurements.

5.4 Summary

In this chapter, a smoothing quantification procedure adapted for the noisy spectra of a 3D acquisition was studied, more specifically its limitations and its capability to reduce noise.

The limitations were discussed for the two noise-reduction steps of the procedure: 3D median filter and principal component analysis (PCA). Median filter is a well-known smoothing technique; to use it efficiently a balance between the smoothing effect and the removal of small spherical features has to be found with the appropriate number of voxels in the kernel. In the present case, the volume was resampled with a higher number of voxels to preserve the spherical features. The PCA as a noise-filter to improve quantification is a non-standard technique that can introduce artefacts if the considered peaks have a signal-to-noise ratio not high enough. It should be used with care visually inspecting the reconstructed spectra.

The capability to reduce noise was discussed considering the evolution of noise at each step of the procedure. The noise level was obtained measuring the variations in sets of spectra acquired in the same phase. The relative evolution of noise shows to be generally independent of the acquisition time per spectrum. With spectra recorded n times longer, the noise level is lower by a factor of about $\sqrt{n}$ at each step of the procedure, coherent with Poisson distribution. Median filter shows a constant effect on the noise level for a given number of voxels in the kernel. PCA reduces the noise in the spectra and has a strong positive effect on one step of the quantification procedure. The noise increase due to the background removal is strongly reduced by PCA, as PCA strongly smoothes the background.

6 Quantification enhancement

The interaction volume is one of the most important limiting factor of EDS mapping for spatial resolution and accuracy of quantification, as detailed in the first part of this chapter. When the variation in composition of the analysed microstructure has a size similar to this microvolume, it is heterogeneous for a large number of voxels; bulk quantification is not appropriate. If voxel size is smaller, interaction volumes of two adjacent voxels overlaps. The redundant information is used to improve existing quantification procedure; the developed method is called enhanced quantification. Based on simplified-geometry assumption, a first approach is presented as a "proof of concept". The method is then extended and applied to acquired data.

6.1 Interaction-volume impact

In the first step to understand the impact of the interaction volume on quantitative mapping, the X-ray distributions in homogeneous microvolumes compared to voxel size are examined. Then heterogeneous microvolumes are investigated. For this study, the electron beam is first considered normal to the surface. Tilt effects are treated in a later section.

6.1.1 Homogeneous microvolume

Figure 6.1(a) and 6.1(b) show X-ray depth distributions for the main elements of the studied samples. Each X-ray line is simulated in corresponding pure material. X-ray distributions in x and y are projected on z axis. Curves are corrected for absorption, and the area under the curves is normalized. The voxel sizes were chosen in order to have X-rays emitted from several voxels, as indicated by vertical lines. The maximum depth is 7 voxels for the AlZn sample and 4 voxels for the NiTi-SS sample. All distributions have a similar shape and vary in depth with one over the density, as suggested by Anderson and Hasler's relation for X-rays range R_x (see equation 2.2). For example, the density of Al is two times smaller than the density of Zn, therefore the depth distribution is less than half.[1]

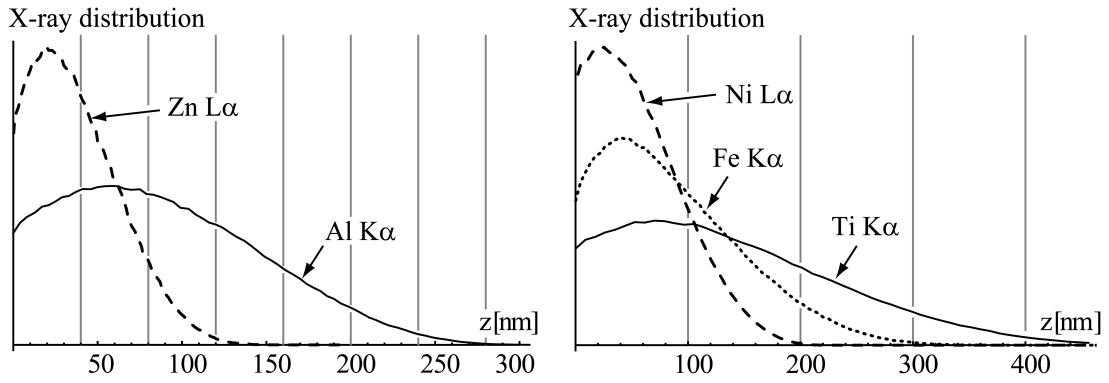

(a) Depth distributions for Al and Zn at 5 kV.

(b) Depth distributions for Ti, Fe, and Ni at 10 kV.

Figure 6.1: X-ray depth distributions in the corresponding pure material: Al Kα in Al, Zn Lα in Zn, etc. Area under the curves is normalized. Vertical lines show the voxel size of the study-case samples.

[1] ρ = 2.7 g/cm^3 for Al and ρ = 7.1 g/cm^3 for Zn.

At perpendicular incidence, the X-ray distribution has cylindrical symmetry, it can thus be fully represented with a 2D plot. In figure 6.2, depth and lateral X-ray distributions are plotted for aluminium and zinc. Distributions are retrieved counting emitted X-rays per bin. The two different scales represent two different bin sizes: the logarithmic colour code for bin size of 40 x 40 x 40 nm^3 and the height for bin size of 5 x 40 x 5 nm^3. The first corresponds to voxel size and the second gives a finer representation. Distributions are plotted in function of z and x, considering along y a single wall of bins.

Both distributions show a sharp peak under the beam entrance point; the voxel under the beam, the central voxel emits more X-rays than the others. The width is smaller; X-rays are more spread in depth than laterally. As electrons penetrate more in lighter material, the central voxel of Al emits less X-rays than the one of Zn, and lateral spreading is also more pronounced, especially for deeper voxels.

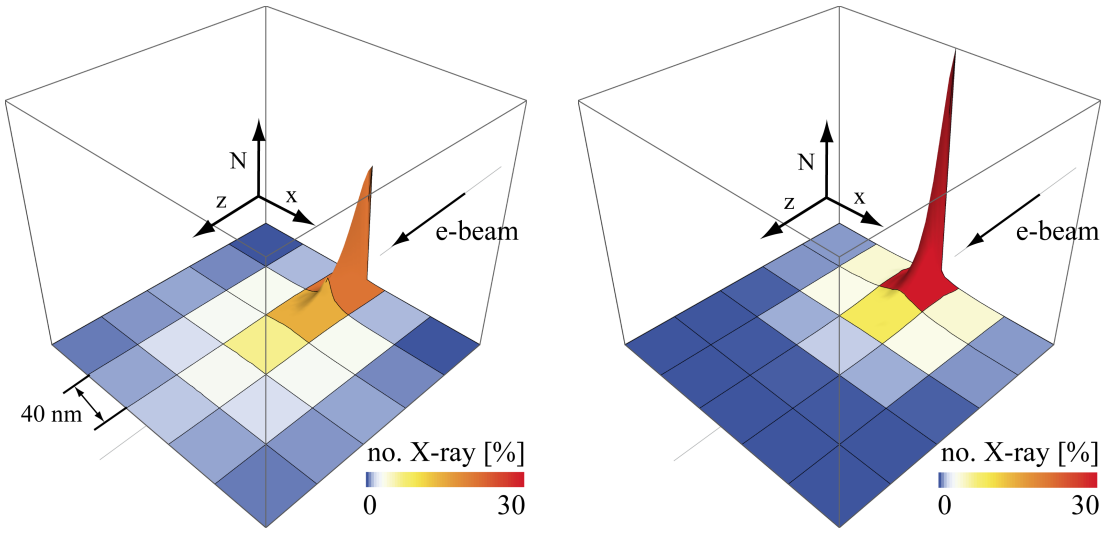

(a) Distribution for Al Kα in Al at 5 kV.

(b) Distribution for Zn Lα in Zn at 5 kV.

Figure 6.2: Lateral and depth X-ray distributions obtained with two bin sizes. N scales bin size of 5 x 40 x 5 nm^3 and the logarithmic colours code scales bin size of 40 x 40 x 40 nm^3.

6.1.2 Heterogeneous microvolume

To understand 3D mappings, a simplified geometry is considered, as described in figure 6.3(a). The interface between Al and Zn is parallel to the milled surface. Electron trajectories are displayed for the central voxel that is drawn by a dashed line. In the shown situation, numerous electrons cross the aluminium and penetrate into the zinc. The obtained microvolume is inhomogeneous; an important number of zinc X-rays are detected, even if the voxel is totally in the aluminium phase. In the next step, a layer is milled away with the ion beam creating a new surface. The new voxel is closer to the interface and more zinc X-rays are detected. Repeating milling and measurement steps, a profile along z is obtained, illustrated by the voxel line in figure 6.3(a)[2].

Such profile is simulated through two planar interfaces. In figure 6.3(b), the obtained k-ratios are plotted as a function of z. For both interfaces, a shift opposite to the incident electron direction is observed. The shift is different from one interface to the other as the interaction volume varies depending on if the electrons have to go through a denser or a less dense material first. The range of the influence of the "substrate" (deeper material) is directly related to the depth distribution of figure 6.1(a), and the maximum influence is proportional to R_x (see equation 2.2)[3].

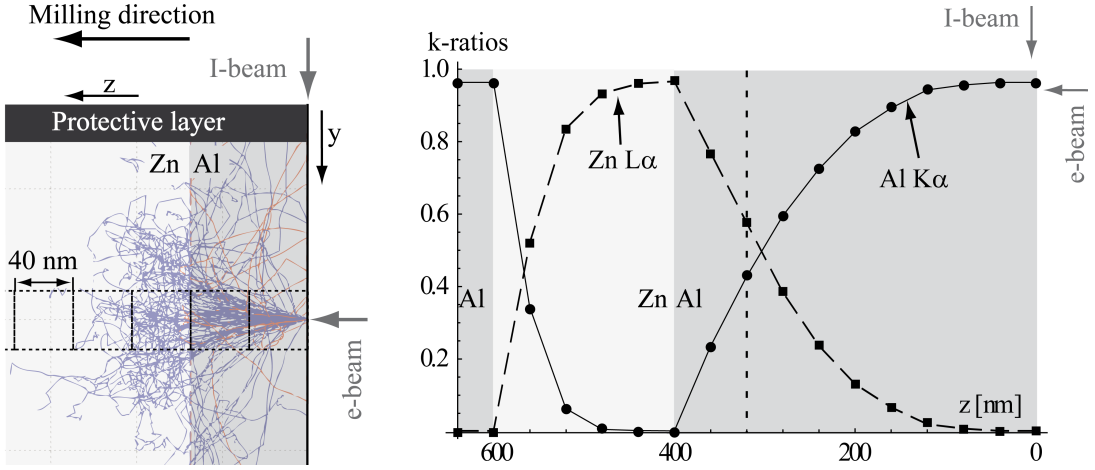

(a) Simulation geometry for one voxel of the profile (z = 320 nm in figure 6.3(b)). The voxels are drawn with a dashed line. Electron trajectories are displayed for one voxel.

(b) K-ratios of Al Kα and of Zn Lα plotted in function of z. The vertical dashed line indicates the position of the milled surface in figure 6.3(a).

Figure 6.3: Simulated profile along z. Between aluminium and zinc, interfaces are perpendicular to z axis. The electron beam is perpendicular to the milled surface, and the accelerating voltage is 5 kV.

[2] *n.b.* simulation geometry differs from U-pattern in electron beam that is perpendicular to the milled surface.

[3] R_x = 310 nm for Al Kα in Al and R_x = 125 nm for Zn Lα in Zn.

To calculate the composition inside each voxel, the k-ratios need to be corrected from effects similar to the matrix effects of bulk quantification. In the homogeneous case, matrix effects are described by the correction factors Z, A and F; in heterogeneous case, matrix effects are described by the correction factors Z', A', and F'. These factors are illustrated in figure 6.4 with the analysis of a precipitate surrounded by a matrix. Z' corrects from the different X-ray distributions, deformed in a complex way from one material to the other. A' corrects for absorption along the path that goes differently through materials to the surface towards the detector. F' corrects for all types of X-ray fluorescence, for instance the fluorescence of one material due to X-rays of another materials.

Z', A', and F' cannot be directly calculated since the microstructure and local composition of real sample is unknown, as for instance the case of figure 6.4. However, with the progress of the analysis in z of figure 6.3, the information of the neighbouring voxels is revealed. Z', A', and F' can be thus indirectly derived. Thus the quantification can be adapted to heterogeneous microvolumes forming the so-called "enhanced quantification".

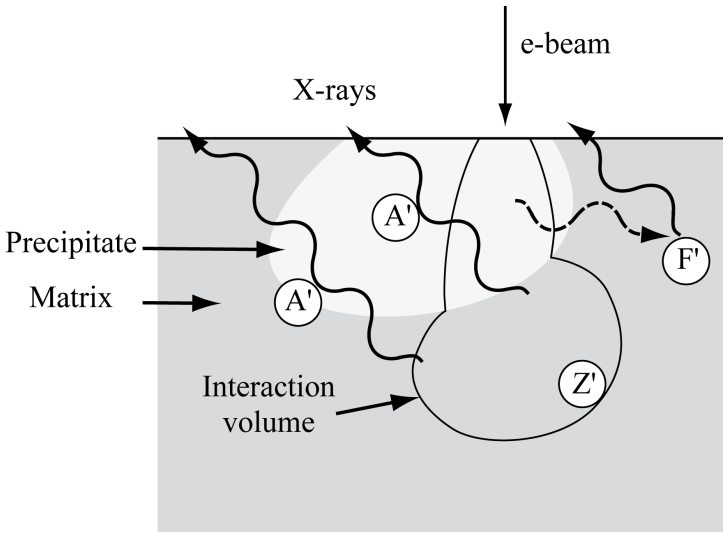

Figure 6.4: Matrix effects in the case of heterogeneous microvolume. Z' corrects from X-ray distributions, A' corrects from absorption along the path to the surface and F' corrects from fluorescence.

6.2 First approach

The "enhanced quantification" requires spectra recorded at various positions and depths that can only be reached with 3D EDS microanalysis. Since this technique is quite recent, such "enhanced quantification" has not yet been reported. However, there is an analogy with another type of complex EDS quantification. Recording spectra at the same position with different accelerating voltages, the information from a range of different depths (even if limited) is obtained. In the case of layered sample, this depth information is used to improve the quantification: this thin-film quantification has been described in section 2.4.1 [32]. The technique is based on the calculation of realistic $\phi(\rho z)$ curves of the layered sample; the Z', A', and F' correction factors are then derived from these curves.

As observed, X-ray distributions are more spread in depth than laterally. Therefore, an important part of X-rays are emitted from the column of voxels just under the electron beam. For instance, in the case of Al and Zn, 32 % and 40 % of X-rays are emitted from this column respectively (see figure 6.2). In a first approach, it seems reasonable to consider only these voxels. This assumption is valid for the electron beam with normal incidence and thus strictly speaking not for FIB/SEM data. Nonetheless, it is used as a first step to implement the enhanced-quantification method and to prove the reliability and the prospective of the method.

6.2.1 Implementation

An indexing system for the z axis is introduced in figure 6.5. j is the index of the central voxel, and n index indicate a voxel relatively to j.

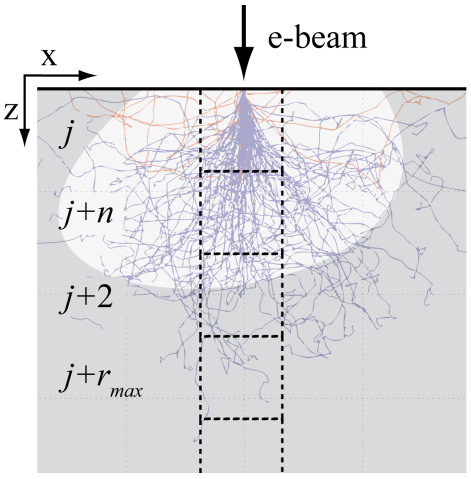

Figure 6.5: Definition of an indexing system for the z axis with indexes j, n, and r_{max}. The index j corresponds to the central voxel. n corresponds to the nth voxel under it. r_{max} corresponds to the deepest voxel from which X-rays are emitted.

With the first-approach assumption, the composition of the central voxel j depends on the measured intensities (the k-ratios) and on the compositions of the voxels under it. This is expressed as followed:

$$\mathbf{C}_j = f(\text{k-ratios}_j, \mathbf{C}_{j+1}, \mathbf{C}_{j+2}, ..., \mathbf{C}_{j+n}, ..., \mathbf{C}_{j+r_{max}}), \tag{6.1}$$

where f is a function and r_{max} is the deepest voxel from which X-rays are emitted as defined in figure 6.5. After initialization, this equation can be run recursively through the data. This equation is the recursive relation, f is the recurrence relation, and the global recursion forms the enhanced-quantification method.

Thin-film quantification as f function

Considering only voxels under the beam is equivalent to consider the sample as stratified; each voxel corresponds to a layer. Consequently, the thin-film quantification is a candidate for the recurrence function. Using this technique as function f, the composition of the central voxel is calculated taking into account the influence of voxels underneath. k-ratios$_j$ are corrected for Z', A', and F' factors that are approximated by a thin-film geometry.

In thin-film quantification, the layer system is first defined with all a-priori knowledge: with known parameters and guesses for the unknown. Accuracy of the quantification procedure depends on the specificity of the layer system. The case defined by equation 6.1 is specific, and some aspect of the expected accuracy are discussed based on Pouchou's consideration [60]. On the negative side, the layers can often have common elements, and k-ratios are measured at only one accelerating voltage. This is an unfavourable case for the thin-film quantification; the risk of converging at a local minimum is increased with such systems. On the positive side, the value to determine is the composition of the uppermost voxel:

- Because compositions are normalized layer by layer in thin-film iteration, error on composition is lower than error on thickness.
- Because the upper layer is considered, $\phi(\rho z)$ curves and absorption are less influenced by other deeper layers. Less correction with possible inaccuracies is needed.
- Because the layer system is relatively fixed, in case of convergence to local solution, the results is more inaccurate than dramatically wrong.

For a more robust recursion, the layer system is set at each step in a way to avoid the most unfavourable case. When in homogeneous phase, k-ratios of voxels are similar and bulk quantification is used. Defining the layer system, layers with close compositions are grouped together.

Recursion implementation

Implementation details are shown in figure 6.6. The main loop on voxel along j goes backwards, towards smaller values of j. Bulk quantification is used to initialize the recursion at highest value of j. In the loop, if the k-ratios of voxels j and j+1 are close enough ($\sum^{A} |\text{k-ratio}_{A,j} - \text{k-ratio}_{A,j+1}| < \epsilon_c$), the microvolume under the voxel is considered as homogeneous, and bulk quantification is used.

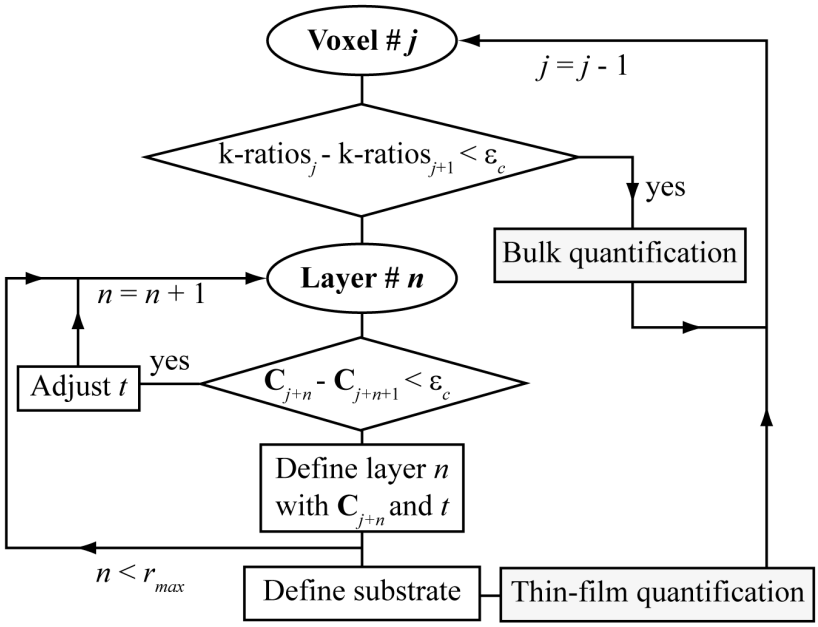

Figure 6.6: Implementation of the first approach: flowchart of the recursion. Ovals indicate loops, rectangles indicate actions, and rhombuses indicate tests.

The layer system is then defined. The k-ratios are set as guesses for the unknown composition of the upper layer. The layers underneath are defined in a loop along n. If compositions of voxels j+n and j+n+1 are close enough ($\sum^{A} |C_{A,j+n} - C_{A,j+n+1}| < \epsilon_c$), they are grouped in one layer and thickness t is adapted. If not, the layer n is defined with a composition $\mathbf{C}_{j+n}$ and a thickness t corresponding to the voxel size in depth. The loop on n ends when r_{max} is reached; the substrate is defined with $\mathbf{C}_{j+r_{max}}$ and the quantification procedure is applied on the layer system[4]. The algorithm for the enhanced quantification is hence implemented.

[4] r_{max} is given by the maximum among all R_x in pure material and reported to the voxel size. ϵ_c is set typically to 1 wt.% times the number of elements.

6.2.2 Test on profile along z

The geometry of the profile along z is defined in figure 6.3(b). The sample considered in this figure is formed by two materials with a planar interface in between. This is a thin-film system, and the assumption of the first approach is valid (see section 6.2). The enhanced quantification is tested on such profiles first with pure materials and later with compound materials.

Pure materials

The profile of figure 6.3(b) goes through pure aluminium and pure zinc. Obviously, the two phases do not share any common element; this is a favourable case for thin-film quantification and, thus, for the enhanced quantification. In figure 6.7, results of the enhanced quantification are compared to k-ratios and bulk quantification. On this plot the recursion goes from left to right. The left interface is perfectly treated; the thin-film quantification returns the actual composition at the first voxel. For the right interface, 47% of Al is obtained for the first voxel (point (1) in figure 6.7): far from the actual composition, but closer to it than the k-ratio. In the next voxel, the layer system is defined with a virtual layer of 47% of Al under the upper layer. The result is still not the actual composition, but again closer to it than k-ratio. This continues until the actual composition is reached. The resulting curve forms a sharper interface than k-ratios curve, with an improvement of composition for each voxel up to 25%. The inappropriate bulk quantification gives a slightly worse Al content compared to k-ratios.

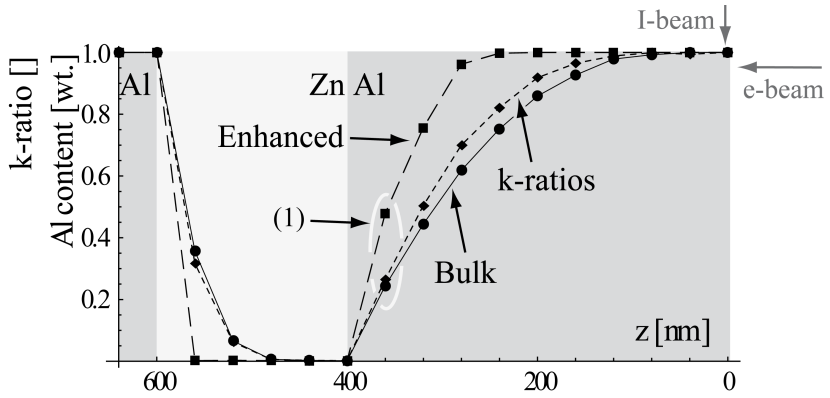

Figure 6.7: Test of the enhanced quantification on simulated profile along z (see figure 6.3(b)). The two interfaces are parallel to the surface. Beams position is indicated at the top right.

Bastin *et al.* established a database of X-ray intensities measured on thin films [53, 61]. He has deposited aluminium and palladium films of different thicknesses on a large range of substrates. He has measured spectra at different accelerating voltages with a wavelength dispersive spectrometer (WDS)[5]. He has extracted the k-ratios of all accessible X-ray lines[6]. The results were

[5] WDS detector has a smaller energy resolution than EDS detector. By construction k-ratios are independent of acquisition parameters; k-ratios of the two techniques are equivalent.

[6] k-ratios measured on 2 different films of Al and Pd, on 20 different substrates from Be to Bi, with 6 different

used to test and to improve the k-ratios predicted by his thin-film method.

As illustrated in figure 6.8(a), this database is adapted to test the enhanced quantification; the thin-film measurements are converted in profile along z. Data are grouped in thin-film systems of same substrate, same film, and same V_0. Thicknesses t of each system are related to the respective z values. The enhanced quantification method is applied to all profiles. Similar results are obtained with both film materials; only results with Al films are presented.

Profiles of three selected substrates are presented in figure 6.8(b). Si, Zr and Au have different densities[7], and the presented X-rays lines are chosen in different families. Considering these properties, Si is close to Al, and Zr is close to Zn of our study-case sample: the database contains no Zn substrate. The Al k-ratios for the three profiles are very similar (only one set of k-ratios is plotted). The enhanced quantification shows as global improvement. Better results are obtained for smaller atomic number with an almost perfect interface for Si. Zr curve is not regular, showing a step. This behaviour is observed for substrates with high atomic number and is more pronounced for high V_0. This will be discussed later.

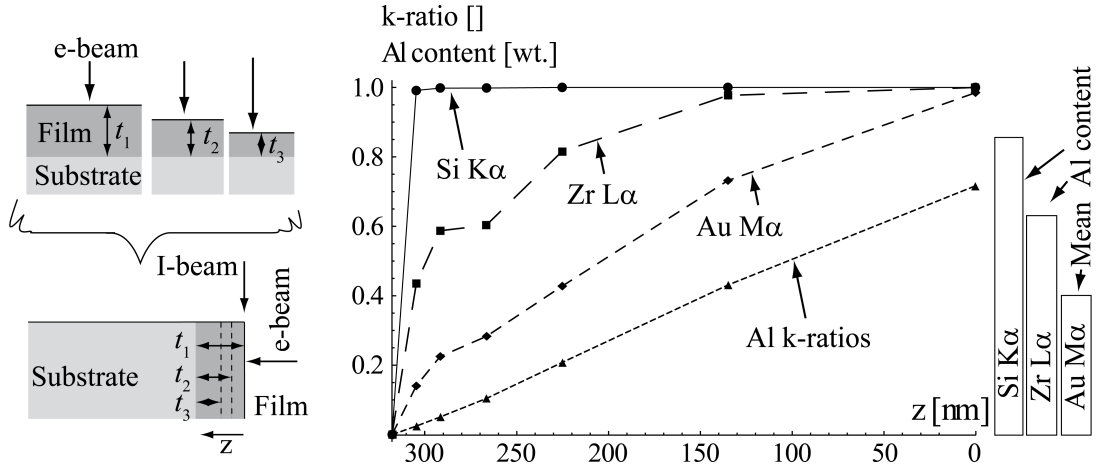

(a) Conversion of measurements on a set of thicknesses into a profile along z.

(b) Enhanced quantification on profile of Al films on 3 different substrates measured at 8 kV. X-ray line of substrate is given. One set of Al k-ratios is shown for the 3 substrates. The mean over all displayed points (Al content) is given at right for the 3 substrates.

Figure 6.8: Thin-film database used to test the enhanced quantification.

To evaluate the accuracy of the enhanced quantification, each profile is considered with aluminium-content averaged over all voxels, as shown in the inset at the right of figure 6.8(b). In figure 6.9(a) and (b), aluminium content is plotted in function of V_0 and R_x of substrate X-ray line in substrate ($R_{x,sub}$) respectively; the aluminium content is given by the average over all profiles having the same V_0 or R_x. In figure 6.9(a), curves of k-ratios and of the enhanced quantification similarly decrease, as V_0 increases. The difference between curves is relatively constant, around 30%. V_0

thicknesses from 10 nm to 320 nm, and with 10 different V_0 from 3 kV to 20 kV.

[7] ρ = 2.3 g/cm^3, 6.5 g/cm^3, and 19.3 g/cm^3 for Si, Zr, and Au respectively

is the parameter showing best the correlation between inputs and outputs.

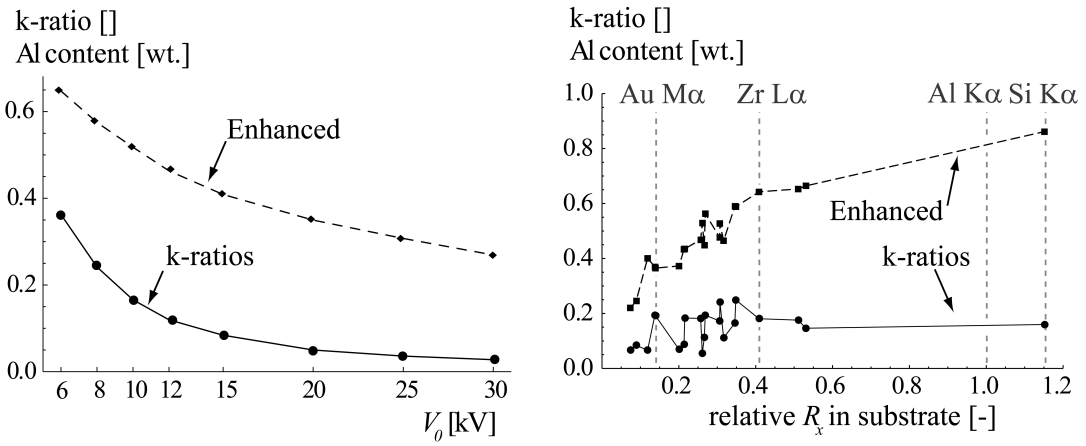

(a) Mean Al content plotted in function of accelerating voltage (V_0).

(b) Al content plotted in function of R_x for substrate X-ray line in substrate ($R_{x,sub}$). This R_x is scaled relatively to the R_x for Al Kα in the Al film ($R_{x,film}$).

Figure 6.9: Enhanced quantification tested on profiles with Al film from Bastin's database [53]. Al contents are averaged over voxels and profiles of the same parameters value.

For figure 6.9(b), $R_{x,sub}$ was chosen because it is the parameter showing the best correlation between substrate and the enhanced quantification. The higher is $R_{x,sub}$, the higher is the enhancement in Al content, while k-ratios show little variation and no clear correlation. On Au substrate, the enhancement is one of the lowest, and, on Zr substrate, the enhancement is medium. The best result is obtained with Si substrate that has $R_{x,sub}/R_{x,film}$ the closest to one, $R_{x,film}$ being R_x for Al Kα in the Al film. Results on Pd films are globally better, and the same behaviour is observed. The curve of the enhanced quantification reaches quickly 1 with $R_{x,sub}/R_{x,film}$ higher than one.

$R_{x,film}$ depends on V_0 by a power law (see Anderson and Hasler's equation 2.2). The two parameters that described best the global accuracy of the enhanced quantification are thus $R_{x,film}$ and $R_{x,sub}$. When $R_{x,film}$ is lower, more X-rays are emitted from the film, and the profiles form a sharper interface for the Al k-ratios and, hence, for the enhanced Al contents. The fact that the k-ratios are not influenced by $R_{x,sub}$ suggests that the variations are induced by inaccuracies of the enhanced quantification and, consequently, of the thin-film quantification. The main assumption of this quantification is the continuity of $\phi(\rho z)$ curves. We can suppose that a too big difference between $R_{x,sub}$ and $R_{x,film}$ leads to conditions invalidating the assumption and leading to inaccuracies.

Compound materials

The case of substrate and film containing the same elements in different composition is unfavourable for the thin-film quantification. The enhanced quantification is tested on such case, with a profile through compound materials. The sample is formed of an aluminium-rich phase containing 20 wt.%Zn and a zinc-rich phase containing 20 wt.%Al. The simulated profile is shown in figure 6.10. Globally enhanced Al contents are closer to the actual composition than the bulk quantification. However, an oscillating behaviour is observed at the left interface. The first voxel after the interface has an Al content 10.7% too low, the next has an Al content 1.4% too high, and the following has an Al content 1.0% too low. The oscillations are stopped when the homogeneity test is fulfilled and the bulk quantification is used. This behaviour is less pronounced at the other interface. The oscillations are due to inaccuracies of the thin-film quantification at one voxel reported on the following one during the recursion.

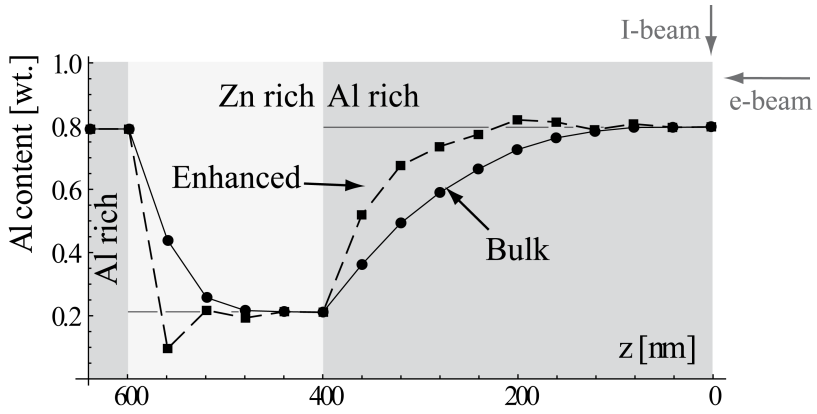

Figure 6.10: Test of the enhanced quantification on profile along z through compounds materials. The Al rich phase contains 20 wt.%Zn, and the Zn rich phase contains 20 wt.%Al. The phase compositions are indicated by horizontal grey lines. The interfaces are parallel to the surface. The beams position is indicated at the top-right corner.

6.3 Full method

3D EDS stacks are acquired with a tilt angle. X-rays distribution and, hence, mapping are affected. The assumption of the first approach is not valid. Enhanced quantification is adapted into a full method taking tilt into account, and the method is tested on 3D EDS stacks simulated and measured.

6.3.1 Tilt effect

In the acquisition geometry, the milled surface is tilted of 90°-α, in the present case 36°. Figure 6.11(a) shows the X-ray distribution for Al with an electron beam tilted of 36°. The colour code indicates the relative number of X-ray in bins of 40 x 40 x 40 nm^3. The black line shows the direction of the beam in the sample. Compared to the distribution with no tilt (see figure 6.2(a)), the tilted distribution is globally inclined following this line. The column of voxels under the central voxel contains way less X-rays, from 32 % to 24 % for Al. The assumption of the first approach is not considered as valid.

The influence of tilt on mapping is illustrated in figure 6.11(b). Profiles on the surface are simulated through interfaces perpendicular to the direction of the profile. The profiles along y correspond to 36° and -36° of electron-beam tilts. The profile with -36° tilt is equivalent to a profile with 36° tilt and with Al and Zn phases inverted. The profile along x corresponds to 0°. A signal spreading different for each tilt value is observed. The tilt induces a shift of the profile in the sense of the tilt direction. Both spreading and shift are smaller when the beam is tilted in the direction of the densest material, as the electrons have to go first through a denser material.

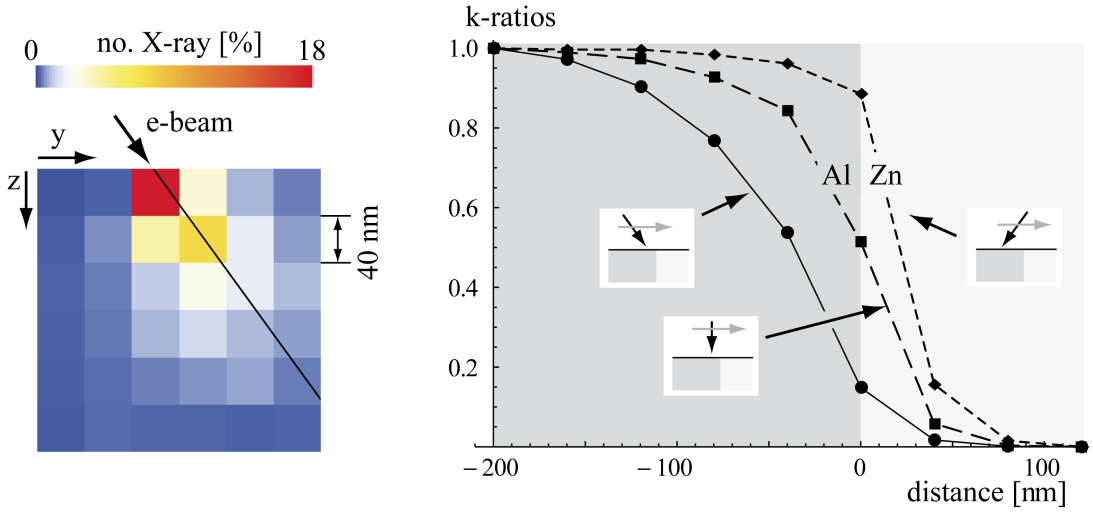

(a) Distribution of emitted X-rays for Al Kα in pure Al. Logarithmic colours code scales the relative number of X-ray contained in a bin. Bins have a size of 40 x 40 x 40 nm^3.

(b) Influence of tilt on surface profiles with tilt 36°, 0°, and -36°. Interfaces are perpendicular to profile direction. K-ratios of Al Kα are plotted in function of distance to interface.

Figure 6.11: Effect of tilt on X-ray distribution and profiles. The surface is tilted of 36° and the accelerating voltage is 5 kV.

6.3.2 Implementation

Voxel definition

A new system of index for y axis is introduced in figure 6.12. In y and z, i, j are indexes of the central voxel, and m,n indexes indicate voxels relatively to i, j.

Considering the tilted X-ray distribution of figure 6.11(a), an important amount of X-rays is emitted from the voxel i+1, j on the right of the central voxel. To obtain voxels more representative of the measured spectra, the voxel's centre is shifted towards positive y. As shown in figure 6.12, the shifted central voxel contains more trajectories of energetic electrons and, hence, produces more X-rays. With simulated electron distribution, an optimum is found at a shift of 0.49 times the voxel size, just at the border of the voxel. In aluminium with trajectories plotted in figure 6.12, the shifted voxels i, j contain 1.3 times more electrons than without shift.

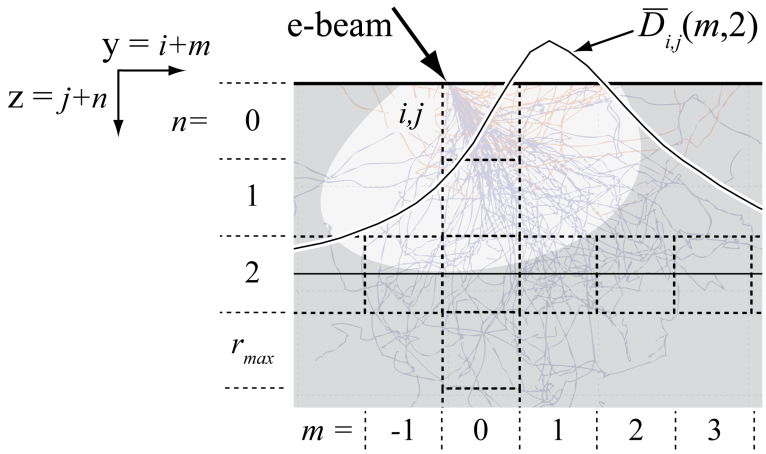

Figure 6.12: Index system definition for full method implementation. The central voxel is indicated by indexes i, j and m,n are indexes relative to this voxel. Electron trajectories for the voxel i, j are simulated for Al at 5 kV. The corresponding $\overline{D}_{i,j}(m,n)$, the curve of weighting factors is plotted in function of continuous m for n=2.

Extension to tilted sample

To extend the enhanced quantification to the tilted sample, compositions in the layer system are adapted considering the electron distribution. In equation 6.1, the voxel composition j+n ($\mathbf{C}_{i,j+n}$) is replaced by $\overline{\mathbf{C}}_{i,j+n}$. This composition is the weighted mean of neighbouring-voxels in layer j+n. $\overline{\mathbf{C}}_{i,j+n}$ is defined as follow:

$$\overline{\mathbf{C}}_{i,j+n} = \sum^{m} \overline{D}_{i,j}(m,n)\mathbf{C}_{i+m,j+n}, \tag{6.2}$$

with $\overline{D}_{i,j}(m,n)$ the weighting factors, as plotted in figure 6.12 for n=2. $\overline{D}_{i,j}(m,n)$ is derived from simulated electron distribution:

$$\overline{D}_{i,j} = \sum^{A} D_A \text{k-ratio}_{i,j,A}, \tag{6.3}$$

where D_A is the electron distribution in pure material A and projected on the y axis. k-ratios$_{i,j}$ are taken as an estimation of the global composition. All D_A are simulated before the global recursion to save computing time.

Implementation of recursion

The recursion of the first approach is consequently adapted (see flow chart of figure 6.6); a second loop on voxel along i is added just inside the loop along j, and $\overline{D}_{i,j}$ is calculated before defining the layer system. In figure 6.12, $\overline{D}_{i,j}(m,n)$ is shifted towards positive y due to tilt. $\overline{D}_{i,j}(m,n)$ covers both side of the central voxel; $\mathbf{C}_{i+m,j+n}$ with positive and negative m are needed to determine $\overline{\mathbf{C}}_{i,j+n}$ (see equation 6.2). However, only half of $\mathbf{C}_{i+m,j+n}$ are calculated inside the loop on i. Because of the shift of $\overline{D}_{i,j}(m,n)$, the loop on i is set backwards. $\mathbf{C}_{i+m,j+n}$ with negative m are then approximated by k-ratios$_{i+m,j+n}$. When i+m exceeds the limits of i, $i-m$ is used; Borders in y are extended with mirror voxels.

6.3.3 Test on simulation

The full method is first tested on a simple three-dimensional object modelling the test-case sample. Aluminium precipitates are simulated by a sphere of pure aluminium in a pure zinc matrix. The sphere has a diameter of 280 nm, slightly smaller than the R_x of Al Kα in Al (~300 nm). The simulation geometry is illustrated in figure 6.13(a). A mapping of 11 x 11 x 14 voxels is simulated. The electron trajectories for one voxel are shown. Orthogonal views through the sphere centre are shown in figure 6.13(b). To show the actual effect of the interaction volume, centre of coloured squares indicates the electron-beam position and not the voxel position.

Inside the sphere, the highest Al k-ratio is 0.75; even if the sphere diameter is close to R_x of Al Kα in Al, *i.e.* 310 nm, a good amount of Zn Lα is emitted. Al content is far away from 100% for the bulk quantification and is about 40% higher for the enhanced quantification. Outside the sphere, Al content is generally lower for the enhanced quantification. The maximum of Al content of bulk quantification is shifted from the centre towards negative z value and towards negative y value. This shift is partially corrected with the enhanced quantification.

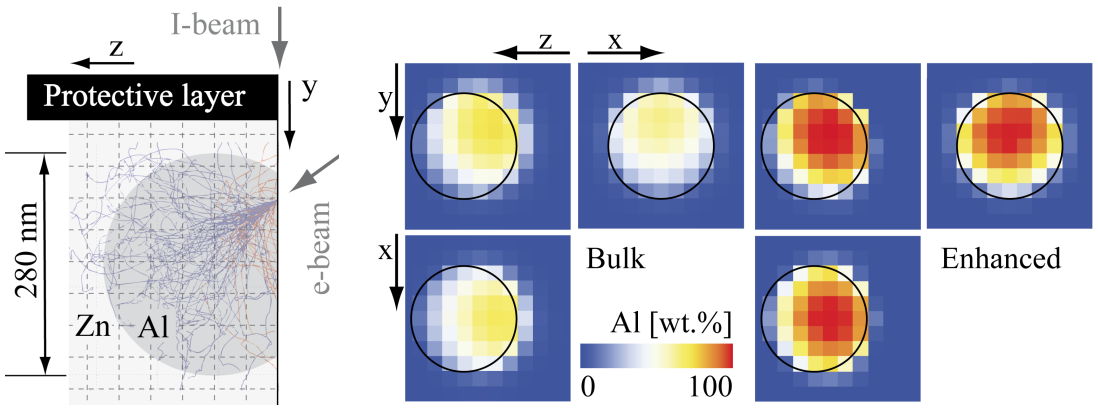

(a) Simulation geometry. The model is composed of an Al spherical precipitate in Zn matrix. Voxels of 40 x 40 nm^2 and electron trajectories for one voxel are shown.

(b) Orthogonal views through the sphere centre. Centre of coloured squares indicates the beam position. The sphere border is drawn with black circles.

Figure 6.13: Enhanced quantification tested on simulated data of a modelled AlZn sample.

Figure 6.14 shows profiles along the main axes through the sphere centre. The profile along z is resembling the first tested profile (see figure 6.7); the results are very similar. The enhanced improves k-ratios from depth and from tilt effect.

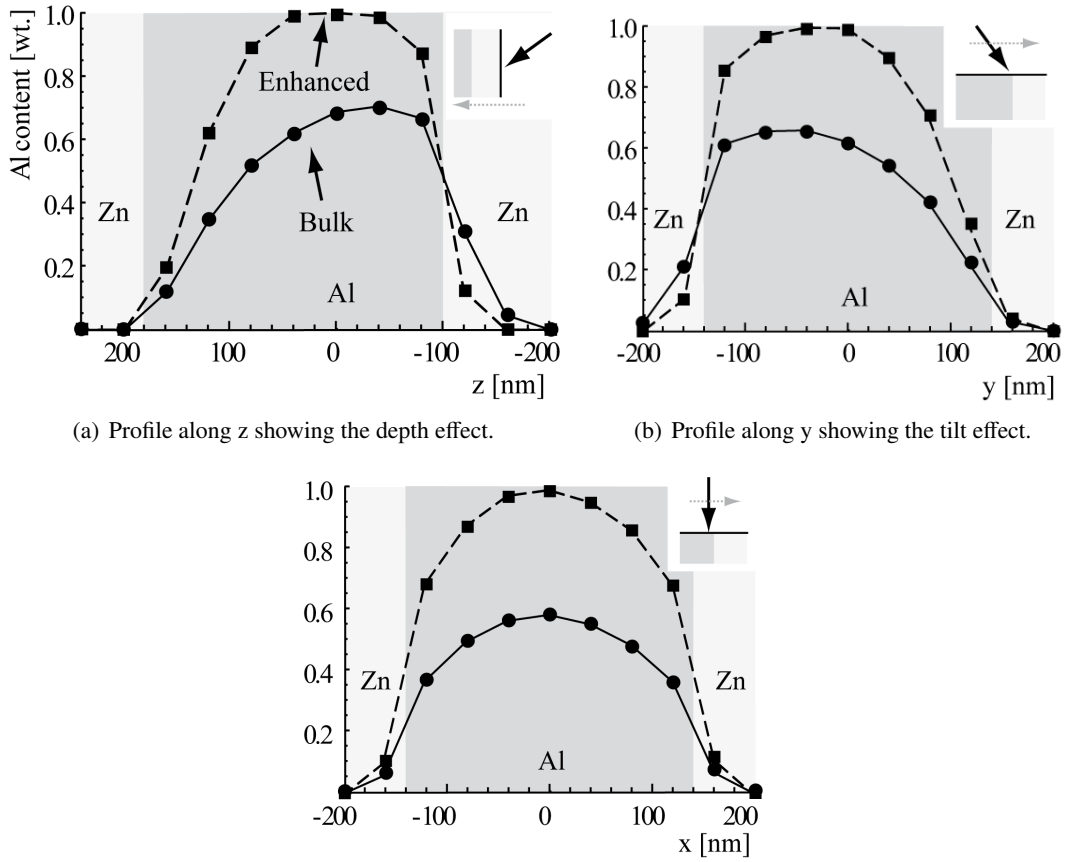

(a) Profile along z showing the depth effect.

(b) Profile along y showing the tilt effect.

(c) Profile along x.

Figure 6.14: Profile through the sphere centre. Insets at the top right of each profile indicates the beam orientation. Al content is plotted in function of the beam position relative to the sphere centre.

6.3.4 Test on measured data

With the measured data, two new factors are added compared to the test on simulations: noise and a more complex microstructure. The data acquired on AlZn sample has a rather low level of noise and a simple microstructure. On the other hand, the data acquired on NiTi-SS sample have a high level of noise and a complex microstructure.

For both samples, k-ratios are extracted from the data stack, previously noise-filtered with PCA in the case of NiTi-SS sample (see section 5.2.1). The k-ratio stacks are then aligned using SE stack as reference. Before the enhanced quantification, the k-ratios are normalized to one as it helps reduce noise (see section 5.3.2). After the enhanced quantification, the quantified stacks are spatially smoothed with an isotropic median filter after doubling the number of voxels, as defined in section 5.2.2. All results are presented before smoothing to show raw effects of the enhanced quantification. Presented for comparison, bulk-quantified stacks follow the same processing steps.

In the simulation, the exact geometry and the composition of the model microstructure are known. In the case of measured data, spatial and compositional references are needed to prove that the compositions obtained by the enhanced quantification describe better the actual sample and do not suffer from artefacts. The composition of metallic alloys at equilibrium is theoretically predicted by the phase diagram; the phase diagrams introduced in section 3.1 are used as compositional reference. Due to their low energy, SE have an escape depth of less than 10 nm. The spatial resolution of SE images is in the same order of magnitude, considering that the image contrast is formed mainly by the SE generated at the probe location (SE1) [4]. This resolution is at least 10 times better than the one obtained by EDS for the two studied samples. Recorded with 8 times more voxels in each direction (see section 3.2.2), the SE stacks are used as a spatial reference.

AlZn sample

Figure 6.15 shows orthogonal views through the stacks of the test-case sample. In the SE stack, particles are well defined. The stack contains some larger particles of ~300 nm at low value of z. The rest of the particles has a mean size of ~100 nm. In the bulk-quantified stack, particles appear more blurry than in the enhanced-quantified stack. In this stack, more aluminium is obtained at the particle's position given by SE image. Inside the bigger particle, the enhanced-quantified maps are noisy. This noise is less present for map xy at the top right.

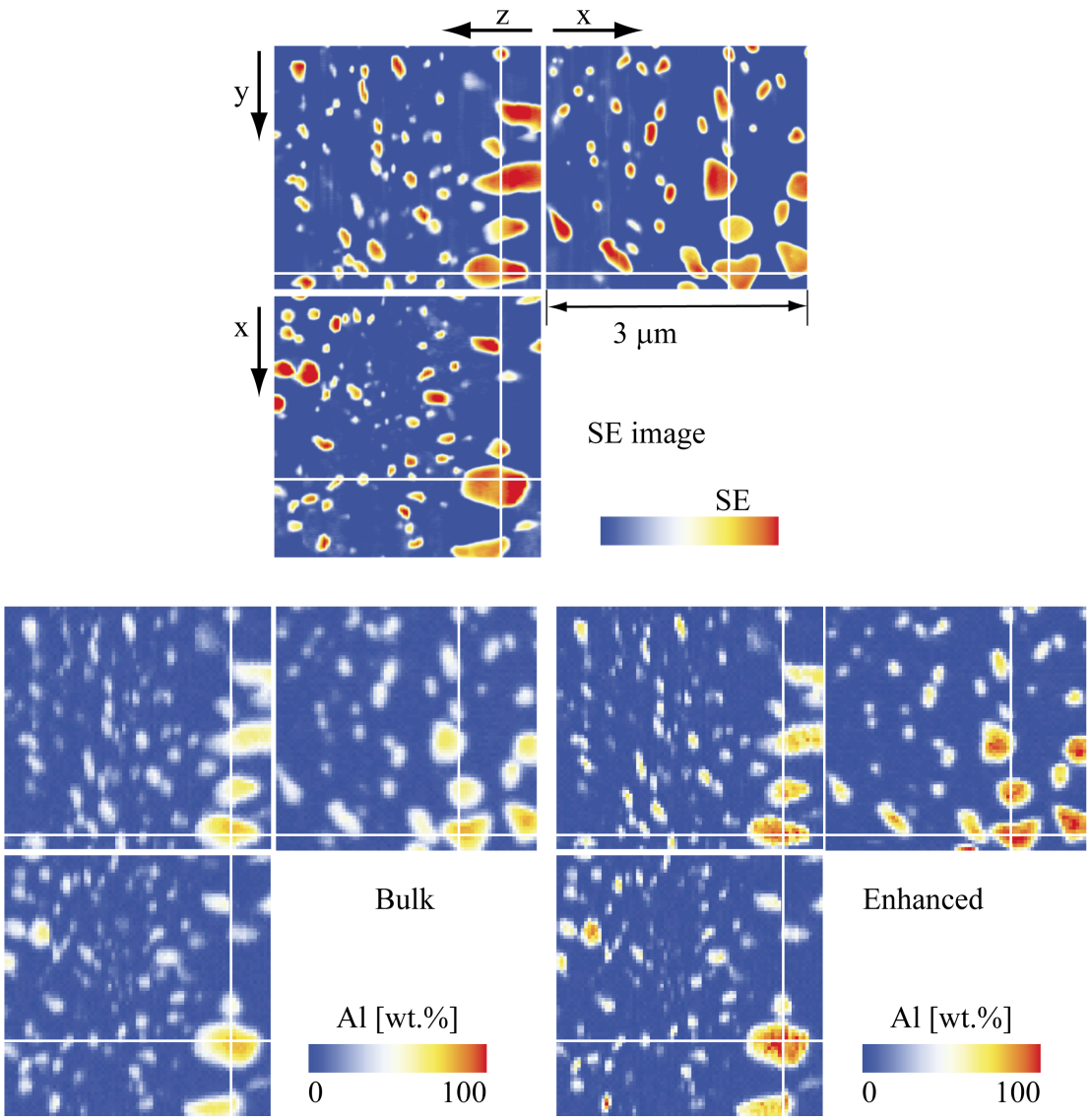

Figure 6.15: Orthogonal views through the AlZn stacks. For SE stack, colours scale is set arbitrarily to obtain pictures similar to the others. The white lines show the position of the other orthogonal views.

In figure 6.16(a), a profile along z is shown. It goes through the big particle at the crossing of all white lines of figure 6.15. The k-ratios are plotted for comparison with the enhanced quantification. The SE signal gives a spatial reference for the position of the interfaces[8]. At the right interface, the three curves have a sharp and regular shape. Each enhanced content is lower than the k-ratio curve forming a profile close to the SE reference. At the left interface, the k-ratio curve is flatter and has a slightly irregular shape. Each enhanced content is overall higher than the k-ratio, but the curve oscillates between voxels. Every k-ratio with a value higher than the mean slope results in an over-estimated Al content (*e.g.* point (1)), over-compensated in the next step (*e.g.* point (2)).

A more regular interface can be obtained by smoothing k-ratios with the PCA method. This behaviour is linked to inaccuracies passed on by the recursion, similarly to what is observed for compound materials (see figure 6.10). However in this case, inaccuracies are mainly due to noise in the input data. The principal recursion is along z, oscillations are thus observed only in this direction. As oscillations have a short period, they are easily smoothed, for instance with a mean filter along z.

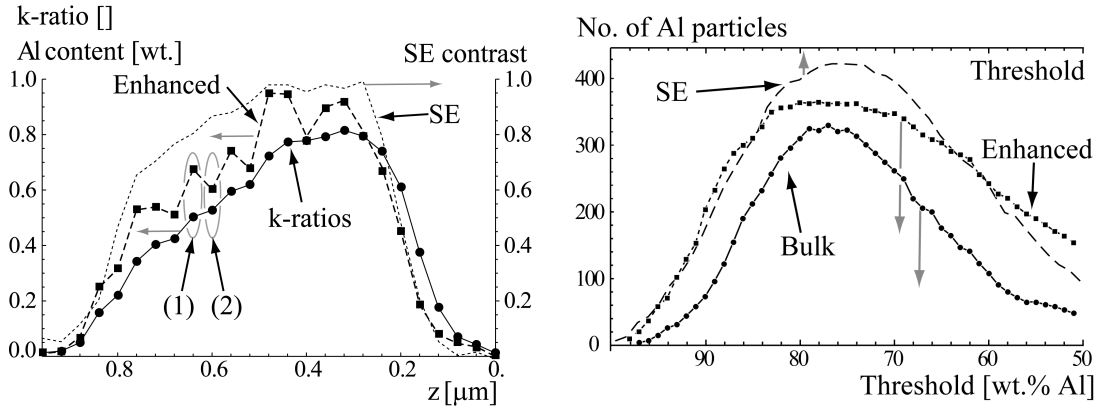

(a) Oscillating behaviour of the enhanced quantification. Profile along z through the big particle at the crossing of the white lines of figure 6.15. SE contrast is adjusted from 1 to 0.

(b) Statistics on the three stacks. Number of particles is plotted in function of threshold. The threshold scale for SE is adjusted to obtain a maximum at the same position as the other curves.

Figure 6.16: Details on the enhanced quantification applied on data measured on AlZn sample.

After spatial smoothing, the final enhanced stack is obtained. To quantify the gain through this method, the whole stack is characterized by the number of particles counted for a given global threshold. In figure 6.16(b), the enhanced quantification is compared to bulk quantification. To be comparable to EDS stacks, SE voxels are binned together, and the threshold scale is adjusted to obtain a maximum at the same position than the other curves. All curves show the same shape; first an increase, then a maximum before a decrease. For high values of the threshold, only the bigger particles with the highest Al content are selected. The particle number increases as the threshold decreases. When threshold is low enough, the curves start to decrease as close particles

[8]Minimum and maximum of SE signal are scaled from 0 to 1 respectively.

start to coalesce. The enhanced curve shows a quick increase for high values of threshold, since particles have higher Al content. This curve has a higher maximum and a slower decrease than the bulk curve; fewer particles coalesce together, they are better defined.

NiTi-SS sample

The normalized k-ratios of the three main elements are used to test the enhanced quantification. Considering the X-ray lines of these elements and the four phases that can form, the corresponding R_x range from 210 nm to 440 nm. These values are slightly closer one to others than the R_x values in AlZn sample. 440 nm corresponds to 4.4 times the voxel size (7.75 in AlZn); the range is smaller relative to voxel size. Without considering the higher noise, the enhanced quantified results should hence be similar to the one of the AlZn sample.

Figure 6.17 shows a simulated profile along z through two phases, γ-(Fe,Ni) and Fe_2Ti, which compose one of the fine microstructures. The composition of the phases is approximated based on the phase diagram and the quantified maps. Nickel is set constant and is not displayed. The two closest voxels at the right of interfaces deviate from the phase composition and are corrected by the enhanced quantification. Because of this short range influence, the oscillation problem is strongly reduced in this profile without noise.

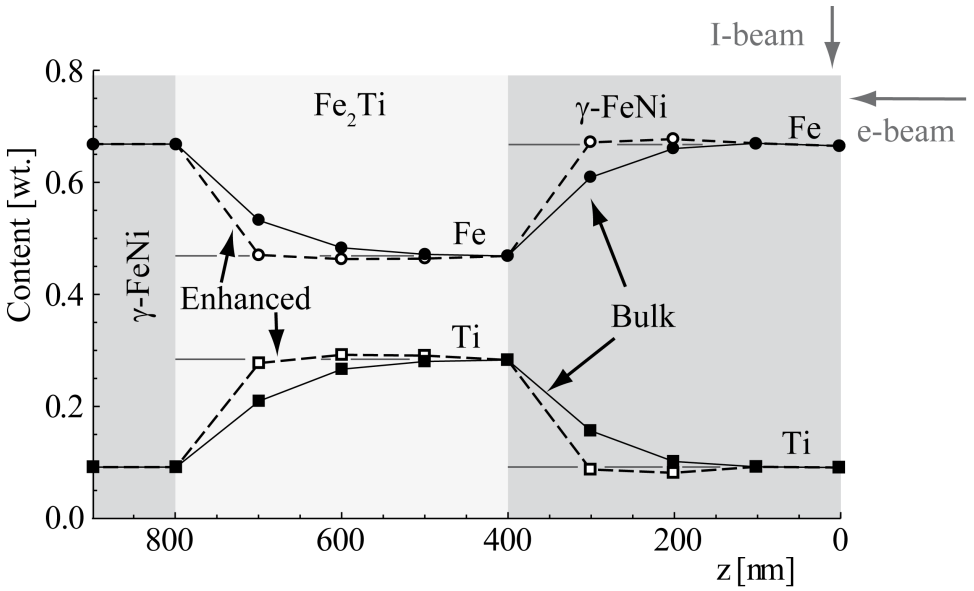

Figure 6.17: Simulated profile along z through interfaces between γ-(Fe,Ni) and Fe_2Ti phases. The bulk quantification is compared to the enhanced quantification. Ni content is constant and not displayed. The phase compositions are indicated by horizontal grey lines. The interfaces are parallel to the surface. The beams position is indicated at the top-right corner.

The raw results of the enhanced quantification are compared to the bulk quantification in figure 6.18. Ternary histograms and orthogonal views through the Ti concentration in the stack are shown. Titanium is considered because it shows variations in the different fine microstructures. The results for the three elements are found in appendix B. Still present after filtering with PCA, the noise is increased by the enhanced quantification as observed in the Ti maps, and peaks broadening can be observed in the histogram. As suggested in the previous section, a mean filter along z is applied on the enhanced quantified stacks. Ti maps are efficiently smoothed, and the ternary histogram shows narrower peaks. However a blurring along z is observed; a part of the enhanced quantification gain is lost.

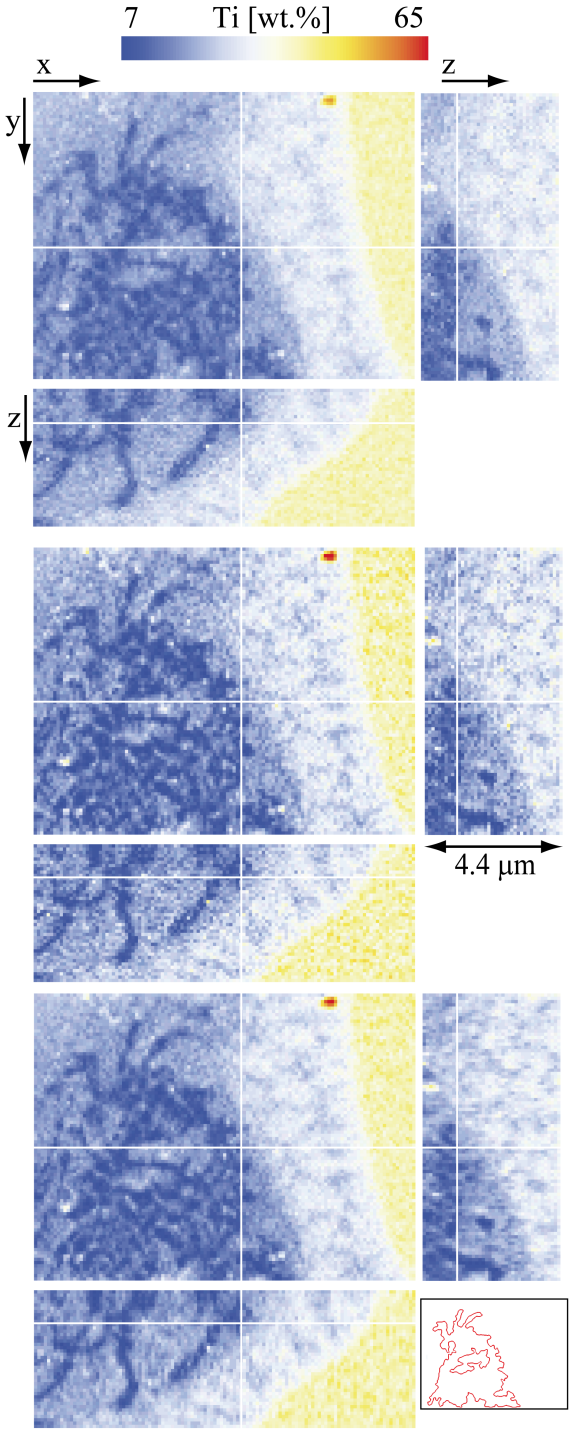

(a) Orthogonal views of Ti quantified stacks scaled by a colours code. The white lines show the position of the other orthogonal views. At the bottom right, the area drawn in red corresponds to the fine microstructure formed by γ-(Fe,Ni) and Fe_2Ti phases.

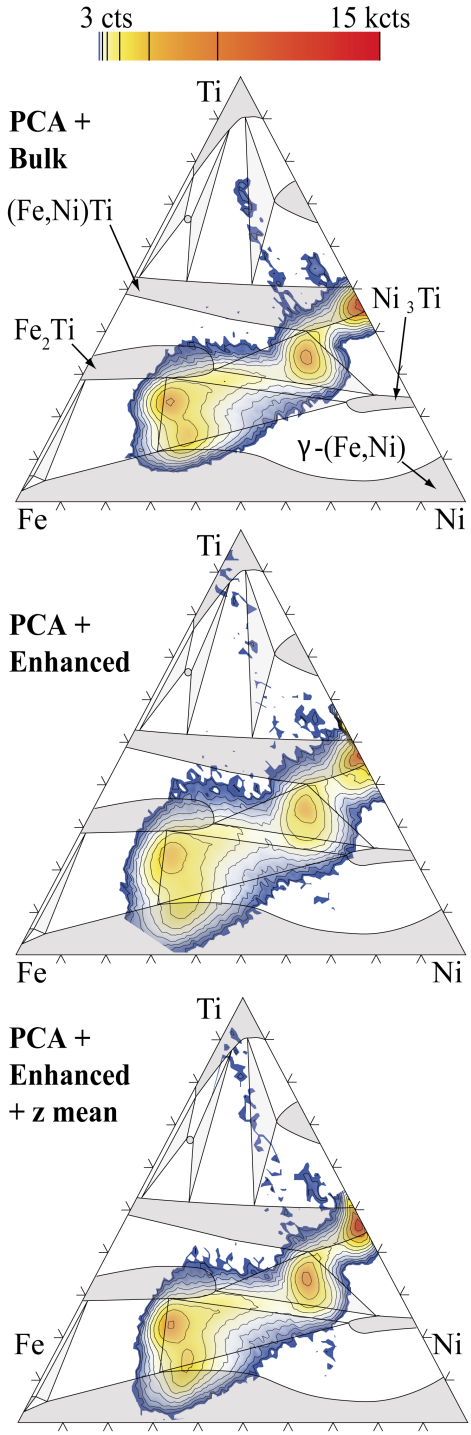

(b) Ti-Fe-Ni ternary histograms scaled by colours code and iso-contours. A ternary phase diagram cut at 1000°C is superimposed [45].

Figure 6.18: Orthogonal views and ternary histograms of NiTi-SS quantified stacks. The bulk quantified stack is compared to the enhanced quantified stacks raw and smoothed along z with a mean filter.

To quantify the effect of the enhanced quantification on the noise level, a set of voxels selected in the NiTi phase is used, as defined in section 5.1. Figure 6.19(a) shows the histogram of Ti k-ratio and Ti enhanced content relative to the mean k-ratio/content. The histogram of the enhanced content is broader due to the oscillations. The broadening is not uniform; the bottom is broader than the upper part of the histogram, as if there are two different distributions. This is caused by the test of homogeneity: voxels are split in two distributions if the test is passed or not. In the present case with a limit ϵ_c of 3 wt.% (see section 6.2), 40% of the voxels in the set pass the test. Increasing ϵ_c will decrease the global efficiency of the enhanced quantification; the test needs to be improved. Applying the mean filter along z, a good part of the bottom broadening is removed. Figure 6.19(b) shows the evolution of the noise level with or without the enhanced quantification. The increase due to the enhanced quantification is partially removed by the two smoothing steps.

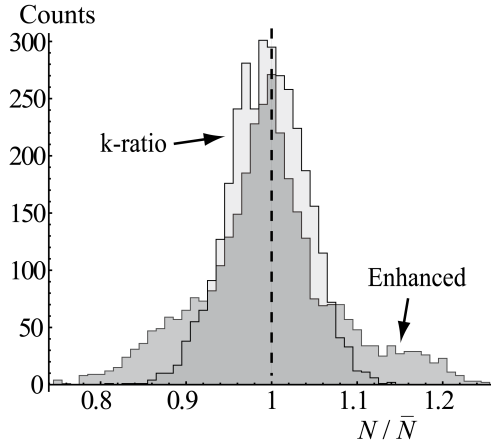

(a) Histogram of Ti k-ratio (normalised and aligned) and Ti enhanced content. The bin size is 1%.

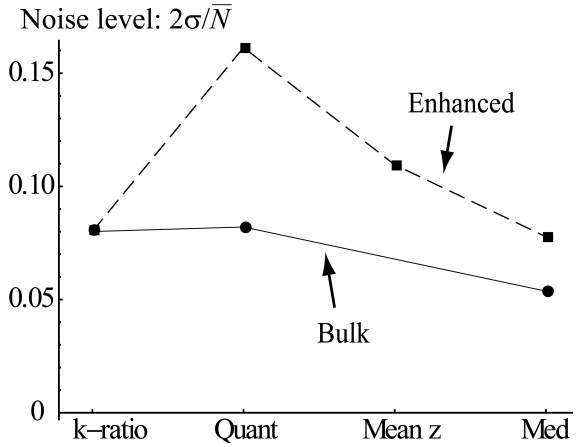

(b) Noise level at different steps of the quantification procedure. $2\sigma/\overline{N}$ is calculated for Ti k-ratio and Ti contents obtained by enhanced or bulk quantification (raw, smoothed with mean filter along z, and smoothed with 3D median filter).

Figure 6.19: Increase of noise level due to enhanced qualification. The noise level is measured on a set of voxels selected in the NiTi phase, as defined in section 5.1.

In the profile simulation, voxels close to the interface show an increase/decrease of Ti being in rich/poor Ti phase respectively. This leads in the Ti map to an increase of contrast. The fine microstructure formed by γ-(Fe,Ni) and Fe_2Ti phases is indicated by the red area at the bottom right of figure 6.18(a). In this region, an increase of contrast is observed with the enhanced quantification; the structure is better defined. As predicted by simulations, the enhanced Fe stack shows a similar increased contrast, while the contrast of the Ni stack stays constant. In the histogram, this should correspond to a further split of the γ-(Fe,Ni) and Fe_2Ti peaks along a line of constant Ni. The γ-(Fe,Ni) peak indeed moves to higher values of Fe, closer to the composition predicted by the phase diagram. However, the shift of Fe_2Ti peak is not significant, since the Fe_2Ti phase mainly forms a bigger microstructure that is less influenced by the enhanced quantification.

The improvement observed for the fine microstructure is confirmed with figure 6.20 in a comparison with the SE image. For a better visualisation, bulk and enhanced quantified stacks are spatially smoothed. All the fine microstructures that are better defined with the enhanced quantification are related to fine details in SE image.

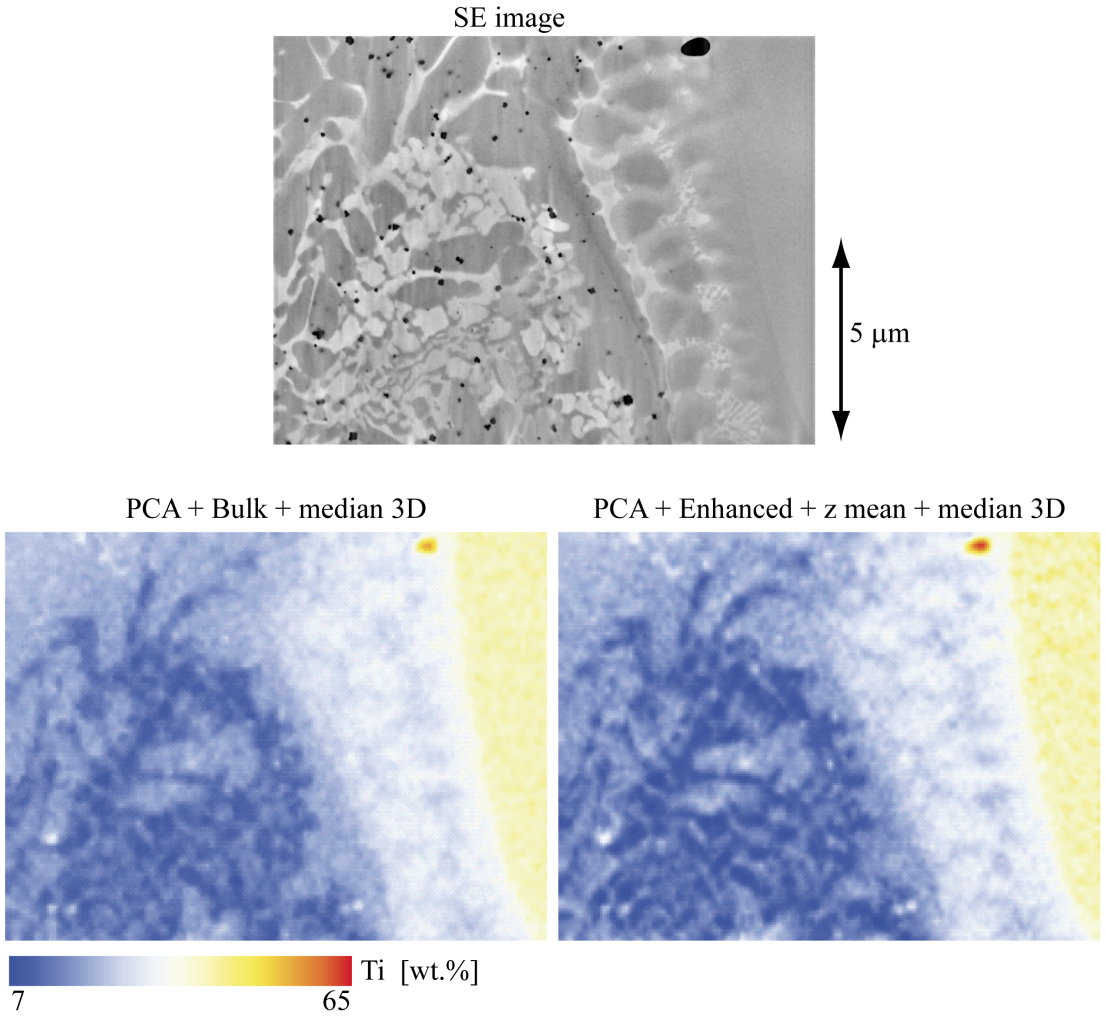

Figure 6.20: Comparison of the two quantification methods with SE image. Ti maps are smoothed with a median filter after doubling the number of voxel.

6.4 Synthesis and improvement perspectives

In case of a voxel size smaller than the interaction volume, an enhanced quantification method was implemented correcting the influence of deeper voxels: a thin-film quantification is recursively applied on voxels along z. Out of several tests on simulated and experimental data, the limits of the method have been studied. The recursion amplifies imprecisions inducing an oscillating behaviour. These imprecisions result from noise in the input, the measured k-ratios, and from inaccuracies in the thin-film quantification. This procedure loses accuracy when the layer system is unfavourable: when layers share common elements leading to an increased risk of converging to a local solution, and when the difference between the X-ray ranges (R_x) for the different elements in the sample is large.

The method is modified to reduce oscillations. Inputs are smoothed with the PCA method, layer systems are defined in a way to avoid the most unfavourable cases, and the outputs are appropriately smoothed. With this approach, the enhanced quantification has shown encouraging results on two acquired set of data, one having a high level of noise and a complex microstructure. To further improve the method, the oscillation problem should be further addressed with:

- better smoothing of the inputs,
- better defining the layer system with other tests and perhaps refined weighting factors to take tilt into account,
- and addressing the local solution problem, improving initial guesses and predicting the accuracy of the thin-film quantification with a method such as the one suggested by Statham [62].

7 Segmentation

An important processing step towards a comprehensive 3D reconstruction is the segmentation of the analysed volume into subvolumes of uniform properties. In the case of 3D EDS microanalysis, the uniform property is the composition, and each subvolume can be related to a chemically different phase. The acquired stack is composed of EDS maps and SE images. On one hand, EDS maps have a high chemical contrast, but have a relatively low spatial resolution (see section 2.3.2). On the other hand, SE images have a good spatial resolution[1], but have a low chemical contrast [4]. Using the advantages of both EDS maps and SE images, a sample with a complex microstructure, in a chemical and geometrical sense, can be accurately segmented.

Two segmentation techniques adapted to 3D EDS have been reported: A) a straight-forward technique most commonly used to isolate one subvolume is to set up a threshold value for the concentration of one of the elements [16, 19, 22], and B) a segmentation technique based on PCA that has been adapted (see section 2.4.3) [29]. As both of these techniques only rely on EDS measurements without using the high spatial information of SE images, a segmentation technique that exploits the complete set of the data is developed in this chapter. The segmentation technique is presented in two steps. The stack of EDS maps is first segmented using the ternary histogram to define the thresholds. The obtained segmentation is then refined using the contrast of the SE images.

[1] The stack of SE images is used as a spatial reference for the enhanced quantification (see section 6.3.4).

7.1 Segmentation of EDS maps

Before actually using the SE images, the EDS maps are segmented as a starting point using a global thresholding technique (see section 2.4.2). Threshold domains are established by plotting them on the representation of the EDS data in a ternary histogram, as suggested by Bright and Newbury for 2D EDS maps [59]. The threshold technique is applied on the 3D stack acquired on the NiTi-SS sample. The corresponding ternary histogram is first compared with the one of the 2D map of longer dwell time. Methods to define the threshold domains and criterions to set the domain boundaries are then discussed.

As the global technique aims to simplify pre-processing, neither the PCA, nor the enhanced quantification are used. The stack is quantified with $\phi(\rho z)$ method (bulk quantification, see section 2.4.1). For each composition, the concentrations of the three main elements (Fe, Ni, and Ti) are normalised to one, and the stack is smoothed with the 3D median filter defined in section 5.2.2.

7.1.1 Ternary histogram

The quantified stack is represented in a ternary histogram by reporting the Fe-, Ni-, Ti-composition of each voxel in the ternary Gibbs simplex. In the two previous chapters, the ternary histograms were mainly used to qualitatively compare quantified stacks. Overlaying these histograms with an isothermal section of a phase diagram (Fe-Ni-Ti cut at 1000°C [45]), composition domains related to the phases can be defined.

According to the phase diagram (see section 3.1.2), four different phases are involved in the analysed region of the solidified weld. The first one is the unmelted NiTi and its associated solid solution (Fe,Ni)Ti. The three others are Ni_3Ti, Fe_2Ti and γ-(Fe,Ni). In figure 7.1(a), the intermetallic regions of the four potential phases are indicated. In this figure, the ternary histogram of the 2D map with less noise is plotted; its acquisition time per spectrum is 10 times longer than the one used in the 3D stack. Some groups of voxels have similar composition; they form peaks in the histogram that tend to be close to the intermetallic regions of the phases[2]. Selecting such a group of voxels allows to segment the analysed volume into composition domains related to the phases of the phase diagram.

As discussed in section 5.3.2, the noise level of the 2D map is about $\sqrt{10}$ times smaller than the one of the 3D stack. Increased by the logarithmic scale, this difference can be clearly observed between the two histograms of figure 7.1(a) and (b): the whole histogram of figure 7.1(b) is broader. Nevertheless, the global shape is preserved. The different intermetallic regions are distinct enough to define the thresholds used as a starting point for the segmentation.

[2]The composition "path" goes from one potential phase to the other. A paper discussing these results and what they imply in terms of solidification in the weld is under review process [63].

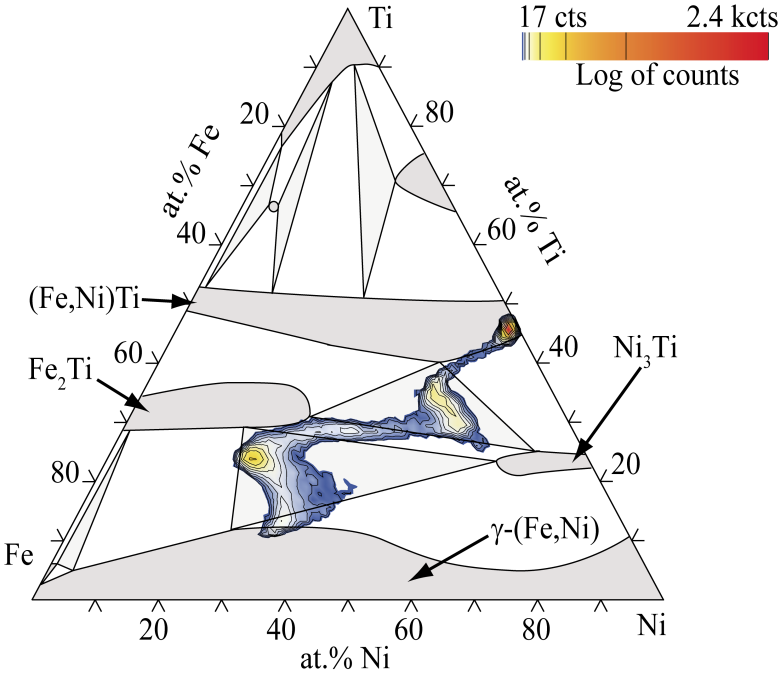

(a) Compositions of the 2D map acquired with a dwell time of 0.3 s.

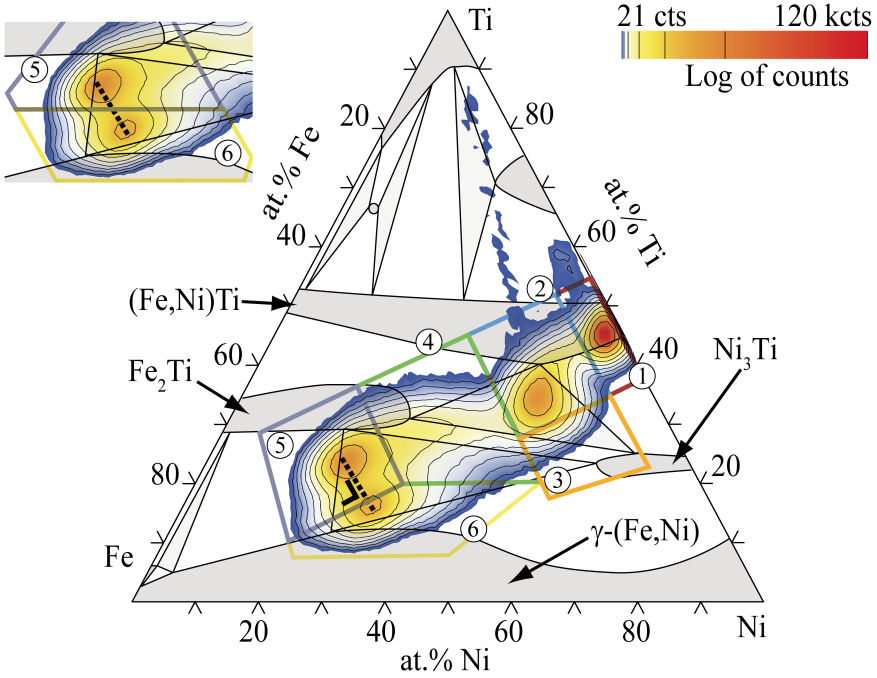

(b) Compositions of the 3D stack acquired with a dwell time of 0.03 s. The labelled polygons give the threshold domain used for segmentation. At top left, the inset shows a part of the ternary histogram with threshold values set parallel to the three main axes of the Gibbs simplex.

Figure 7.1: Ternary histograms of the compositions measured on NiTi-SS sample and displayed in the Fe-Ni-Ti Gibbs simplex. The histograms are superimposed with a 1000°C-isothermal section of the Fe-Ni-Ti phase diagram [45]. The four phases that can form in the sample are indicated. The logarithm colour code and iso-contours used to scale the three compositions is shown in the top right corner.

7.1.2 Defining the threshold domains

For segmentation, the whole analysed volume is divided in composition domains to which voxels are attributed. Depending on the segmentation technique, not all voxels are attributed: this is unwanted as every part of a bulk sample has to belong to a composition domain. Even in the case of porous materials, voxels in pore can be seen as belonging to a "porous domain"[3]. To respect the constraint of "complete attribution", either the segmentation technique needs to be adapted, or the composition domains need to be expanded until all voxels are attributed. The first option is considered using a global threshold technique; the threshold domains must thus cover the whole range of measured compositions.

First approach

In a first approach, a voxel of composition **C** belongs to a domain if the following relation is true for the content C of any element A:

$$T_{min,A} \leq C_A < T_{max,A} \tag{7.1}$$

where $T_{min,A}$ and $T_{max,A}$ correspond to the minimum and maximum threshold values, respectively. On the ternary diagram of figure 7.1(b), these threshold values form lines that define the boundaries of a threshold polygonal domain. A threshold domain can have a maximum of six boundaries parallel to the edges of the Gibbs simplex. Defining the different threshold domains with shared boundaries, the whole range of composition can be covered, and all voxels are attributed to one single domain.

An example of two threshold domains defined by equation 7.1 is shown in the inset of figure 7.1(b) for regions corresponding primarily to Fe_2Ti (region 5) and γ-(Fe,Ni) (region 6). Drawn between these two regions, the dashed line links the two maxima of the ternary histogram and goes through a saddle point in between. With respect to this line, the ternary histogram shows a symmetry that is not respected by the shared boundary of the two threshold domains, since this boundary is parallel to the edges of the Gibbs simplex. This will lead to an incorrect attribution of voxels of compositions close to the boundary between regions 5 and 6.

[3]Porous materials are not considered here. Schaffer has suggested a processing technique for this type of sample [16].

Second approach

In order to define domain boundaries which are not necessarily parallel to the edges of the Gibbs simplex, one more degree of freedom is added to equation 7.1 with a second factor called r for rotation; a voxel of composition $\mathbf{C}$ belongs to a domain if the following relation is true for the content C of any element A_1:

$$\begin{aligned} C_{A_1} &\geq T_{min,A_1} - r_{min,A_1} C_{A_2} \qquad \text{and} \\ C_{A_1} &< T_{max,A_1} - r_{max,A_1} C_{A_2}, \end{aligned} \tag{7.2}$$

where A_2 is an element different than the element A_1. The factors r_{min,A_1} and r_{max,A_1} thus allow to rotate the boundaries of the threshold domain, so that they are perpendicular to the "path" of the composition histogram, as shown in the overall Gibbs simplex of figure 7.1(b).

Six composition domains identified in figure 7.1(b) (domains 1 to 6) have been segmented with this approach. Their composition domains boundaries have shared boundaries and cover the whole range of composition[4]. The constraint of "complete attribution" is respected as each voxels is attributed to one domain.

[4]Two small parts of the ternary histogram with high Ti content are not covered (both sides of no. (2) in figure 7.1(b)). They correspond to TiC and TiO particles that can be separately segmented. They are not considered here to avoid an overloaded representation of the domains.

7.1.3 Position of the domain boundaries

With equation 7.2, the boundaries of the threshold domain are defined with two factors. Criteria to set the two factors are needed for an accurate segmentation. Rotating the boundary, the factor r is set perpendicular to the composition path. Changing the position of the boundary, the factor T can be set considering the ternary histogram, for example at the saddle point observed on the black dashed line (between regions 5 and 6). However the saddle points between the other regions are not well defined. The ternary histogram does not provide a precise criterion to set T. Figure 7.2 shows orthogonal views through the stack of SE images with the composition domains superimposed (1 to 6). As SE images have a better resolution, this type of figure can provide a good criterion, such as set T in order to minimize the average distance between the domain border and the grey level boundary in the SE images. Using this criterion, T is tuned by visual inspection. This approach could be improved measuring the average distance.

The 6 composition domains of figure 7.2 are obtained with this approach. The unmelted NiTi wire and the (Fe,Ni)Ti can be distinguished both with the ternary diagram (more Fe in solution) and the SE image contrast giving the domains labelled 1 and 2. The domain labelled 3 correspond to the Ni_3Ti phase. A complex and fine structure is observed in the SE images at the interface between domains 2 and 3. This structure is not well retrieved with the two segmented domains. A grey contrast boundary systematically appears in the Fe_2Ti phase. This domain is segmented arbitrarily into two sub-domains labelled 4 and 5. Inside the domain labelled 6 corresponding to γ-(Fe,Ni), a fine structure is observed with SE images. This suggests that domain 6 is actually composed of two sub-domains, but no satisfying separation is obtained with the segmentation technique.

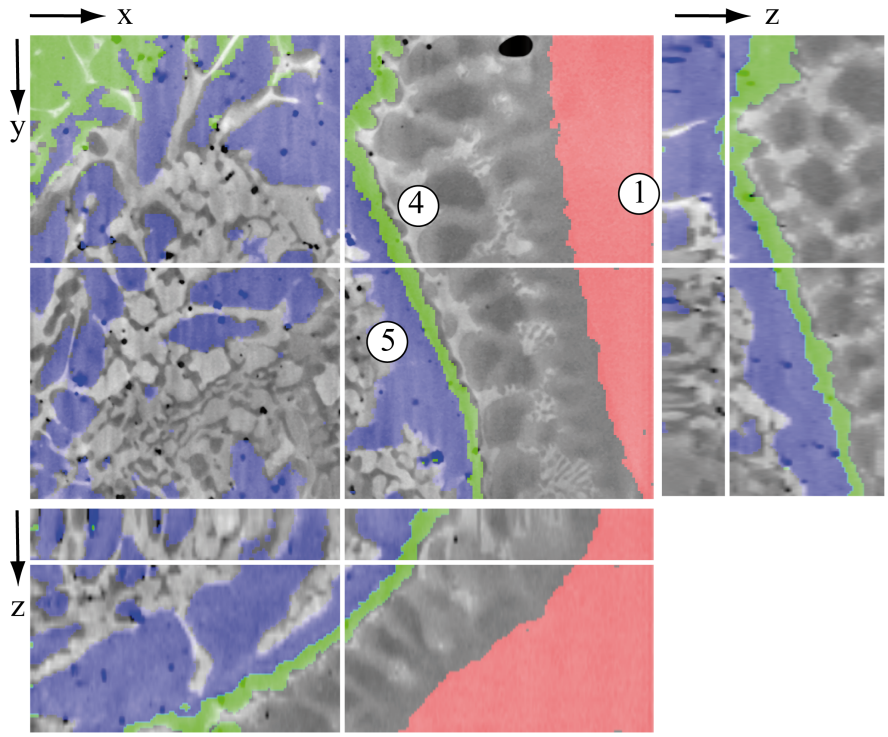

(a) Domains 1, 4, and 5.

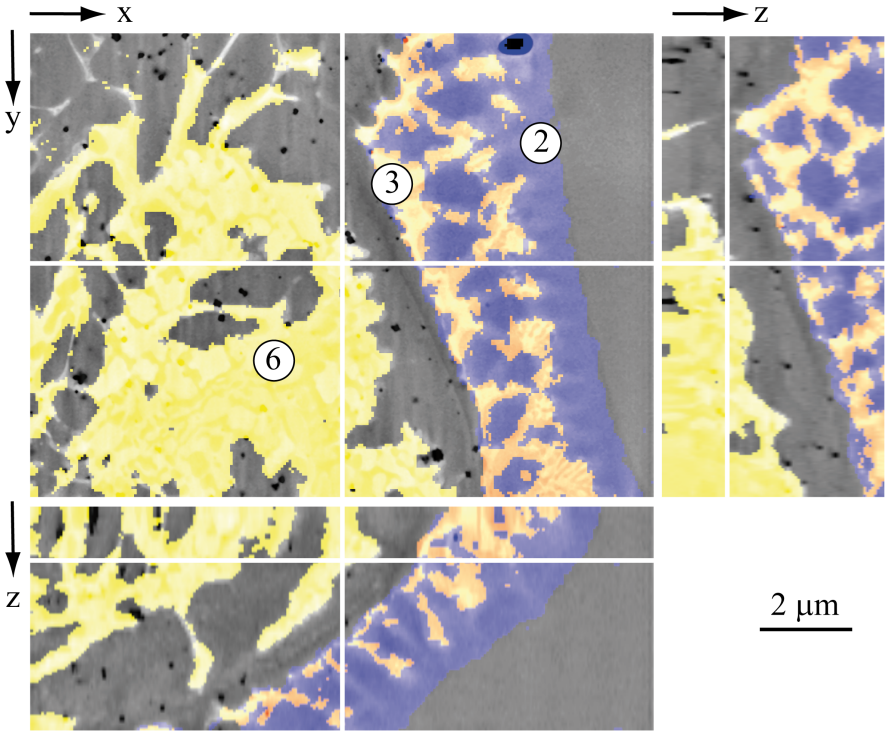

(b) Domains 2, 3, and 6.

Figure 7.2: Orthogonal views through the stack of SE images with composition domains superimposed (1 to 6). The thresholds domains are defined in figure 7.1(b). The white lines show the position of the other orthogonal views.

Enhanced quantification

The fine structure of domain 6 is hardly resolved by the segmentation technique, because the EDS maps have an insufficient contrast or spatial resolution in this region. As an improvement of contrast is obtained with the enhanced quantification described in the previous chapter, the stack quantified with this technique is used in this subsection[5]. The threshold domains 5 and 6 defined in figure 7.1(b) are used as a starting point. As indicated by a red arrow in figure 7.3(a), the shared boundary is moved toward less Ti (downwards) to obtain a new domain 6a shown in figure 7.3(b). Similarities are observed between this new domain and the clearest contrast of the SE images. This contrast of the SE images corresponds to the γ-(Fe,Ni) phase, and the darker contrast corresponds to the Fe_2Ti phase.

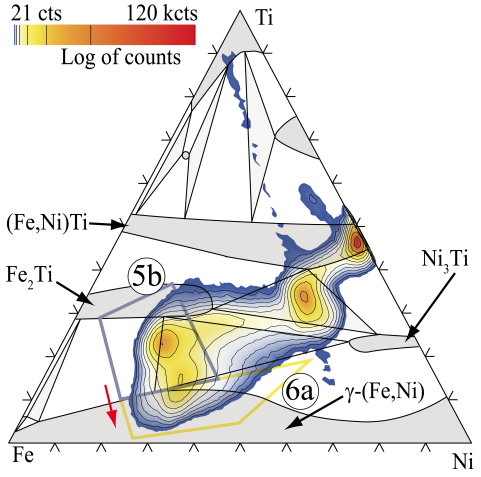

(a) Ternary histograms of the compositions displayed in the Fe-Ni-Ti Gibbs simplex. The histogram is superimposed with a 1000°C-isothermal section of the Fe-Ni-Ti phase diagram [45]. The labeled polygons give the threshold domain used for segmentation.

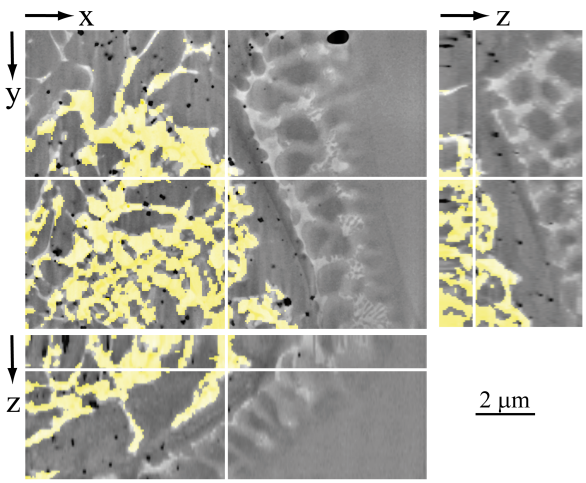

(b) Domain 6a: orthogonal views through the stack of SE images with the domain superimposed. The white lines show the position of the other orthogonal view.

Figure 7.3: Refinement of the composition domains 5 and 6 using the enhanced quantified stack.

7.2 Segmentation refinement with SE images

A second segmentation step is applied considering SE images in order to go beyond the resolution limits of EDS maps. The two regions with a fine microstructure are treated this way: the composition domain 6, and the domains 2 and 3. These regions are isolated from the rest of the SE images using the composition domains of figure 7.2(b) (shown also in figure 7.4(a)) as masks. Applying then a threshold on the grey level of the masked SE images, these regions are finely segmented into two sub-domains shown in figure 7.4(b). A very good example of the

[5] In section 6.3.4, the domain 6 with a composition close to γ-(Fe,Ni) was used to show the gain obtained with the enhanced quantification.

higher resolution so-achieved is provided by the bottom region of domain 3 in the x-y orthogonal slice of figure 7.4(a). In this figure, the orange domain nearly forms an uniform zone. While, in figure 7.4(b), the blue and orange domains (2' and 3') clearly form a system of lamellae[6]. Similarly, domain 6 which is a uniform pink region in figure 7.4(a) is composed of a yellow and a pink sub-domains in figure 7.4(b). These sub-domains 6'a and 6'b correspond to γ-(Fe,Ni) and Fe_2Ti respectively.

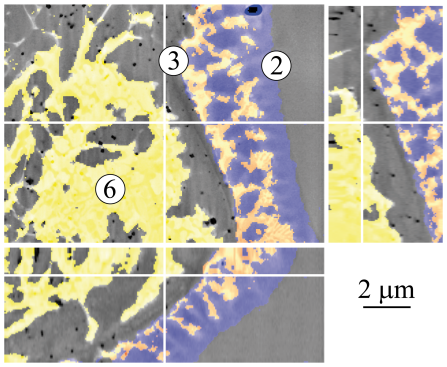

(a) Domains 2, 3, and 6: see figure 7.2(b).

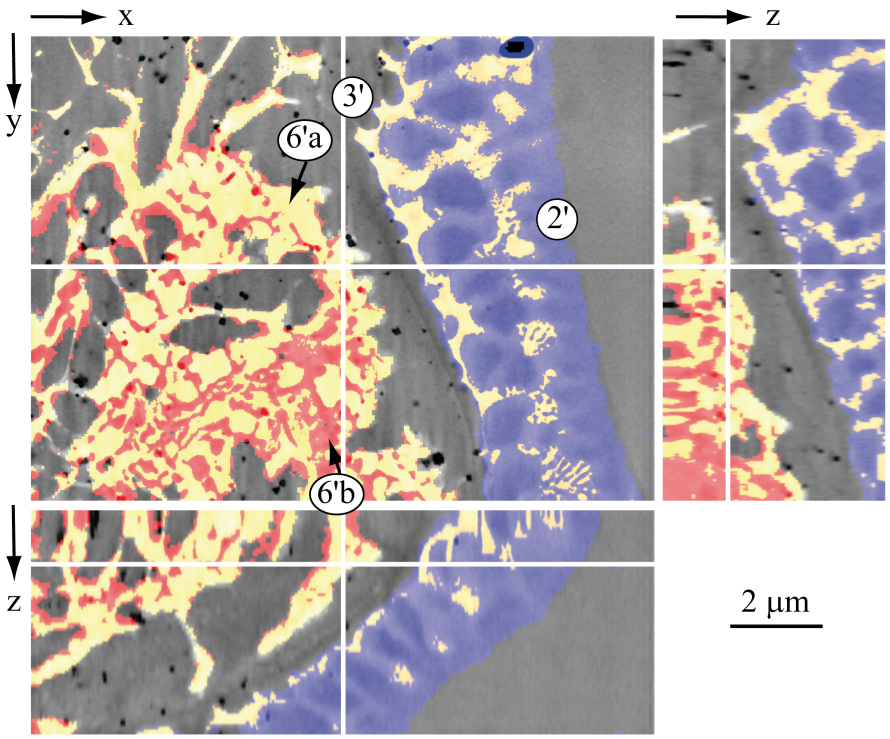

(b) Refined domains 2', 3', 6'a and 6'b.

Figure 7.4: Comparison between domains and refined domains: orthogonal views through the stack of SE images with domains superimposed. The white lines show the position of the other orthogonal views.

[6]This zone is supposed to be a eutectic made of γ-(Fe,Ni)Ti and Ni_3Ti.

The 7 refined domains (figure 7.2(a) and figure 7.4(b)) are used to reconstruct the 7 surfaces of the 3D visualisation of figure 7.5. A careful analysis of this figure reveals the various phases with their different morphologies. The sequence of appearance of these phases has been correlated with the ternary Fe-Ni-Ti phase diagram and the solidification process implied during the laser welding [63]. In a further step, the reconstruction can be extended with the two other phases not considered here: the TiC particles that have a dark contrast on SE images and the TiO particles that are identified with the oxygen elemental map.

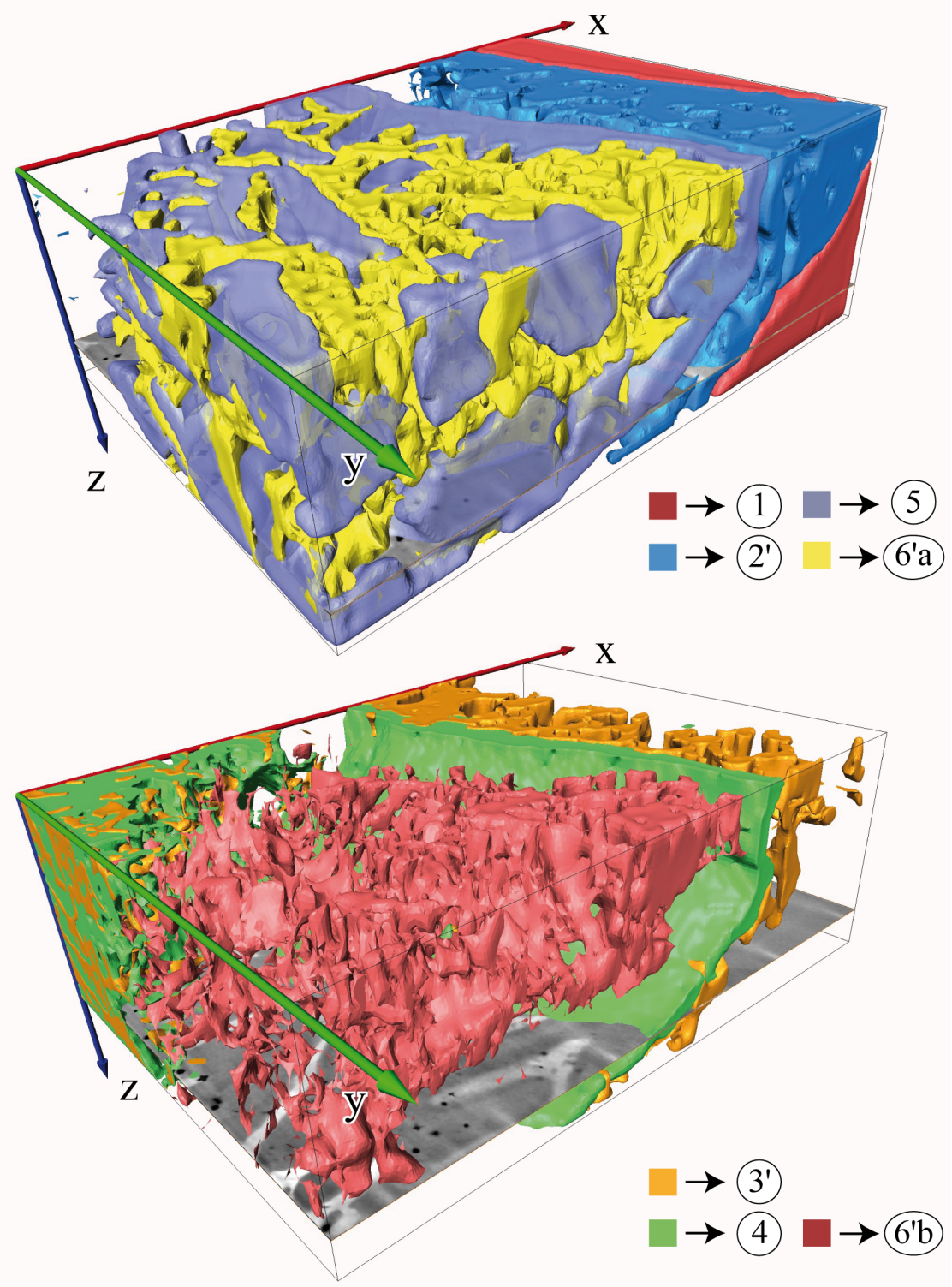

Figure 7.5: Surface reconstruction of the seven domains of figure 7.2 and figure 7.4. The surfaces of the domain correspond to the phases as follows: surface 1 → unmelted NiTi wire; surface 2 → (Fe,Ni)Ti, surface 3 → Ni_3Ti; surface 4, 5, and 6'b → Fe_2Ti with different morphologies; and surface 6'a → γ-(Fe,Ni).

7.3 Summary

Figure 7.6 shows a flow chart that summarizes the segmentation technique. First a ternary histogram is generated from the elemental maps. Chemically similar regions are isolated with threshold domains defined on the ternary histogram. Care is taken that each voxels is attributed to one single phase. The boundaries of the threshold domains are finely tuned with the help of domain visualisation overlaying SE images. A further refinement into sub-domains is obtained applying thresholds on the SE images. With this segmentation technique applied on the stack acquired on the NiTi-SS sample, 7 different phases were successfully identified with features otherwise unresolved in EDS maps.

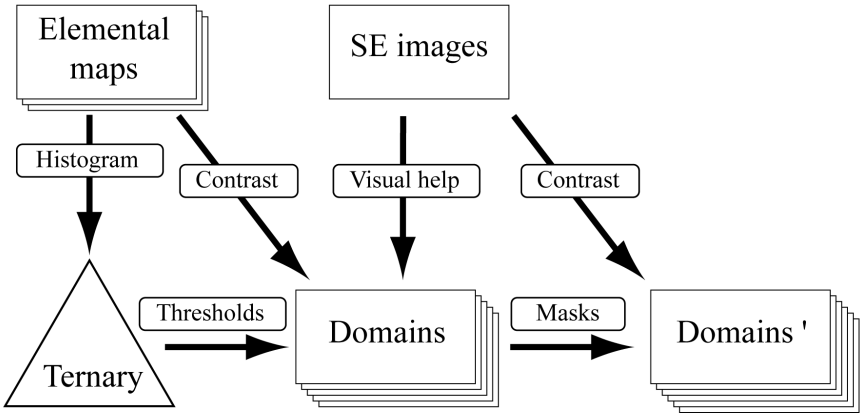

Figure 7.6: Flowchart of the segmentation technique. First row: the input stacks. Second row: the segmentation steps. Arrows: the processes. "Domains '" are the refined domains.

The accuracy of the segmentation depends on the quality of the EDS maps: the stack quantified with the enhanced method (see chapter 6) was used to better relate the contrast of the SE images with a phase of a fine morphology. However, since the SE images provide a ground with a high spatial resolution, this technique can provide good results with stack processed with simple procedure, such as maps of intensities of X-ray line with a simple noise filter.

8 Conclusion

The goal of this work is to investigate the limitations of EDS microanalysis in three dimensions and to develop appropriate solutions with a focus on data processing techniques. As discussed in chapter 4, 5, 6, and 7 respectively, the four studied limitations are:

1. The parasite X-rays artefact: spurious X-rays that are generated on the surrounding trench walls that reach the detector.
2. The noise in the spectra: the acquisition time per spectrum is short due to the limited time to record the numerous spectra for a 3D data set.
3. The compositional accuracy when the analysed feature is smaller than the X-ray emission volume: this volume is large because the required accelerating voltage needs to be high enough to excite the desired characteristic X-ray lines.
4. The spatial resolution: the resolution is limited by the large X-ray emission volume.

Solutions to these four limitations have been developed and demonstrated in the corresponding chapter. Here, a synthesis and an outlook will be provided. The suggested solution for the first limitation is treated independently as it is not part of the post-processing procedure formed by the three later solutions.

8.1 Synthesis

The parasite X-rays artefact depends on the sample-preparation geometry. This artefact is observed with the U-pattern geometry, but is not observed with the block lift-out geometry suggested by Schaffer [17]. Very often, however, the simpler and faster U-pattern geometry is preferred, therefore the artefact was further studied for this geometry in chapter 4. An element present in the surrounding trenches, but not in the milled surface, has served as a parasite X-ray indicator. Its variations in function of the position on the milled surface were explained considering the geometry of the surrounding trenches. The amount of parasite X-rays can be reduced either by lowering the accelerating voltage, or by milling trenches facing the detector wider.

The developed solutions to the later three limitations are three processing techniques, respectively: a noise reduction technique (PCA and 3D median), an enhanced quantification procedure, and a segmentation technique. Grouped together, they form a full post-processing procedure, from the raw data to the final 3D visualisation, as shown in figure 8.1. Each solution was independently summarized at the end of the corresponding chapter. In this chapter, the three procedures are discussed together in paragraphs focused on different aspects.

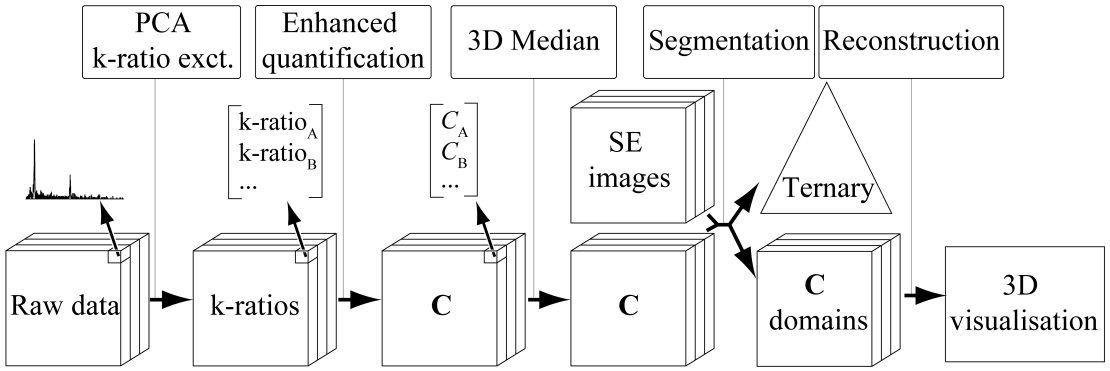

Figure 8.1: Flowchart of the full procedure. "k-ratio exct." stands for k-ratio extraction. **C** is the composition. The content of one voxel (top right corner) is illustrated for three first stacks.

Implementation: Noise reduction is applied at two stages of the procedure as shown in figure 8.1. The raw spectra are smoothed with principal component analysis (PCA), a technique based on multivariate statistics applied to all spectra. After the quantification, the compositional maps are smoothed with a 3D median filter. With the enhanced quantification, the influence of the neighbouring voxels is corrected applying recursively a complex quantification technique (thin-film quantification). Applied on the smoothed compositional maps, the segmentation technique is divided in two steps. The volume is first segmented into composition domains defining thresholds on a ternary composition histogram. The domains are then further refined with the contrast of the SE images.

Context: The PCA is used as a noise filter to improve quantification, and this has been reported only few times for EDS: Parish discussed it for STEM/EDS [39]. Median filter is a classical smoothing filter that preserves edges [33]. No technique to enhance the quantification of 3D EDS data has been reported, but the thin-film quantification, on which the enhanced quantification is based, is a well-developed technique chosen among others [60]. Defining the thresholds on a composition histogram was suggested by Bright and Newbury for 2D EDS maps [59]. Adapting this technique to 3D, two aspects of the presented segmentation technique are new: the careful definition of threshold values with a constraint to have all voxels attributed, and the refinement step with the use of SE images.

Testing: A real-case sample was selected to test the processing techniques. The sample is produced welding wires of nickel-titanium (NiTi) and stainless steel (SS) by laser. The 3D EDS

data were acquired at the interface between the welded region and the unmelted NiTi wire. As this last wire has a constant composition, the variations in sets of spectra acquired of this region were used to measure the noise level. Regions of the analysed volume show a microstructure size larger than the volume of X-ray emission, where as some other regions show smaller features. The regions with finer microstructure were used to test the compositional accuracy and the spatial resolution. To evaluate the actual improvement, the SE images that have higher spatial resolution were used as a spatial reference, and an isothermal section of the Fe-Ni-Ti phase diagram was used as a compositional reference.

Limitations: The PCA can introduce artefacts if the signal-to-noise ratio of the considered peaks is not high enough. In the demonstrated case, the artefact results in an overestimation of the minor elements. The median filter tends to remove small spherical features. To preserve them, a balance needs to be found with the smoothing effect through the careful adjustment of the kernel size. The enhanced quantification can introduce noise in the form of oscillations along the z axis. A mean filter along this direction can be applied to reduce this artefact. The segmentation technique fails if the contrast of the SEM images are not correlated to changes in composition.

Gain: With both PCA and 3D median filter, the noise is decreased and features that were unseen are revealed. The PCA has shown to efficiently reduce the increase of noise induced by the background subtraction. Noise reduction has shown to be important for the enhanced quantification that needs data with a low noise level. The enhanced quantification reveals even more the small features, and their enhanced composition is closer to the predicted one. With the segmentation, all voxels are attributed to a composition domain related to a phase of the phase diagram. A spatial resolution close to the SE images can be reached, allowing fine microstructure details to be identified.

For the NiTi-SS sample with its complex microstructure and complex phase composition, the 3D EDS microanalysis has shown to be a valuable characterisation technique. As presented in an article that is under review process, a careful analysis of the different phases and morphologies was undertaken using the 3D visualisation of the domains obtained with the segmentation technique [63]. With this analysis, the sequence of phase formation has successfully been correlated to the phase diagram and the involved solidification process.

Applicability: As stressed by Parish, the PCA as a noise filter should not be used without a careful inspection of the principal components and the reconstructed spectra[1]. The enhanced quantification has only been tested on two stacks of data from two different samples. More investigations and probably more improvements are needed for the technique to be generally applicable to any kinds of samples. The segmentation technique is robust and can be used with any stack of data with any pre-processing[2].

[1] Implemented by G. Lucas, the PCA version used in this work will be freely available on request as a plugin for DigitalMicrograph™.

[2] A version of the segmentation technique, coupled with 3D visualisation, is currently under a joint development with Carl Zeiss. It will be available as a plugin for Avizo® fire 7.0 (VSG).

8.2 Outlook

The present work has shown now that different techniques can be combined in order to improve EDS elemental analysis in 3D. Nevertheless there is still some potential for improvement. The neighbourhood smoothing filter, such as median filter, can be improved if the kernel size changes in function of the local properties of the image (*e.g.* the kernel is smaller when close to an edge). The noise can thus be reduced more efficiently preserving the edges (the anisotropic diffusion filter is based on this principle [34]). To make the PCA a more routine technique for noise reduction, a more systematic study of the artefacts is required in order to predict the minimum signal-to-noise ratio needed for an artefact-free reconstruction. The different potential improvements for the enhanced quantification were detailed in section 6.4: for example, the layer system for the thin-film quantification can be better defined, and the test for homogeneity needs to be improved. In order to reduce the oscillation problem, an iterative approach over the whole quantification could be used. For the segmentation, the different domains could be more accurately segmented by measuring the average distance between the domain border and the grey level boundary in the SE images.

All the three processing techniques to overcome the different problems can be improved independently, but the obtained global improvement will remain limited. The approach used during this thesis was to treat these problems with the different techniques individually. A global approach can be envisaged in which all problems (the noise and the large volume of X-ray emission) could be treated at once using both EDS maps and SEM images. In this global approach, we have to solve an inverse problem, *i.e.* to convert physical measurements into meaningful information about the observed physical object. To solve this inverse problem, an objective function that takes into account the noise and the image degradation (*e.g.* convolution) can be defined. The original image is then recovered optimizing this function through an iterative procedure, which can be subject to constraints involving noise statistic and edge preservation. Various approaches to this problem have been developed such as "$\ell_2 - \ell_0$ regularization" [64]. One advantage of this technique is that some a-priori knowledge, such as the SEM images, can be used as constraint. Another approach consists in considering the X-ray emission volume, the point spread function (PSF), as unknown. With techniques based on blind source separation, such as non-negative matrix factorisation technique (NNMF) [65], the different composition-dependent PSFs and the compositional maps can be simultaneously recovered. Both of these approaches have the advantage of being robust to noise as they are global unlike the enhanced quantification.

Bibliography

[1] Castaing, R. *Application des sondes électroniques à une méthode d'analyse ponctuelle chimique et cristallographique*. PhD thesis, Université de Paris, Paris, (1951).

[2] Schaffer, M. *Development of 3D Elemental Analysis using Focused Ion Beam Microscopy and Enery Dispersive X-ray Spectrometry*. PhD thesis, TU Graz, Graz, April (2008).

[3] Kotula, P., Keenan, M., and Michael, J. *Microscopy and Microanalysis* **12**(1), 36–48 (2006).

[4] Goldstein, J., Newbury, D. E., Echlin, P., Joy, D. C., Lyman, C. E., Lifshin, E., and Sawyer, L. *Scanning Electron Microscopy and X-ray Microanalysis*. Springer, 3rd edition, (2003).

[5] Bethe, H. *Annals of Physics.* **5**, 325 (1930).

[6] Kanaya, K. and Okayama, S. *Journal of Physics D: Applied Physics* **5**(1), 43–58 (1972).

[7] Anderson, C. A. and Hasler, M. In *Proccedings of the 4th International Conference on X-ray otpics and Microanalysis,* Castaing, R., Deschamps, P., and Philibert, J., editors, 310. Parishermann edition (1966).

[8] Joy, D. C. *Monte Carlo modeling for electron microscopy and microanalysis*. Oxford University Press US, (1995).

[9] Drouin, D., Couture, A., Joly, D., Tastet, X., Aimez, V., and Gauvin, R. *Scanning* **29**(3), 92–101 (2007).

[10] Ritchie, N. W. *Microscopy and Microanalysis* **15**(05), 454–468 (2009).

[11] Pouchou, J. and Pichoir, F. *Recherche Aerospatiale (English Edition)* (3), 13–38 (1984).

[12] Giannuzzi, L. A. and Stevie, F. A. *Introduction to Focused Ion Beams*. Springer, (2005).

[13] Strüder, L., Lechner, P., and Leutenegger, P. *Naturwissenschaften* **85**(11), 539–543 (1998).

[14] Collins, C., Holland, J., Burgess, S., Statham, P., and Rowlands, N. *Microscopy and Microanalysis* **15**(Supplement S2), 230–231 (2009).

[15] Schaffer, M., Wagner, J., Schröttner, H., and Schmied, M. *Praktische Metallographie/Practical Metallography* **44**(5), 248–250 (2007).

[16] Schaffer, M., Wagner, J., Schaffer, B., Schmied, M., and Mulders, H. *Ultramicroscopy* **107**(8), 587–597 (2007).

[17] Schaffer, M. and Wagner, J. *Microchimica Acta* **161**(3-4), 421–425 (2008).

[18] Lasagni, F., Lasagni, A., Holzapfel, C., Mücklich, F., and Degischer, H. P. *Advanced Engineering Materials* **8**(8), 719–723 August (2006).

[19] Lasagni, F., Lasagni, A., Marks, E., Holzapfel, C., Mücklich, F., and Degischer, H. *Acta Materialia* **55**(11), 3875–3882 (2007).

[20] Lasagni, F., Lasagni, A., Engstler, M., Degischer, H., and Mücklich, F. *Advanced Engineering Materials* **10**(1-2), 62–66 (2008).

[21] Scott, K. and Ritchie, N. *Journal of Microscopy* **233**(2), 331–339 (2009).

[22] Scott, K. *Journal of Microscopy* **242**(1), 86–93 April (2011).

[23] Ziebold, T. and Ogilvie, R. *Analytical Chemistry* **36**, 322 (1964).

[24] Ancey, M., Bastenaire, F., and Tixier, R. *Journal of Physics D: Applied Physics* **10**(6), 817–830 (1977).

[25] Lifshin, E., Doganaksoy, N., Sirois, J., and Gauvin, R. *Microscopy and Microanalysis* **4**(06), 598–604 (1998).

[26] Xu, X. *Journal of Vacuum Science & Technology B: Microelectronics and Nanometer Structures* **10**(6), 2675 (1992).

[27] Phaneuf, M. F. In *Introduction to Focused Ion Beams,* Giannuzzi, L. A. and Stevie, F. A., editors, 143. Springer (2005).

[28] Kotula, P., Keenan, M., and Michael, J. *Microscopy and Microanalysis* **9**(1), 1–17 (2003).

[29] Kotula, P. G. and Sorensen, N. R. *Journal of Microscopy* **63**, 41–43 July (2011).

[30] Statham, P. *Journal of Research of the National Institute of Standards and Technology* **107**(6), 531–546 (2002).

[31] Bastin, G. F., Dijkstra, J. M., and Heijligers, H. J. M. *X-Ray Spectrometry* **27**(1), 3–10 February (1998).

[32] Pouchou, J. and Pichoir, F. *Recherche Aerospatiale (English Edition)* (5), 47–65 (1984).

[33] Russ, J. C. *The Image Processing Handbook*. CRC Press, 5th edition, (2007).

[34] Ohser, J. and Schladitz, K. *3D Images of Materials Structures: Processing and Analysis*. Wiley VCH, (2009).

[35] Thévenaz, P., Ruttimann, U., and Unser, M. *IEEE Transactions on Image Processing* **7**(1), 27–41 (1998).

[36] Friel, J. and Lyman, C. *Microscopy and Microanalysis* **12**(1), 2–25 (2006).

[37] Malinowski, E. R. *Factor Analysis in Chemistry*. John Wiley & Sons Inc, 3rd edition, March (2002).

[38] Keenan, M. and Kotula, P. *Surface and Interface Analysis* **36**(3), 203–212 (2004).

[39] Parish, C. and Brewer, L. *Microscopy and Microanalysis* **16**(3), 259–272 (2010).

[40] Keenan, M. *Surface and Interface Analysis* **41**(2), 79–87 (2009).

[41] Friedli, J. *Interfacial Energy Anisotropy and growth Morphologies in Aluminium-Zinc Alloys*. PhD thesis, EPFL, Lausanne, September (2011).

[42] Vannod, J. *Laser Welding of Nickel-Titanium and Stainless Steel Wires: Processing, Metallurgy and Properties*. PhD thesis, EPFL, Lausanne, September (2011).

[43] Massalski, T. B. In *Binary alloy phase diagrams: Volume 1 (Ac-Au to Fe-Rh)*, volume 1, 184–188. American Society for Metals, Ohio (1986).

[44] Vannod, J., Bornert, M., Bidaux, J., Bataillard, L., Karimi, A., Drezet, J., Rappaz, M., and Hessler-Wyser, A. *Acta Materialia* **59**(17), 6538–6546 (2011).

[45] Cacciamani, G., De Keyzer, J., Ferro, R., Klotz, U., Lacaze, J., and Wollants, P. *Intermetallics* **14**(10-11), 1312–1325 (2006).

[46] Kirkaldy, J. S. and Brown, L. C. *Canadian Metallurgical Quarterly* **2**, 89–117 (1963).

[47] Uglietti, D., Abächerli, V., Cantoni, M., and Flükiger, R. *Applied Superconductivity, IEEE Transactions on* **17**(2), 2615 –2618 June (2007).

[48] Duerig, T., Pelton, A., and Trepanier, C. *Nitinol.* , To be published (2012).

[49] Alvisi, M., Blome, M., Griepentrog, M., Hodoroaba, V., Karduck, P., Mostert, M., Nacucchi, M., Procop, M., Rohde, M., Scholze, F., Statham, P., Terborg, R., and Thiot, J. *Microscopy and Microanalysis* **12**(5), 406–415 (2006).

[50] Cantoni, M., Genoud, C., Hébert, C., and Knott, G. *Microscopy and Analysis* **24**(4), 13–16 (2010).

[51] Statham, P. *Analytical Chemistry* **49**(14), 2149–2154 (1977).

[52] Lucas, G., Burdet, P., Cantoni, M., and Hébert, C. *To be published* (2012).

[53] Bastin, G. and Heijligers, H. *X-Ray Spectrometry* **29**(3), 212–238 (2000).

[54] Statham, P., Llovet, X., and Duncumb, P. In *IOP Conference Series: Materials Science and Engineering*, volume 32, (2012).

[55] Cantoni, M., Scheuerlein, C., Pfirter, P., De Borman, F., Rossen, J., Arnau, G., Oberli, L., and Lee, P. *Journal of Physics: Conference Series* **234**(PART 2) (2010).

[56] Müller, K. *Microelectronic Engineering* **11**(1-4), 443–447 (1990).

[57] Cliff, G. and Lorimer, G. *Journal of Microscopy* **103**(2), 203–207 (1975).

[58] Rudin, L., Osher, S., and Fatemi, E. *Physica D: Nonlinear Phenomena* **60**(1-4), 259–268 (1992).

[59] Bright, D. and Newbury, D. *Analytical Chemistry* **63**(4), 243A–250A (1991).

[60] Pouchou, J. *Mikrochimica Acta* **138-139**(138/3-4,139/1-4), 133–152 (2002).

[61] Bastin, G. and Heijligers, H. *X-Ray Spectrometry* **29**(5), 373–397 (2000).

[62] Statham, P. J. *IOP Conference Series: Materials Science and Engineering* **7**, 012027 February (2010).

[63] Burdet, P., Vannod, J., Hessler-Wyser, A., Rappaz, M., and Cantoni, M. *To be published* (2012).

[64] Chouzenoux, E., Pesquet, J., Talbot, H., and Jezierska, A. In *Proceedings - International Conference on Image Processing, ICIP*, 2717–2720, (2011).

[65] Lee, D. and Seung, H. *Nature* **401**(6755), 788–791 (1999).

A Notation

Latin Characters

A, A_1, A_2	Element index
a	Constant for the calculation of the uncertainty on the composition
$\mathbf{C}$	Sample concentration
$\overline{\mathbf{C}}_{i,j+n}$	Concentration compensated for tilt at $j+n$ in z and i in y
C_A, C_{A_1}, C_{A_2}	Content of element A
$\mathbf{D}$	Data matrix
D_A	Electron distribution in a pure element A
$\overline{D}(m,n)$	Weighted factor at n in z and m in y
d_p	Electron probe diameter
e	Index of energy channel in a spectrum
E_0	Primary electron energy
E_c	Critical ionization energy
f	Recurrence relation
i, j	Voxel index for y and z axes
I_0	Primary X-ray intensity
I_B	Measured X-ray intensity of the background
I_{corr}	Measured X-ray intensity corrected for the background
I_e	Number of X-ray in an energy channel e
I_{emit}	Emitted X-ray intensity
I_{raw}	Measured X-ray intensity not corrected for the background
I_{std}	Measured X-ray intensity on a microanalysis standard
i_p	Electron probe current

k-ratio	Ratio between measured intensity and intensity of a standard
L_{int}	Channel width used to measure the intensity
L_{up}, L_{low}	Channel widths used to defined the kernel of the top hat filter
m, n	Index in y and z relative to i and j
n	Number of spectra in a set
N, N_1, N_2, N_3, N_i	A set of variables
P	Loading matrix
p-value	Probability of a hypothesis in a χ^2 test
Q	Cross section for inner shell ionization
R	Electron range
R_x	X-ray range
$r, r_{min,A1}, r_{max,A2}$	Rotation factor for the boundary of a threshold domain
r_{max}	Deepest voxel from which X-rays originate
$T, T_{min,A}, T_{max,A}$	Threshold value of a composition domain
t	Thickness
T	Score matrix
U	Overvoltage
V_0	Accelerating voltage
Z, A, F	Correction factor for matrix effects
Z', A', F'	Correction factor for heterogeneous microvolume

Greek Characters

α	Angle between SEM and FIB columns
β	Elevation angle
γ	Azimuth angle
ϵ_c	Limit to test concentration similarity
μ/ρ	Mass absorption coefficient
ρ	Density
σ	Standard deviation
$\phi(\rho z)$	Depth distribution of generated X-ray
χ	Absorption depth
ψ	Take-off angle

B Processing steps

The two following figures show the orthogonal views and the ternary histograms of the NiTi-SS quantified stack. The orthogonal views of the SE images are shown at the top. At the middle, the orthogonal views show the concentrations of the quantified stack scaled by colour codes. To obtain the ternary histogram at the bottom, the Fe-, Ni-, Ti-concentrations measured at each voxel of the quantified 3D stacks are reported in a ternary Gibbs simplex, with a logarithmic scale given by a colour code. These ternary histograms are overlaid on a 1000°C-isothermal section of the Fe-Ni-Ti phase diagram [45].

Figure B.1 is the complement of figure 5.6 in which the effects of the different steps of the smoothing procedure are qualitatively shown (see section 5.3.2).

Figure B.2 is the complement of figure 6.18 in which the effects of the enhanced quantification are qualitatively shown (see section 6.3.4).

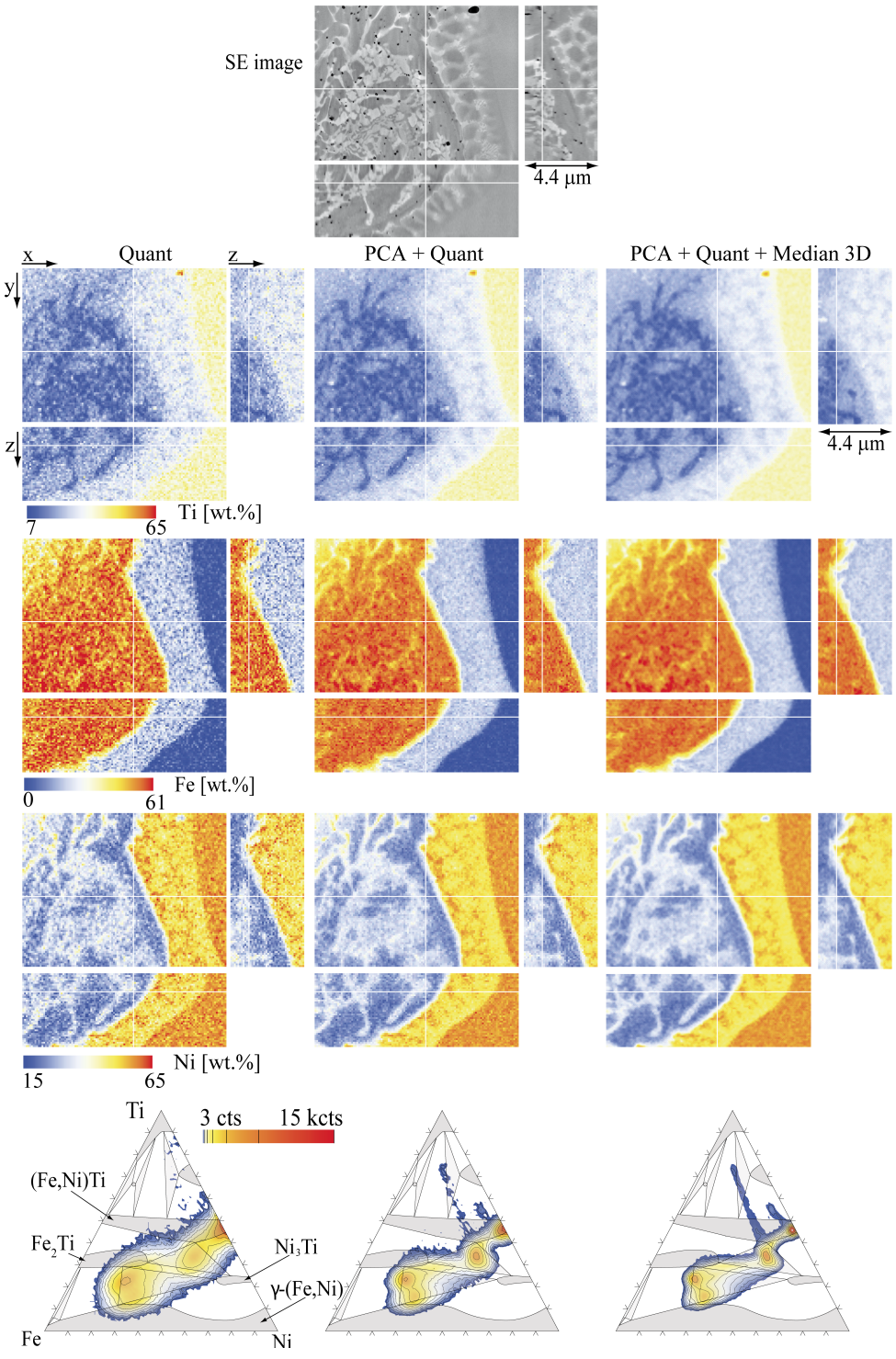

Figure B.1: Orthogonal views (top) and ternary histograms (bottom) of the NiTi-SS quantified stack: comparison between the different steps of the smoothing procedure (see section 5.2). The concentrations of the quantified stack are scaled by colour codes. The white lines show the position of the other orthogonal views. The histograms are scaled by a colour code and iso-contours, and a ternary phase diagram cut at 1000°C is superimposed [45].

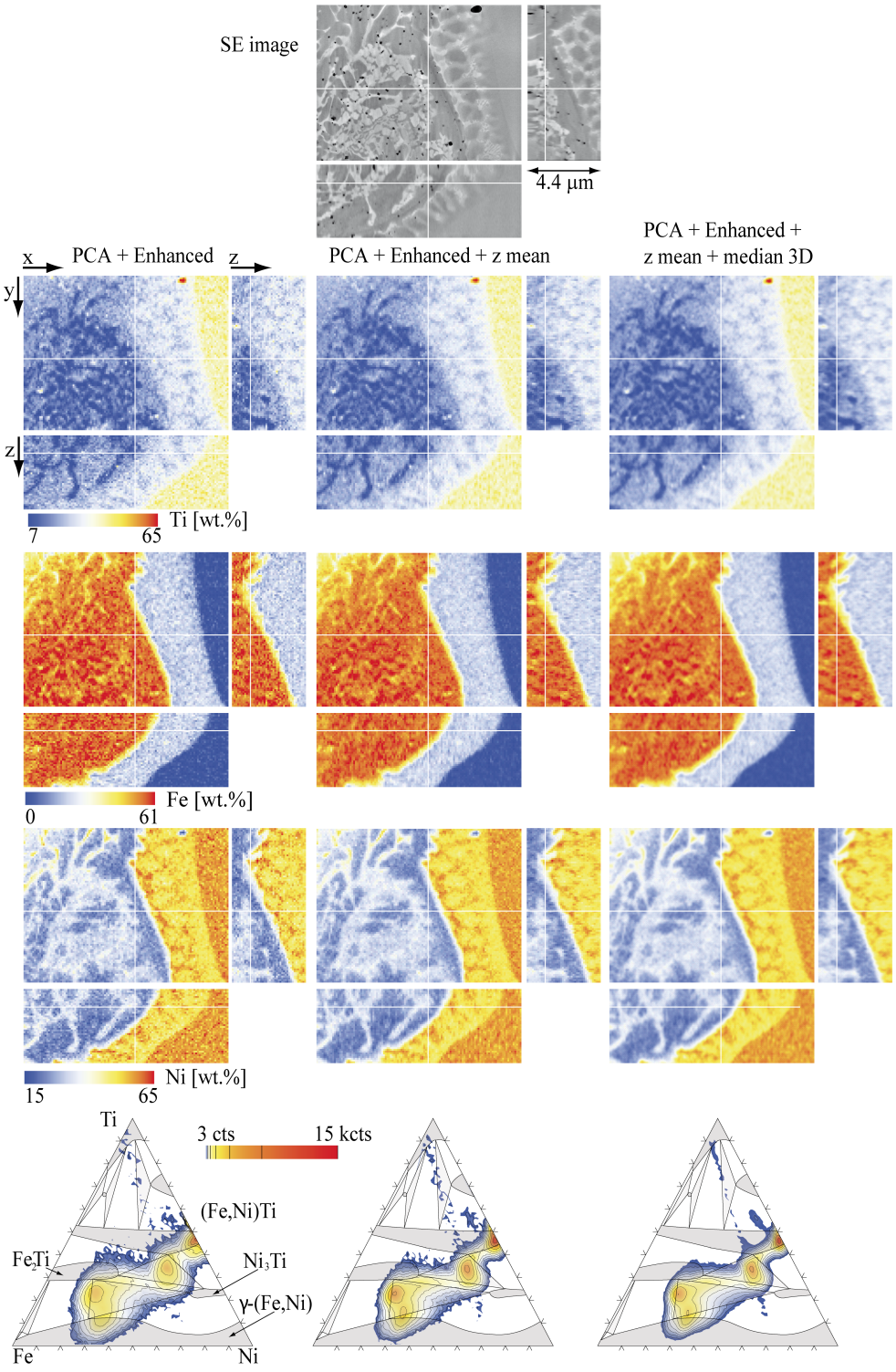

Figure B.2: Orthogonal views (top) and ternary histograms (bottom) of the NiTi-SS stack quantified with the enhanced technique: comparison between different noise-reduction filter (see section 6.3.4). The concentrations of the quantified stack are scaled by colour codes. The white lines show the position of the other orthogonal views. The histograms are scaled by a colour code and iso-contours, and a ternary phase diagram cut at 1000°C is superimposed [45].

C Publications

Publications in refereed Journals

M.A. Salgado-Ordorica, P. Burdet, M. Cantoni, and M. Rappaz,
Study of the twinned dendrite tip shape II: experimental assessment
Acta Materialia **59**(13), 5085-5091 (2011)

P. Burdet, J. Vannod, A. Hessler-Wyser, M. Rappaz, and C. Cantoni,
3D chemical analysis of laser welded NiTi:staineless steel wires using a dual-beam FIB
Under review process (2012)

G. Lucas, P. Burdet, M. Cantoni, and C. Hébert,
Multivariate statistical analysis tool for the segmentation of hyperspectral images
To be published (2012)

Awards

1^{th} prize of the young scientist's contribution
EMAS, Anger/France, 15-19. May 2011

Best oral presentation of the 5^{th} EDMX research day.
EDMX research day (EPFL doctoral school), EPFL/Lausanne, 17. March 2011

Oral Presentations

3D EDX Microanalysis by FIB-SEM: Influence of Sample Preparation
MC, Graz/Austria, 30. August- 4. September 2009

3D EDX Microanalysis by FIB-SEM: Particularity
EDX workshop, EPFL/Lausanne, 7. April 2010

3D EDX Microanalysis by FIB-SEM: Algorithm for elemental quantification enhancement
EMRS, Strasbourg/France, 7-11. September 2010

3D EDX Microanalysis by FIB-SEM: Algorithm for elemental quantification enhancement
FIB workshop, Wien/Austria, 28-29. June 2010

3D EDX Microanalysis by FIB-SEM: Algorithm for elemental quantification enhancement
CAZAC, Lyon/France, 1-2. July 2010

Analytical SEM: EDX and FIB
CCMX Summer School, EPFL/Lausanne, 25-27. August 2010

3D EDX Microanalysis by FIB-SEM : Comprehensive characterization of complex metal alloy phases.
FIB workshop, Zurich/Switzerland, 27-30. June 2011

3D EDX Microanalysis by FIB-SEM : Algorithm for elemental quantification enhancement.
M&M, Nashville TN/United-States, 7-11. August 2011

3D EDX Microanalysis by FIB-SEM : Algorithm for elemental quantification enhancement.
MM, 3D workshop, Saarbrücken/Germany, 1-4. November 2011

Microanalyse en 3D par MEB-FIB : Limitations, Potentiel et Perspectives.
GN-MEBA, Journée pédagogique, Paris/France, 1-2. December 2011

3D EDX Microanalysis by FIB-SEM : Algorithm for elemental quantification enhancement.
SSOM, 3D workshop, Diablerets/Switzerland, 5-8. March 2012

3D EDX Microanalysis by FIB-SEM : Algorithm for elemental quantification enhancement.
CAZAC, EPFL/Lausanne/Switzerland, 12-14. June 2012

3D EDX Microanalysis by FIB-SEM : Algorithm for elemental quantification enhancement.
M&M, Phoenix Ar/United-States, 29. July - 02. August 2012

Poster Presentations

Microanalysis 3D FIB/EDS : Influence of interaction volume on interface detection.
SSOM, 3D workshop, Interlaken/Switzerland, 12-15. July 2009

Microanalysis 3D FIB/EDS : Influence of interaction volume on interface detection.
EDMX research day (EPFL doctoral school), EPFL/Lausanne, 15. October 2009

3D EDX Microanalysis by FIB-SEM : Algorithm for elemental quantification enhancement.
EMAS, Anger/France, 15-19. May 2011

Pierre Burdet

EPFL-CIME
MXC-136, Station 12
1015 Lausanne, Switzerland
Tel: +41 21 6934437
Date of Birth: 1st August 1984

Rue de la Borde 27
1018 Lausanne, Switzerland
Mobile : +41 79 3178482
pierre.burdet@a3.epfl.ch
Nationality: Swiss

Education

2008-present — EPFL, Lausanne, Switzerland

Ph.D. degree in Material Science

Title: "*3D EDS Microanalysis by FIB/SEM, Improved Data Processing*"
Supervisors: Prof. C. Hébert and Dr. M. Cantoni
This work comprises developments of experimental and processing. The thesis was financed and supported by Carl Zeiss.

2003-2008 — EPFL, Lausanne, Switzerland

Master degree in Materials Science and Engineering

Dissertation Project: *"Reliability of Organic Field Effect Transistor: Atmosphere Effect."*
Main fields studied comprise; Processing, Structure, Properties and Applications of Structural and Functional Materials.

2000-2003 — CESSNOV, Yverdon, Switzerland

"Maturité fédérale" degree

Other Research Experience

2007-2008
Undergraduate Research Assistant — EPFL-CIME, Lausanne, Switzerland
I worked under the supervision of Prof. P. Stadelmann, characterising materials by TEM for various projects. Two publications resulted from these projects (see co-author publication).

2008-present
Research Assistant — EPFL-CIME, Lausanne, Switzerland

- In addition to the dissertation work, I participated in different projects using SEM/EDS and FIB/SEM. A publication resulted from one project (see co-author publication).
- I have been involved with the supervision of undergraduates in practical classes and EM practical formation. I had some experiences of teaching, replacing Dr. M. Cantoni for doctoral classes and in one summer school .

Research Techniques

From my PhD, I'm qualified in SEM/EDS and FIB/SEM nanotomography. From my undergraduate work, I'm qualified in imaging TEM, STEM/EDS, diffraction, and mechanical TEM-sample preparation.

Other Experiences

I have had various student projects: projectionist in cinema, coach for young students, administrative work, and museum guide. The last job helped me to develop my oral-presentation skills.

Skills

IT

As the focus of my thesis is image processing, I have learned different computing methods and developed my own scripts. My main tools were Mathematica and C++, and some others: Jython, Vb6, Java, Illustrator, ImageJ, Latex, and Microsoft Office.

Languages

Extensive knowledge of English, I completed one year of the Master of Material Science at KTH in Stockholm with all classes in English. Good speaking and writing skills.
Good writing skills and basic speaking skills in German.

Interests & Achievements

- 1st prize of the young scientist's contribution at EMAS, Anger France 2011.
- President of the Material Student Association, EPFL 2005-2006.
- Councillor of sailing at "La Matelote", Yverdon 2003-2011.
- Outside sport: climbing, skiing, sailing, and hiking. Competition in running and triathlon.

Publications

Presented at conferences:

During my thesis, I had several oral presentations. Three relevant ones are listed here:

1. "*3D EDX Microanalysis by FIB-SEM: Algorithm for elemental quantification enhancement*."
   EMAS, Anger/France, May 2011
2. "*3D EDX Microanalysis by FIB-SEM: Algorithm for elemental quantification enhancement*."
   M&M, Nashville TN/United-States, August 2011
3. "*Microanalyse en 3D par MEB-FIB: Limitations, Potentiel et Perspectives*."
   GN-MEBA, Journée pédagogique, Paris/France, December 2011

First author:

A first publication on a specific material studied by 3D EDS microanalysis is under review process. A second publication relating the dissertation focus will be written.

Coauthor:

1. M.A. Salgado-Ordorica, **P. Burdet**, M. Cantoni and M. Rappaz, "*Study of the twinned dendrite tip shape II: experimental assessment*" Acta Mater 59(13), 5085-5091 (2011)
2. F. Bernard, C. Rousselot, P. Delobelle, L. Hirsinger, and **P. Burdet**, "*Magnetic-field induced strains in ferromagnetic shape memory alloy Ni $_{55}Mn_{23}Ga_{22}Z$ deposited by RF-magnetron sputtering*", Plasma Process Polym 6 (SUPPL. 1) , 822-825 (2009)
3. N. Butoescu, O. Jordan**, P. Burdet**, P. Stadelmann, A. Petri-Fink, H. Hofmann, and E. Doelker, "*Dexamethasone-containing biodegradable superparamagnetic microparticles for intra-articular administration: Physicochemical and magnetic properties, in vitro and in vivo drug release*", Eur J Pharm Biopharm 72 (3), 529-538 (2009)